Atomic-Scale Simulation of keV Xenon Ion Irradiation-Induced Erosion in Spacecraft Electric Thruster Materials

Maximilian Maigler

Vollständiger Abdruck der von der Fakultät für Elektrische Energiesysteme und Informationstechnik der Universität der Bundeswehr München zur Erlangung des akademischen Grades eines

Doktors der Naturwissenschaften (Dr. rer. nat.)

angenommenen Dissertation.

Gutachter 1:	Univ.-Prof. Dr.-Ing. Jochen Schein
Gutachter 2:	Prof. Dr. Bärbel Rethfeld
Gutachter 3:	Prof. Dr. Siegfried Glenzer

Die Dissertation wurde am 28.10.2024 bei der Universität der Bundeswehr München eingereicht und durch die Fakultät für Elektrische Energiesysteme und Informationstechnik am 04.03.2025 angenommen. Die mündliche Prüfung fand am 06.05.2025 statt.

Acknowledgements

Zunächst gilt mein besonderer Dank Herrn Prof. Schein, der das Institut zu jeder Zeit mit Weitsicht, Herzlichkeit und einer Prise Humor leitet. Durch seine offene und vertrauensvolle Art schafft er ein Umfeld, in dem sowohl wissenschaftliche Neugier als auch Freude an der Forschung an erster Stelle stehen. Die Zeit an der UniBw war für mich geprägt von einer familiären Atmosphäre, die das tägliche Arbeiten zu etwas Besonderem gemacht hat. Meinen Kollegen danke ich herzlich für diese einmalige Erfahrung – es war mir eine große Ehre, Teil dieses Teams sein zu dürfen.

Besonders bereichernd waren auch die gemeinsamen sportlichen Aktivitäten mit den Kollegen vom LRT – ob beim Fußballtennis, Fußball oder im Fitnessstudio. Ebenso in Erinnerung bleiben mir die zahlreichen Gespräche bei unseren gemeinsamen Mittagessen in der Mensa, die den Arbeitsalltag stets mit Leichtigkeit erfüllten.

Während meiner Promotion hatte ich die Möglichkeit, wertvolle fachliche Erfahrungen zu sammeln und an vielfältigen Projekten mitzuwirken – Kenntnisse, die meine heutige berufliche Tätigkeit maßgeblich prägen und ohne die vieles nicht möglich wäre.

Mein tief empfundener Dank gilt meiner Familie, die mir stets mit Liebe, Vertrauen und Rückhalt zur Seite stand, sowie meinen engsten Freunden für ihre Unterstützung auf diesem Weg.

Nicht zuletzt durfte ich während dieser Zeit Dich, CM, kennenlernen. Du hast ein kleines Schiff auf dem Ozean entdeckt – und es wünscht sich nichts sehnlicher, als seine Reise ins Unbekannte an Deiner Seite fortzusetzen.

Kurzfassung

Diese Dissertation befasst sich mit der Entwicklung eines numerischen Modells zur Simulation der komplexen physikalischen Phänomene, die während der Xenon-Ionen-Bestrahlung von verschiedenen Materialien im niedrigen keV Bereich auftreten. Es wurden Titan, Graphit, Quarz und Siliziumkarbid untersucht, welche Materialien sind, die häufig in elektrischen Triebwerken von Satelliten verwendet werden. Das Modell koppelt die Molekulardynamik (MD) mit dem Zwei-Temperaturen-Modell (TTM) und ermöglicht so die zeitliche Auflösung atomarer und elektronischer Subsysteme auf ihren jeweiligen charakteristischen Längen- und Zeitskalen. Die zwei primären Ziele dieser Forschung können wie folgt zusammengefasst werden: Erstens erlaubt das Modell eine detaillierte Analyse der theoretisch vorhergesagten thermischen Spitzen und Kollisionskaskaden, die für lokales Schmelzen und die Ausstoßung von Atomen von der bestrahlten Oberfläche verantwortlich sind. Zweitens zielt die Studie darauf ab, die Lücke zwischen theoretischen Vorhersagen und praktischen Anwendungen zu schließen, indem Sputteringraten und Ionenimplantationstiefen vorhergesagt werden können, die für die Entwicklung und Optimierung von Triebwerkskomponenten, die einer Xenon-induzierten Erosion ausgesetzt sind, entscheidend sind. Diese Berechnungsergebnisse werden mit experimentellen Daten verglichen sowie gegen bestehende Softwaretools, insbesondere TRIM, abgeglichen. Die Ergebnisse liefern ein Verständnis der zugrunde liegenden physikalischen Phänomene und zeigen eine gute bis exzellente Übereinstimmung mit experimentellen Messungen, was die Fähigkeiten der numerischen Modellierung zur Bereitstellung hochwertiger und zuverlässiger Vorhersagen für die Erosion und Langlebigkeit elektrischer Triebwerke demonstriert.

Abstract

This thesis presents the development of a numerical model designed to simulate the complex physical phenomena taking place during xenon ion irradiation on materials commonly used in electric thrusters, namely titanium, graphite, quartz, and silicon carbide. The model couples the molecular dynamics (MD) technique with the two-temperature model (TTM), enabling the temporal resolution of atomic and electronic subsystems on their respective characteristic length and time scales. The primary objectives of this research are twofold. Firstly, the model allows for the detailed analysis of the theoretically predicted thermal spike and collision cascade phenomena, which are responsible for local melting and the ejection of atoms from the irradiated target surface. Secondly, the study aims to bridge the gap between theoretical predictions and practical applications by evaluating sputter yields and ion implantation depths, crucial for the development and optimization of thruster components subjected to xenon-induced erosion. The obtained computational results are compared with experimental data and benchmarked against existing software tools, namely TRIM. The findings provide a comprehensive understanding of the underlying physics and demonstrate good to excellent agreement with experimental measurements, advancing the capability of numerical modeling to deliver high-quality and reliable predictions for the erosion and lifetime of electric thrusters.

Contents

List of Symbols **iii**

List of Abbreviations **v**

List of Figures **vii**

1 Introduction **1**

1.1 Background and motivation 9

1.2 Problem statement 12

1.3 Literature review 13

2 Theory of ion beam sputtering **19**

2.1 Temporal evolution of the sputtering process 19

2.2 Two-temperature model 22

2.3 Nuclear and electronic stopping 22

2.4 Synopsis 25

3 Methodology **27**

3.1 Irradiation cases 27

3.2 Two-temperature molecular dynamics 30

3.3 Interatomic potentials 35

3.4 Computational details 38

3.4.1 Simulation framework 39

3.4.2 Numerical details 39

3.4.3 Deriving macroscopic and structural properties 46

3.4.4 Obtaining initial atomic configurations 47

3.4.5 Impact simulations 50

3.5 Synopsis 54

4 Results and discussion **57**
4.1 Titanium 58
4.1.1 Principal analysis 58
4.1.2 Parameter study 70
4.2 Graphite 74
4.2.1 Principal analysis 74
4.2.2 Parameter study 78
4.3 Quartz 83
4.3.1 Principal analysis 83
4.3.2 Parameter study 86
4.4 Silicon carbide 90
4.4.1 Principal analysis 90
4.4.2 Parameter study 93
4.5 Synopsis 97

5 Conclusion **99**

A Appendix **105**
A.1 LAMMPS input files 105
A.2 Data availability statement 112

List of Symbols

Symbol	Description	Unit
$\mathbf{a}$	acceleration	$\mathrm{m\,s^{-2}}$
Z	atomic number	1
σ	collision cross-section	$\mathrm{m^{-2}}$
$\mathbf{x}$	coordinate	m
ρ	density	$\mathrm{kg\,m^{-3}}$
g_p	e-ph coupling parameter	$\mathrm{W\,m^{-3}\,K^{-1}}$
E	energy	J
$\mathbf{F}$	force	N
γ_s	friction coefficient	$\mathrm{m\,s^{-1}}$
a_0	lattice constant	Å
m	mass	kg
$\dot{m}$	mass-flow	$\mathrm{kg\,s^{-1}}$
λ	mean-free path	m
M	molar mass	$\mathrm{kg\,mol^{-1}}$
n	number density	$1/\mathrm{m^3}$
g	pair correlaction function	1
p	pressure	$\mathrm{N\,m^{-2}}$
ξ	proportionality constant	1
r	radius or distance	m
C	specific heat	$\mathrm{J\,m^{-3}\,K^{-1}}$
T	temperature	K
κ	thermal conductivity	$\mathrm{W\,m^{-1}\,K^{-1}}$
D	thermal diffusivity	$\mathrm{m^2\,s^{-1}}$
t	time	s
τ	timescale	s
$\mathbf{u}$	velocity	$\mathrm{m\,s^{-1}}$
V	volume	$\mathrm{m^3}$

List of Abbreviations

Abbr.	Description
AEV	Adaptive electron voxels
AI	Artificial intelligence
AIREBO	Adaptive intermolecular reactive bond order
CEX	Charge exchange
CFL	Courant-Friedrichs-Lewy number
CP	Chemical propulsion
DC	Discharge chamber
DFT	Density-functional theory
DOS	Density of states
DSG	Deep-space gateway
DSMC	Direct-simulation Monte-Carlo
EAM	Embedded atom method
EP	Electric propulsion
FDM	Finite difference method
HET	Hall-effect thruster
ICP	Inductively coupled plasma
LAMMPS	Large-scale atomic/molecular massively parallel simulator
LCBOP	Intrinsic long-range bond-order potential
LJ	Lennard-Jones
LOX	Liquid oxygen
MC	Monte-Carlo method
MCC	Monte-Carlo collision
MD	Molecular dynamics
MEAM	Modified embedded atom method
MEX	Momentum exchange
MPD	Magnetoplasmadynamic thruster
PIC	Particle-in-Cell
PKA	Primary knock-on atom
PPT	Pulsed plasma thruster
PTM	Polyhedral template matching

REBO	Reactive empirical bond order
RF	Radio-frequency
RIT	Radio-frequency ion thruster
SCC	Space charge compensation
SCCM	Standard cubic centimetre per minute
SEM	Scanning electron microscopy
SHI	Swift heavy ion
SLURM	Simple Linux utility for resource management
SRIM	The stopping and range of ions in solids
TBBOP	Tight binding bond-order potential
TDE	Threshold displacement energy
TRIM	Transport of ions in matter
TSM	Thermal spike model
TTM	Two-temperature model
XRD	X-ray diffraction

List of Figures

1.1 Schematic of an electrostatic propulsion device. 4

1.2 Electron impact cross sections of different noble gases commonly used in EP according to Bartlett and Stelbovics [8]. 5

1.3 Schematic of a simplified RIT with axial propellant injection and 2-grid extraction configuration. 6

1.4 Different types of CEX cross sections for xenon from Miller *et al.* [9]. 7

1.5 Schematic of ions focused and accelerated by screen and accel grid, respectively; electrons are extracted from the discharge chamber plasma by the positively charged screen grid; CEX ions produced inside the accel grid by collisions with neutral propellant xenon atoms leaking out of the discharge chamber, leading to barrel erosion. . . . 8

1.6 RIT PIC–DSMC simulation of one grid hole illustrating superparticles. Screen, accel, and decel grid colored in red, green, and blue, respectively. From Maigler, Maaß, *et al.* [10]. 9

1.7 Percentage of CEX ions of results presented in Fig. 1.6. From Maigler, Maaß, *et al.* [10]. 10

1.8 NSTAR thruster screen and accel grid erosion after 8200 h operating time. From: Polk *et al.* [11]. 10

1.9 NSTAR thruster accel grid *pit* and *groove* erosion after 30 000 h operating time. From: Wirz, Anderson, Goebel, *et al.* [12]. 11

1.10 Various HET erosion exposures after endurance testing. From: Brown and Walker [14]. 11

2.1 Schematic of knock-on collision cascade by low keV ion irradiation dominated by nuclear stopping. The affected lattice volume is indicated by the grey area. The primary ion trajectory is denoted by the solid black line; secondary, tertiary, etc. displacements are denoted by the dashed lines. Since the kinetic energy of the impacting ion is much higher than the displacement energy threshold, permanent defects are induced. Energetic, non-primary collisions close to the surface of the lattice leads to sputtering of atoms, and, depending on the target material, SEE. Schematic based on Fig. 2 from Volkert and Minor [69]. 20
2.2 Stopping force of Au^+ ions iraddiated onto SiO_2 substrates [73]. . . . 23
2.3 **Left:** Electronic stopping force of Al substrate irradiated by H^+ ions. **Right:** Mean excitation energy measurements (see [77]). 25

3.1 Surface properties of RIT accel grid from PIC-DSMC simulation. The length of the vectors indicates the ion impact energy, the surface coloring the ion impact flux, and from the vector itself the ion impact angle can be derived. Results are scaled by $E_k^{\max} = 1.5\,\mathrm{keV}$, $\beta_{\mathrm{imp}}^{\max} = 75\,\mathrm{deg}$, and $J^{\max} = 1.5 \times 10^{19}\,\mathrm{m^{-2}\,s^{-1}}$. From: Maigler, Maaß, *et al.* [10]. 28
3.2 Schematic of impact parameters based on quantities outlined in Table 3.1. Due to randomized shifts of the ion's x and y positions at $t = 0$, the initial impact lattice impact position x_l changes each run. 30
3.3 Schematic of electron background cells containing a slab of copper atoms. From: Maigler, Held, *et al.* [87] 32
3.4 Schematic of AEV with different voxel states, based on the contained number of atoms. From: Maigler, Held, *et al.* [87] 33
3.5 Schematic of different ensembles to avoid pressure reflections and atoms crossing periodic boundaries. Ensemble (1) is evolved using the `nve` thermostat, ensemble (2) held at 1 bar pressure and 300 K temperature employing the `npt` thermostat, and ensemble (3) are non-moving *ghost* atoms only allowed to interact with atoms of ensemble (2) through the potential. 40
3.6 Comparison of pair correlation function by Wang, Yang, *et al.* [124] and numerical verification study of Ti at 2400 K. 42
3.7 Electronic specific heat of graphite and diamond predicted by DFT simulations from Xibraku *et al.* [128]. They provided their values in meV/K/atom, which were converted to SI units using an atomic volume of $V^{\mathrm{Carbon}} = 4/3\pi\,(150\,\text{Å})^3 = 1.41 \times 10^{-29}\,\mathrm{m^3}$. 44

3.8 Temperature dependent electronic properties of Ti based on DOS simulation from Lin *et al.* [89]. **Left**: Specific heat capacity **Right**: Electron-phonon coupling parameter. 44
3.9 Temperature dependent heat capacity of SiO_2 in LAMMPS units; scatter plot represents data from [53], continuous line is the fit according to Eq. (3.23). 45
3.10 Template matching hulls for different lattice structures. From: Larsen *et al.* [136]. 47
3.11 Example of polycrystalline initialization using Voronoi tessellation [138] in the `atomsk` code. 48
3.12 SiC supercell during quenching period and equilibriation, colored by PTM identified lattice structures (`dcub` and `dhex`) using a continuous volume rendering technique. The left image shows the initial growth of diamond like crystal nuclei from the slowly cooled liquid. The right image illustrates the formation of groups from crystalline nuclei at a later stage during quenching. 49
3.13 SiC supercell after equilibriation, melting, and quenching; portrayed as atomic bonds, colored by atom type (**blue**: Si, **red**: C). A surface-mesh of the supercell was generated to outline the formation of non-uniform topology during quenching. Crystalline boundary: 19 %, diamond cubic `dcub` atoms: 60 %, diamond hexagonal `dhex` atoms: 21 %. 50
3.14 SiO_2 supercell after equilibriation, melting, and quenching. Left: generated surface mesh of final configuration before irradiation with Xe^+ ion at $t = 0$. Right: portrayal of atomic bonds, colored by atom type (**blue**: Si, **red**: O), showcasing amorphous topology and bulk structure. 51
3.15 Ti supercell after melting, quenching, and equilibriation, colored by PTM identified lattice structures. [1]Crystalline boundary atoms: 10 %, face-centred-cubic `fcc` atoms: 1 %, hexagonal close packed `hcp` atoms: 85 %, body centred cubic `bcc` atoms: 4 %. 52
3.16 Graphite supercell after equilibriation, illustrating stacked layers of graphene and array of hexagonal carbon rings building graphite. . . 53

4.1 **Case:** $E_{Xe+} = 1.4\,\mathrm{keV}$, $\beta = 0\,\mathrm{deg}$. Top: Time-dependent ion velocity of the five different runs with mean indicated by dashed black line. Bottom: Time-dependent total penetration depth $|z|$. The time when the ion comes to rest in all cases is indicated by the vertical gray line. 59

4.2 **Case:** $E_{\mathrm{Xe+}} = 1.4\,\mathrm{keV}$, $\beta = 0\,\mathrm{deg}$, run 3. Region affected by ion irradiation after 2 ps. The collision cascade produces fast atoms escaping their lattice structure (indicated in blue as *None*), generating a region of liquid titanium, which relaxes after the ion and cascade have come to rest. In this simulation, 1 titanium atom left the bulk material and crossed the upper boundary condition ($Y = 1$) while the region marked in yellow featured a temperature of roughly 1200 K, slowly relaxing towards the initial temperature. Ion velocity colored from red: ≡ 50 km/s to blue: ≡ 0 km/s. 60

4.3 **Case:** $E_{\mathrm{Xe+}} = 1.4\,\mathrm{keV}$, $\beta = 0\,\mathrm{deg}$. Temporal evolution of mean and max atomic and electronic temperature. The thick dashed lines respresent the averages of the five runs for each quantity; the melting temperature of Ti is indicated by the horizontal, gray dashed line; the time when the ion comes to rest according to Fig. 4.1 is given by the vertical gray line. 61

4.4 **Case:** $E_{\mathrm{Xe+}} = 1.4\,\mathrm{keV}$, $\beta = 0\,\mathrm{deg}$. Temporal evolution of voxels with (atomic) temperatures above T_{melt} and number of atoms leaving the hcp or bcc structure compared to the initial number at $t = 0$ (see Fig. 3.15). 62

4.5 **Case:** $E_{\mathrm{Xe+}} = 1.4\,\mathrm{keV}$, $\beta = 0\,\mathrm{deg}$, run 1. Snapshots of collision cascade the first 360 fs after the ion is launched onto the Ti target. . 63

4.6 **Case:** $E_{\mathrm{Xe+}} = 1.4\,\mathrm{keV}$, $\beta = 70\,\mathrm{deg}$, run 3. Comparative illustration to Fig. 4.2; impact zone with blue atoms indicating atoms in liquid state. 65

4.7 **Case:** $E_{\mathrm{Xe+}} = 1.4\,\mathrm{keV}$, $\beta = 70\,\mathrm{deg}$. Comparative illustration to Fig. 4.1. The mean penetration depth decreases by a factor of 0.3 to 12 Å; the mean duration for the ion to come to rest increases from 0.6 to 0.7 ps. 66

4.8 **Case:** $E_{\mathrm{Xe+}} = 1.4\,\mathrm{keV}$, $\beta = 70\,\mathrm{deg}$. Comparative illustration to Fig. 4.3. The thermal spike is much more pronounced accompanied by a higher maximum electron temperature of 8000 K compared to normal incidence. 67

4.9 **Case:** $E_{\mathrm{Xe+}} = 1.4\,\mathrm{keV}$, $\beta = 70\,\mathrm{deg}$. Comparative illustration to Fig. 4.4. Thermal spike indicated by red zone from 0 – 0.5 ps after impact, maximum number of voxels above T_{melt} at 0.2 ps. 68

4.10 **Case:** $E_{\mathrm{Xe+}} = 1.4\,\mathrm{keV}$, $\beta = 70\,\mathrm{deg}$, run 5. Comparative illustration to Fig. 4.5. Atomic trajectories of collision cascase the first 360 fs with 4 sputtered atoms. Logarithmic velocity contours from $1 - 50\,\mathrm{km\,s^{-1}}$ (blue to red). 69

4.11 **Case:** $E_{\mathrm{Xe+}} = 1.4\,\mathrm{keV}$, $\beta = 70\,\mathrm{deg}$, run 3. Volume rendering of atomic voxel temperature the first 2.5 ps after ion is launched. Colormap scaled to $\min(T) = 350\,\mathrm{K}$ and $\max(T) = T_{\mathrm{melt}} = 1941\,\mathrm{K}$. 71
4.12 Ti parameter study of yield and penetration depth including comparison with experimental data from Tartz, Heyn, Bundesmann, Zimmermann, *et al.* [60] and Ziegler *et al.* [68] (denoted as TRIM–2013). 72
4.13 **Case:** $E_{\mathrm{Xe+}} = 1.4\,\mathrm{keV}$, $\beta \in \{0, 70\}\,\mathrm{deg}$. Top row: Time-dependent ion velocity of the five different runs with mean values indicated by dashed black line. Bottom row: Time-dependent total penetration depth $|z|$. The time when the ion reaches the *inter–layer bouncing* phase is indicated by the vertical gray line. 75
4.14 **Case:** $E_{\mathrm{Xe+}} = 1.4\,\mathrm{keV}$, $\beta = 0\,\mathrm{deg}$. Temporal evolution of mean and max atomic and electronic voxel temperatures 76
4.15 **Case:** $E_{\mathrm{Xe+}} = 1.4\,\mathrm{keV}$, $\beta = 0\,\mathrm{deg}$. Temporal evolution of voxels above sublimation temperature and atoms forced out of their graphite lattice structure. 77
4.16 **Case:** $E_{\mathrm{Xe+}} = 1.4\,\mathrm{keV}$, $\beta = 70\,\mathrm{deg}$. Temporal evolution of voxels above sublimation temperature and atoms forced out of their graphite lattice structure at high angle of incidence. About 3× as many voxels are forced above T_{melt} but the same number of atoms forced out of their PTM structure. 77
4.17 **Case:** $E_{\mathrm{Xe+}} = 1.4\,\mathrm{keV}$, $\beta = 70\,\mathrm{deg}$. Closeups of the impact region the first 5 ps. Left: atomic velocity (blue to red: 1 to $100\,\mathrm{km\,s^{-1}}$), right: atoms colored by PTM identification. 79
4.18 Measurements of energy dependent mean impact angle of xenon ions on the μ−10 EM RIT engine accel grid (top) and SEM images of the accel grid downstream edge (bottom left, right). From: Nakano *et al.* [61]. 80
4.19 C parameter study of yield and penetration depth including comparison with experimental data from Nakano *et al.* [61] and Ziegler *et al.* [68] (denoted as TRIM–2013). 81
4.20 Comparison of penetration ranges in graphite subjected to bombardment by fast neutrons (Christie *et al.* [52]) and fast xenon ions (present study, TTM–MD) in the keV regime. 83
4.21 **Case:** $E_{\mathrm{Xe+}} = 1.4\,\mathrm{keV}$, $\beta \in \{0, 70\}\,\mathrm{deg}$. Top row: Time-dependent ion velocity of the four different runs with mean indicated by dashed black line. Bottom row: Time-dependent total penetration depth $|z|$. 84

4.22 **Case:** $E_{\mathrm{Xe+}} = 1.4\,\mathrm{keV}$. Comparison of temporal evolution of mean and maximum atomic and electronic voxel temperatures. 85
4.23 **Case:** $E_{\mathrm{Xe+}} = 1.4\,\mathrm{keV}$, $\beta = 70\,\mathrm{deg}$, run 2. Snapshots of temporal evolution of atomic velocity and ion trajectory length. 87
4.24 SiO_2 parameter study of yield and penetration depth including comparison with experimental data from Tartz, Heyn, Bundesmann, and Neumann [62], Nenadović *et al.* [63], Yalin *et al.* [64], and Ziegler *et al.* [68] (denoted as TRIM–2013). 88
4.25 **Case:** $E_{\mathrm{Xe+}} = 1.4\,\mathrm{keV}$, $\beta \in \{0, 70\}\,\mathrm{deg}$. Top row: Time-dependent ion velocity of the four different runs with mean indicated by dashed black line. Bottom row: Time-dependent total penetration depth $|z|$. 91
4.26 **Case:** $E_{\mathrm{Xe+}} = 1.4\,\mathrm{keV}$. Top row: comparison of mean and maximum atomic and electronic voxel temperatures. Bottom row: comparison of number of atoms converted to atoms without PTM structure and atomic voxels with temperatures higher than T_{melt} 92
4.27 **Case:** $E_{\mathrm{Xe+}} = 1.4\,\mathrm{keV}$, $\beta = 0\,\mathrm{deg}$, run 2. **Left**: snapshots of temporal evolution collision cascade with ion velocity and atomic PTM structure, filtered by trajectory length. Target top surface indicated by transparent grey area / white line. Coloring of target atoms by PTM identified structure (PTM=0, dcub, and PTM=dhex). **Right**: Time-dependent number of atoms forced out of dcub or dhex structure. 94
4.28 SiC parameter study of yield and penetration depth including comparison with experimental data from Ecke *et al.* [65] and Ziegler *et al.* [68] (denoted as TRIM–2013). 95

Starting from day 0 became my friend.

— D. Goggins

1 Introduction

Contents

1.1 Background and motivation 9
1.2 Problem statement 12
1.3 Literature review 13

With the explosive growth of SpaceX's global Starlink fleet, electric satellite propulsion (EP) has become the most widely used propulsion technique for attitude control of satellites operating in orbit as well as for orbit raising and specific orbit insertion maneuvers [1]. One of the most important quantities in astrodynamics governing orbital maneuvers is the total change of velocity Δu, sometimes referred to as *Delta–v*, given by the expression

$$\Delta u = u_e \ln\left(\frac{m_0}{m_d}\right) \qquad u_e = I_{\text{sp}} \cdot g_0 \,. \tag{1.1}$$

In Eq. 1.1, u_e is the exhaust velocity, m_0 the vehicle's initial mass before the orbital maneuver, m_d the vehicle's dry mass after the maneuver, I_{sp} the engine's specific impulse, and g_0 the standard gravity, respectively. Every orbital maneuver can be characterized by the required amount of Δu. Eq. 1.1 was initially derived by Tsiolkovsky [2] in 1903 and has fundamentally shaped the research, design, and engineering of rockets ever since. The "tyranny" of Eq. 1.1, as some like to describe it, lies in the fact that the more Δu one likes to achieve, the more propellant is required. Because of this circumstance, most of a rocket's initial mass is propellant and not the actual payload. This has lead to the concept of staging, where burnt out, empty

stages are seperated after they have consumed their fuel. A different way to approach this dilemma is to maximize the exhaust velocity of the engine and therefore it's I_{sp}. However, conventional chemical engines used for launching payloads into space are severely limited by their ability to attain large exit velocities of their propellant. The maximum exit velocity of $4400\,\mathrm{m\,s^{-1}}$ is achieved by burning liquid hydrogen (LH2) with liquid oxygen (LOX), corresponding to a specific impulse of 450 s.

This lead to the development of electrical engines, which accelerate ions in order to produce thrust. The kinetic energy and therefore exhaust velocity of the ions is proportional to the accelerating potential described by the relation

$$E_k = mu^2 = e\phi\,, \tag{1.2}$$

where m, e and ϕ denote the ion's mass, the elementary charge of $1.6 \times 10^{-19}\,\mathrm{C}$ and the electrostatic potential, respectively. Applying acceleration potentials of just few hundreds of volts already allows exhaust velocities many times that of the most efficient chemical engines. Thus, electric engines exhibit several advantages over classical in-orbit propulsion methods such as chemically propelled (CP) thrusters, including:

- Higher specific impulse, $I_{\mathrm{sp}}^{\mathrm{EP}} = (5-20)\cdot I_{\mathrm{sp}}^{\mathrm{CP}}$
- Power for operating the thruster can be accessed from solar arrays
- Lower total mass of propellant required due to higher I_{sp} for the same Δu
- Propellant is usually an inert gas, thus no chemically reacting and hypergol propellants are required
- Allowing for extremely precise thrust in the µN regime

However, the essential shortcoming compared to CP is the much lower total thrust

$$T = \dot{m}u_e \tag{1.3}$$

produced by EP. In Eq. (1.3), $\dot{m}$ and u_e denote the propellant mass flow and exit velocity, respectively. While u_e of EP devices is much higher, which is the reason for their high specific impulse, the total mass flow is considerably lower and usually measured in standard cubic centimetre per minute (SCCM) compared to kg/s of CP thrusters. Consequently, operating times of EP thrusters are required to be much longer for achieving the same *delta-v*[1]. Nonetheless, both the academic and industrial sectors work closely together and invest considerable effort to overcome

[1]A measure of how much impulse per mass unit of a spacecraft is required to achieve a desired orbital maneuver.

this disadvantage. As a result, the most powerful EP thrusters *in production* may achieve thrusts up to $\approx 2\,\mathrm{N}$ (AEPS, [3]). In fact, the primary in-orbit propulsion technique utilized for NASA's Deep Space Gateway (DSG, launch of first sections no-earlier than 2025) are Hall effect thrusters (HETs), which can generate up to $0.6\,\mathrm{N}$ of thrust at $13\,\mathrm{kW}$ operating power [4].

Since first attempts of using electrothermal thrusters in the early 1960s [5], a wide range of EP systems has been developed. After initial attempts to test ion engines in space proved to be difficult [6], first successes in using the new technology for attitude control were reported by Cybulski *et al.* [7]. Since then, three main branches of EP thrusters have been established:

1. **Electrostatic engines**:
    - Gridded (radio-frequency) ion thruster (RIT)
    - Hall-effect thruster[2] (HET)
2. **Electromagnetic engines**:
    - (Pulsed) plasma thruster (PPT)
    - Magnetoplasmadynamic thruster (MPD)
3. **Electrothermal engines**:
    - Arcjet thruster
    - Resistojet thruster
    - Microwave thruster

A schematic of the working principle of an electrostatic thruster is illustrated in Figure 1.1. The propellant, usually xenon, is fed from a high-pressure reservoir through a valve to the ionization chamber. The neutral gas is then ionized in the chamber, for instance by a radio-frequency generating coil wrapped around it. Ions are extracted from the chamber by means of an extraction and acceleration mechanism such as an electrostatically charged grid. To avoid satellite charge-up and excessive beam divergence, the space charge is compensated (SCC) by injecting electrons into the exhaust plume. The velocity at which the ions exit the extraction system is in the range of tens of thousands of m/s. Despite the high exit velocity, EP allows for precise attitude adjustment maneuvers by reducing the already low mass

[2] Due to the presence of strong permanent magnets in HETs, they are sometimes categorized as *electromagnetic* engines.

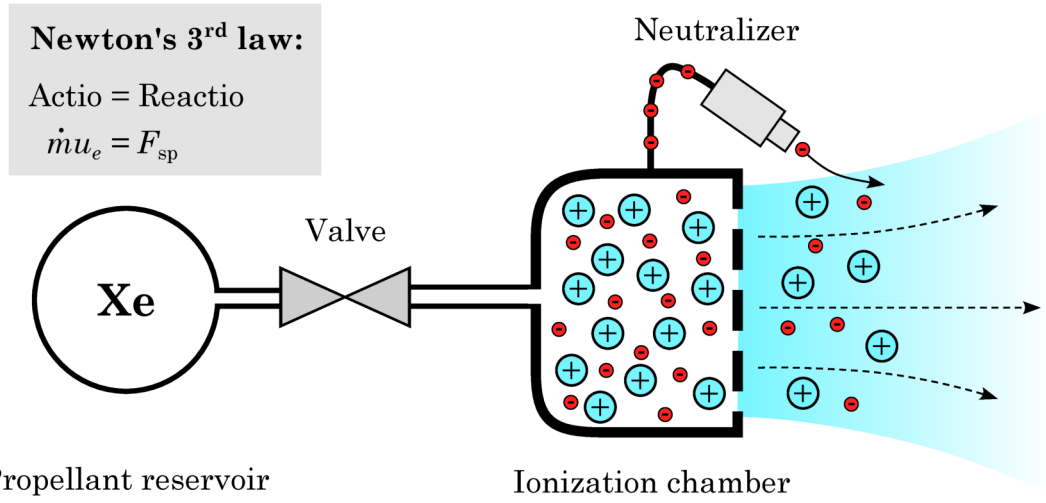


Figure 1.1 Schematic of an electrostatic propulsion device.

flow. To give an example, consider a thruster with $u_e = 40\,000\,\mathrm{m/s}$ and a desired thrust of $50\,\mu\mathrm{N}$. In this case, the required mass flow would be

$$\dot{m} = \frac{T}{u_e} = \frac{50\,\mu\mathrm{N}}{40\,000\,\mathrm{m/s}} = 1.25 \times 10^{-9}\,\mathrm{kg/s}\,. \tag{1.4}$$

One can convert this value using the expression

$$\dot{m}_{\mathrm{SCCM}} = \frac{\dot{m}_{\mathrm{SI}}}{7.44 \times 10^{-10} \cdot M} = 0.013\,\mathrm{SCCM}\,, \tag{1.5}$$

considering xenon with a molar mass of $M_{\mathrm{Xe}} = 131\,\mathrm{u}$. The high exit velocity of the ions is achieved by employing a strong electromagnetic field with a specific orientation and field strength, which produces a directed force, i.e., the Lorentz force, on charged particles. According to Newton's third law (actio = reactio), this gives rise to a force propelling the spacecraft in the opposite direction.

In order to ionize the propellant in electrostatic thrusters, neutral atoms are bombarded with fast electrons inside the discharge chamber or channel. During the collision process, one or more electrons are ejected from the valence band, resulting in the production of a new freely moving electrons and a singly or multiply charged ion. It is desirable to use propellants that exhibit low binding energy of valence electrons to the nucleus as well as high atomic mass to maximize the impulse of individual ions produced during extraction.

The forces of an electromagnetic field exerted on a singly charged ion or electron can be written as

$$\mathbf{F}_{em} = e\mathbf{E} + e(\mathbf{u} \times \mathbf{B})\,, \tag{1.6}$$

where e denotes the elementary charge (1.602×10^{-19} C), $\mathbf{E}$ the electric field, $\mathbf{u}$ the particle's velocity vector, and $\mathbf{B}$ the magnetic field. The temporal evolution of a charged particle's trajectory is governed by Newton's second law of motion, expressed as

$$\mathbf{F} = m \cdot \frac{\partial \mathbf{u}}{\partial t} \qquad \leftrightarrow \qquad \mathbf{u} = \int_{t_0}^{t_1} \frac{\mathbf{F}_{em}}{m} \partial t \,. \tag{1.7}$$

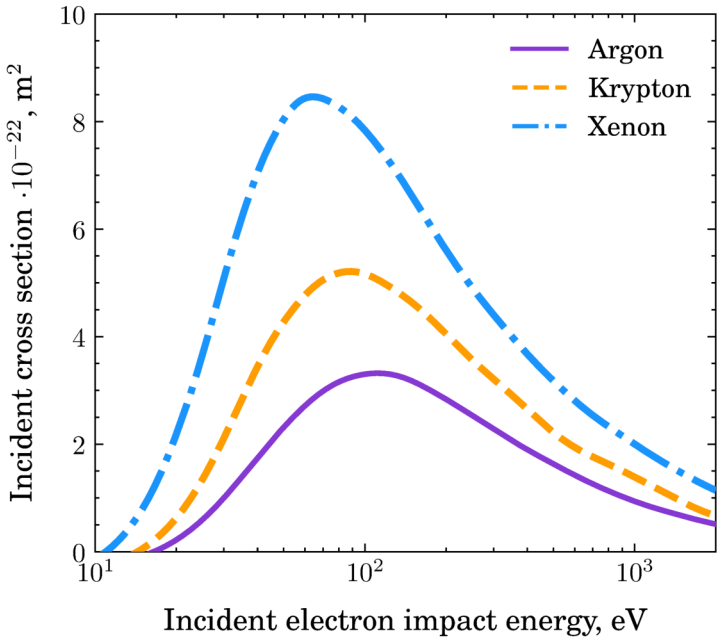


Figure 1.2 Electron impact cross sections of different noble gases commonly used in EP according to Bartlett and Stelbovics [8].

Following Eq. (1.7), ions with a higher mass are preferred because the resulting force is proportional to the mass. Xenon is commonly used as the propellant, since it exhibits the highest impact cross section[3] compared to other noble gases, such as argon or krypton across a wide range of incident electron impact energies, as illustrated in Figure 1.2.

A popular method for generating high-energy electrons is utilized in inductively coupled plasmas (ICP), where a radio-frequency alternating electromagnetic field is applied within a discharge chamber. ICPs are widely used in RITs due to their large degree of ionization $\xi = \chi_p / \chi_n$ and proportionality to the power input of the coil. Figure 1.3 illustrates an example of such a thruster with axial injection and a 2-grid extraction system. Inside the discharge chamber, the alternating RF field produces a force acting on the electrons, which rapidly oscillate along the varying field lines to eventually collide with propellant atoms. Due to the extremely low pressure outside

[3] A measure of the likelyhood of an ionization-resulting collision taking place according to the specific impact energy, based on the reaction $\mathrm{Xe} + \mathrm{e}^- \longrightarrow \mathrm{Xe}^+ + 2\,\mathrm{e}^-$.

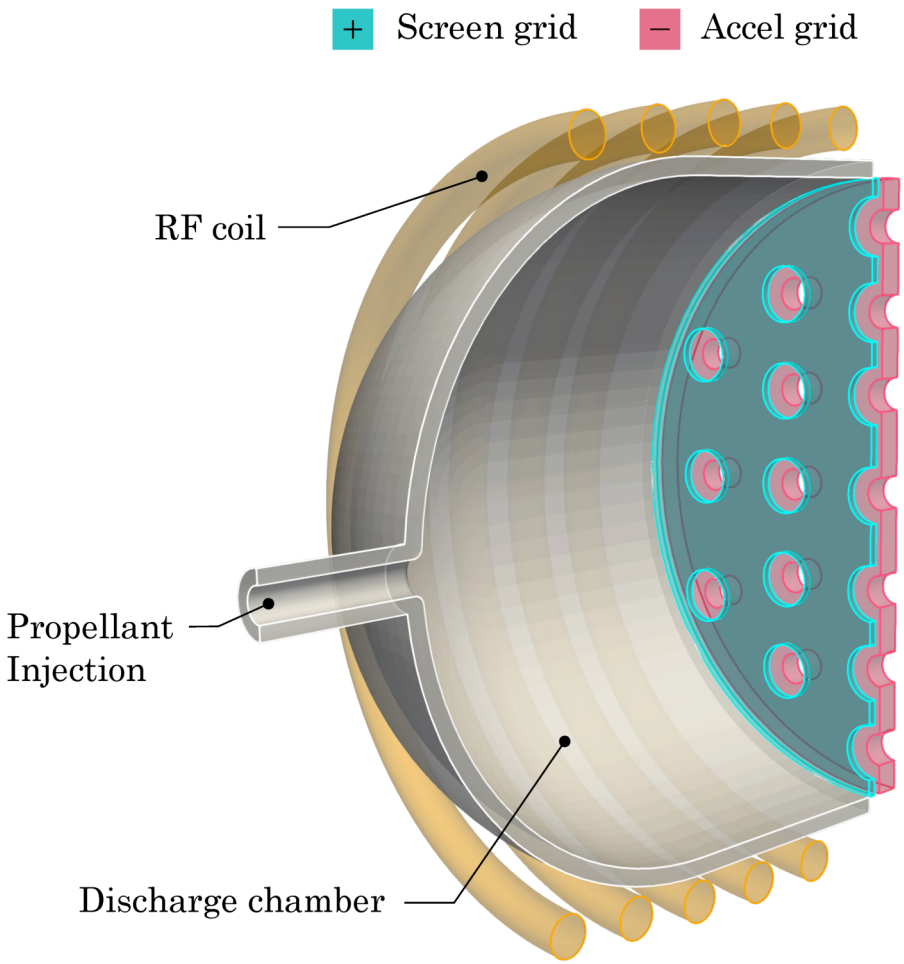


Figure 1.3 Schematic of a simplified RIT with axial propellant injection and 2-grid extraction configuration.

of the thruster behind the extraction grid, a portion of neutral propellant leaks out and leaves the discharge chamber unionized. Therefore, the thruster's effiency is based on it's ability to ionize and extract the propellant ions before it leaks out.

A 2-grid RIT example thruster is shown in Figure 1.3 and the grid apparatus consists of a screen grid, which is positively charged with respect to the satellite potential in order to focus the ions. The subsequent accel grid is negatively charged and accelerates the ions and repels the electrons. In the extraction region, the composition is made up of two main components:

1. Neutral gas leaking out from the discharge chamber.
2. Ions focused within the screen grid and accelerated within the accel grid.

The number density of neutral atoms and ions is still high enough for frequent collisions to take place. Mainly, so-called charge exchange (CEX) events occur

when a fast moving ion collidies with a slow moving neutral atom, resulting in the exchange of its charge and momentum:

$$\text{CEX}: \quad \text{Xe}^{+}_{\text{fast}} + \text{Xe}_{\text{slow}} \longrightarrow \text{Xe}^{+}_{\text{slow}} + \text{Xe}_{\text{fast}} \tag{1.8}$$

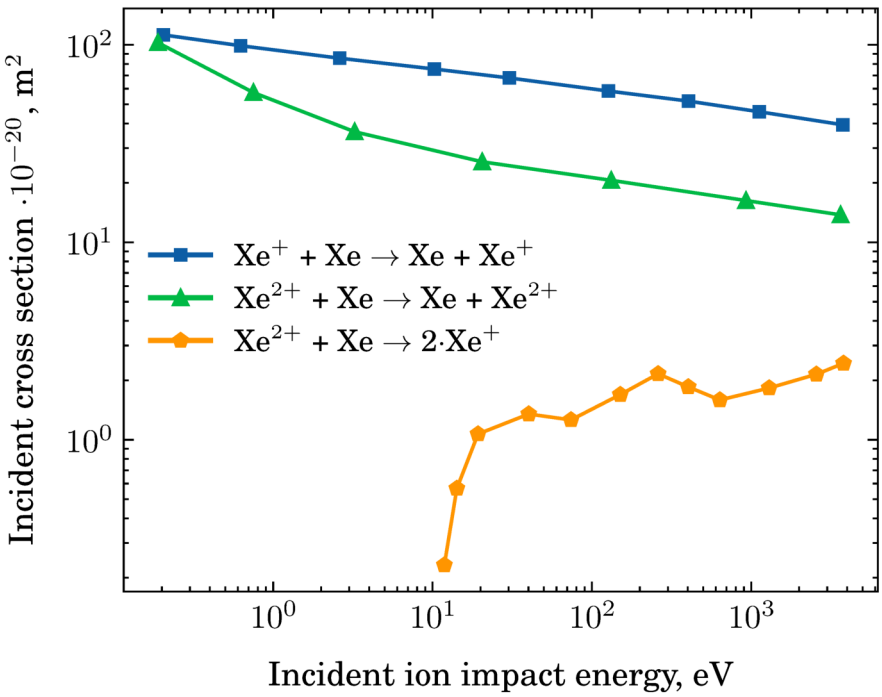


Figure 1.4 Different types of CEX cross sections for xenon from Miller *et al.* [9].

If this event takes place within the vicinity of the accel grid, the slow moving ion with a now random trajectory is subsequently accelerated towards it and impacts the surface. Collision cross sections of different reactions producing CEX ions are given in Figure 1.4. Since the mass of single ions is low, they are quickly accelerated towards the accel grid and their impact velocity can reach the same velocity as perfectly extracted ions. Slow ions can also be produced by collisions with other ions (momentum exchange, MEX) in proximity of the screen grid, yielding misaligned acceleration and collision with the accel grid. Although in HETs a different approach is utilized to extract and accelerate ions, the essential problem remains the same: MEX and CEX ions producing erosion on extraction and acceleration surfaces due to ion bombardment.

To illustrate the problematic of CEX ions in RIT grids, Figure 1.5 delineates the extraction of ions and electrons from the discharge chamber (denoted as DC) plasma. The screen grid removes electrons from the plasma and concentrically

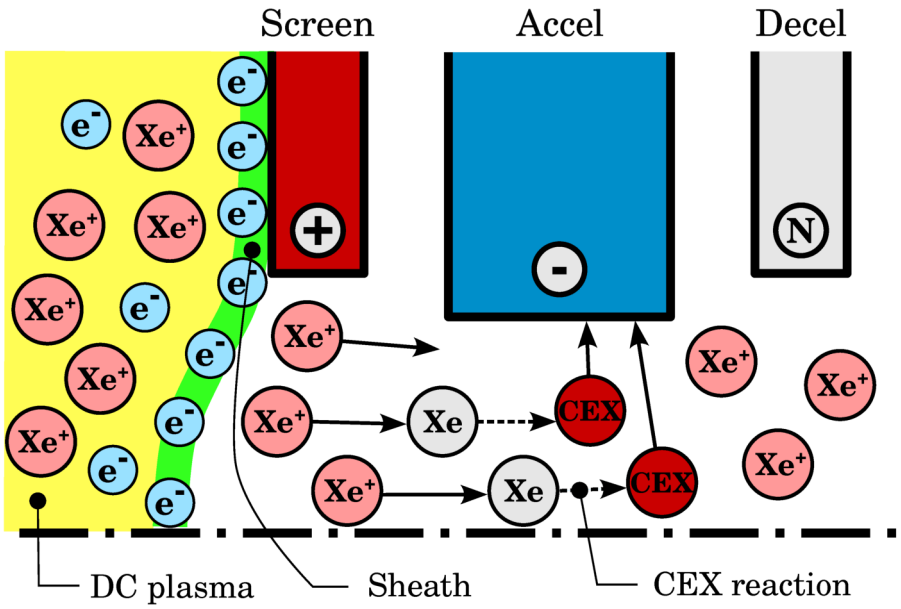


Figure 1.5 Schematic of ions focused and accelerated by screen and accel grid, respectively; electrons are extracted from the discharge chamber plasma by the positively charged screen grid; CEX ions produced inside the accel grid by collisions with neutral propellant xenon atoms leaking out of the discharge chamber, leading to barrel erosion.

focuses ions which arrive with Bohm velocity[4] due to pre-sheath effects in order to ensure conservation of electronic and ionic wall fluxes. The ensuing accel grid accelerates the ions to their exhaust velocity. Behind the grounded decel grid, the ions space charge compensate with electrons ejected from the neutralizer.

Figure 1.6 portrays how this entire extraction process is modeled using fully-kinetic Particle-in-Cell Direct-Simulation Monte Carlo (PIC–DSMC) simulations [10]. It additionally illustrates how CEX ions are mostly produced within the accel grid region.

A section cut of the fraction of CEX ions to primary ions in the grid region is shown in Figure 1.7. It is observed that up to 2 % of ions in the extraction grid are CEX ions and for the initially non-eroded accel grid, barrel errosion in the rear section of the inner accel grid radius is the main erosion type. This is highlighted by the yellow dashed lines where the flux of CEX ions onto the surface of the walls is the largest.

[4]The Bohm velocity mainly depends on the electron temperature and is typically around few $\mathrm{km\,s^{-1}}$.

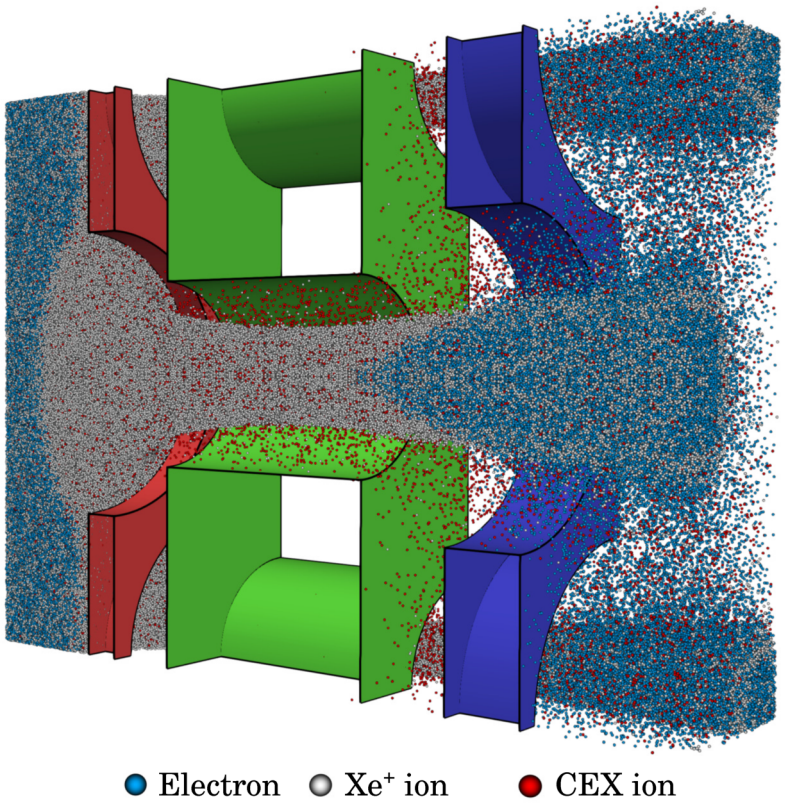


Figure 1.6 RIT PIC–DSMC simulation of one grid hole illustrating superparticles. Screen, accel, and decel grid colored in red, green, and blue, respectively. From Maigler, Maaß, *et al.* [10].

1.1 Background and motivation

The lifetime of most EP devices is limited by erosion leading to disfunction of the accelerating mechanism. In RITs, the primary failure mode at higher power levels is electron backstreaming from the neutralized plasma plume acting as the electron source. Due to erosion and thus enlargement of the accel grid, (thermal) downstream electrons are able to be attracted from the screen grid and disturb the ion extraction process [11]. The application of a third *decel* grid improves the electron backstreaming problem, until downstream CEX ions have dramatically induced pit and groove erosion.

Figure 1.8 illustrates experimental exposures using scanning electron microscopy (SEM) of a RIT after more than 8000 h of operating time. After this period of operation, the so-called *barrel* or *aperture wall* erosion is the most prominent one. It is manifesting itself by eroding the inner accel grid surface, leading to a non-uniform widening of the radius along the downstream direction. Longer operating times can cause erosion in the form of *pits* and *grooves*, primarily caused by CEX ions behind the acceleration grid with perpendicular impacts. Comparative figures of

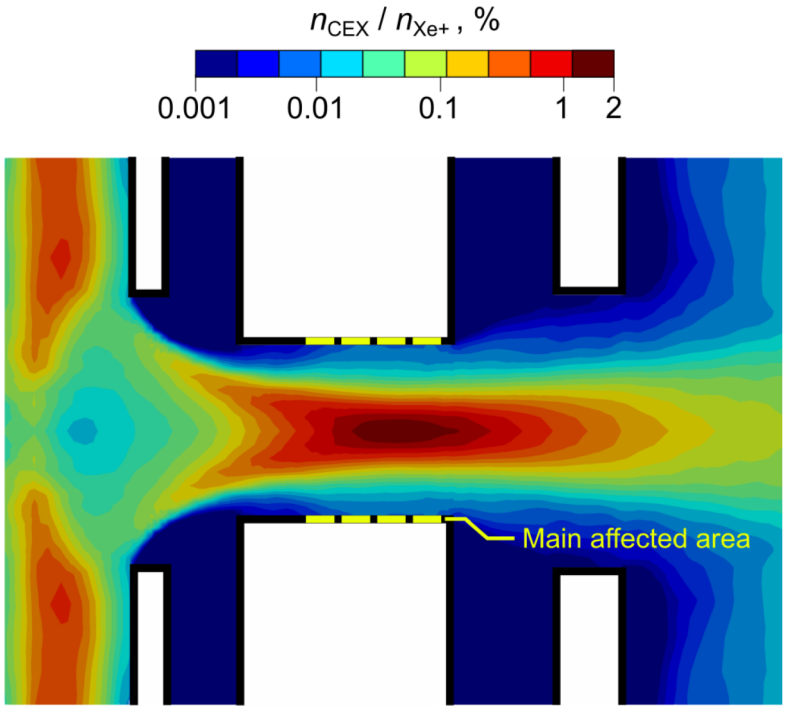


Figure 1.7 Percentage of CEX ions of results presented in Fig. 1.6. From Maigler, Maaß, *et al.* [10].

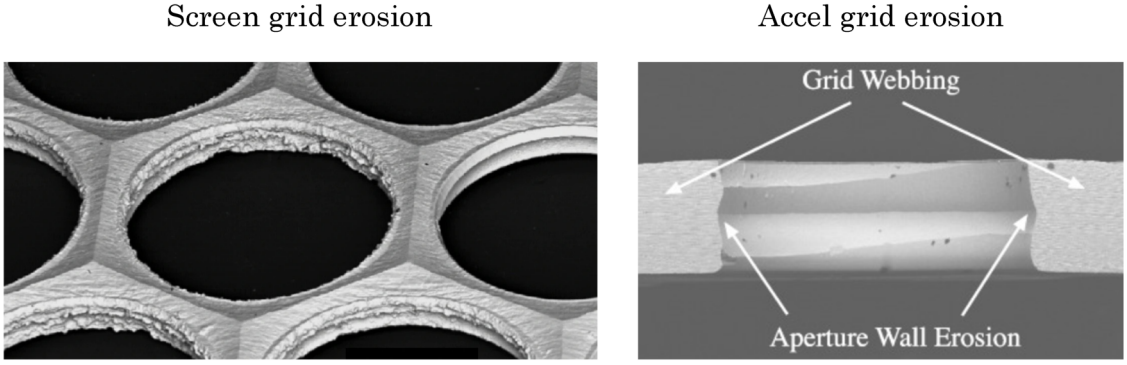


Figure 1.8 NSTAR thruster screen and accel grid erosion after 8200 h operating time. From: Polk *et al.* [11].

different operating times of the accel grid are shown in Figure 1.8. After 30 000 h of operation, shown in Figure 1.9, the pits responsible for electron backstreaming are clearly visible in the latter figure. In a similar manner, erosion of HET discharge channels is driven by plasma sputtering of the chamber walls, significantly reducing the thruster's performance over time.

Compared to RITs, HETs feature shorter lifetimes since the erosion rates are larger which yield more aggressive sputtering of the discharge channel. Exemplary characteristic erosion structures of various HET models that underwent endurance testing are illustrated in Figure 1.10. Specifically for HETs, the actual plasma-related phenomena responsible for discharge channel erosion are not well understood

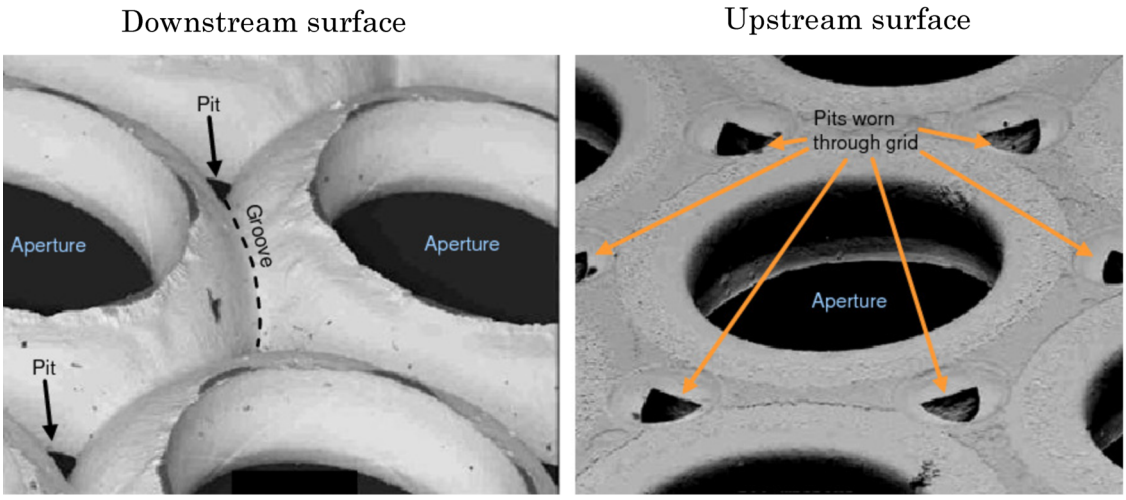


Figure 1.9 NSTAR thruster accel grid *pit* and *groove* erosion after 30 000 h operating time. From: Wirz, Anderson, Goebel, *et al.* [12].

due to the complex plasma-wall interaction and phenomena such as "spokes" taking place, including the fraction of ions impacting the channel, with estimations ranging up to 40 % [13].

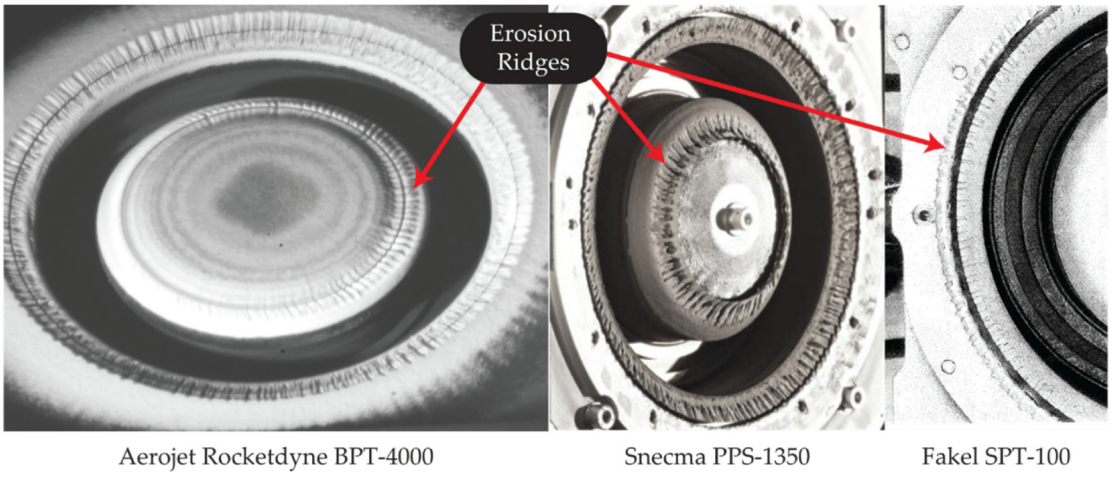


Figure 1.10 Various HET erosion exposures after endurance testing. From: Brown and Walker [14].

The sputtering rate is a highly sensitive material property and may locally change due to the plasma sheath[5], incident ion angle and energy, surface roughness, and other parameters. This has lead to extensive experimental and numerical efforts in order to characterize and predict sputtering rates. Researchers in the field of material science are attracted to develop ceramics with low sputtering yields while

[5]Bounded plasmas experience higher electron flux at the walls due to the electrons' greater mobility (i.e., lower mass). This results in a negative charge buildup on the walls and the formation of a plasma boundary layer known as the *sheath*, which contains a higher ion number density.

maintaining the features of currently used materials such as boron nitride [14, 15]. However, understanding the physical phenomena occurring within HET discharge channels and the plasma sputtering process remains a challenging task. The erosion process for RIT grids is better understood and improvements have already been implemented by adding a third neutrally charged grid behind the accel grid, reducing the *pit* and *groove* erosion of the accel grid. Additionally, optimized materials, such as graphite, have been successfully implemented to decrease the total sputter yield.

Nonetheless, detailed understanding of the various processes and interactions taking place on the atomic length and time scale are subject to discussions, in particular the timeframes and effects of the thermal spike and collision cascade initiated after the ion impact. Sparse research has been published on the topic of numerical modelling of EP materials subjected to ion bombardment. For this reason, the present work is concerned with a comprehensive molecular dynamics (MD) study of the most commonly used propellant, xenon, impacting commonly used EP materials, specifically of HETs and RITs.

The primary objectives are twofold, with the first one to give insight on the thermal spike model and atomic scale collision cascade after the impacting ion has entered the surface with a specific impact energy and angle. Secondly, the actual sputter yields shall be predicted and compared to experimental data, bridging the gap to practical applications in the real world.

1.2 Problem statement

In detail, the objective of this work is to develop an atomic-scale numerical model for the simulation of xenon ion impacts on three typically employed thruster materials; namely titanium, graphite, quartz as well as one experimental material, silicon carbide. Modeling of the thermal spike and collision cascade with the resulting ejection of atoms and molecules shall give insight into the process of plasma sputtering, change of local material properties near the surface, and sputtering yields. Moreover, parametrized impact conditions are investigated with variations of the ion impact energy and angle.

Most of the literature on numerical work in this area, as outlined in the following section, employs the so-called primary knock-on atom technique (PKA). Here, the entire kinetic energy of the impacting ion is assumed to be transferred to the PKA, which initializes the collision cascade, therefore ignoring the entire subsquent interactions between the ion and target atoms. For high energy cases, this impact energy is assumed to be entirely transferred a region of the electronic subsystem,

which then interacts and relaxes due to interactions with the lattice through the electron–phonon coupling. Compared to these approaches, the simulations performed in the present study capture the full atomic interactions. This includes hybrid potentials entailing the interactions between the target atoms themselves *and* between the impacting ion and the target atoms. Furthermore, the ion is allowed to interact with the electronic subsystem of the target and is randomly launched onto the target, ensuring a statistically more realistic approach compared to a complete transfer of momentum to one single PKA.

To summarize, the TTM-MD technique is employed, coupled with with specialized considerations applied for the interatomic potentials, numerical boundary conditions, and electron-phonon coupling in order to accurately capture the physical phenomena of plasma sputtering.

1.3 Literature review

Because there is limited amounts of research available specifically on TTM–MD simulations of EP plasma sputtering, this literature review includes publications from diverse fields where similar analyses were performed.

It is important to recognize that researchers can only model specific aspects of a complete thruster system numerically due to the complex interactions between various physical phenomena, each with different sensitivities, time, and length scales. This limitation similarly applies to experimental studies, where the focus is typically confined to the measurement of particular parameters, for instance the sputtering yield or electron number density. Given the ab-initio nature of molecular dynamics (MD) simulations, it is essential to carefully select and detail initial conditions. These conditions must be derived from high-resolution simulations of the plasma system and require a thorough review of the existing literature on near-wall plasma behavior and material properties, as the main parameters apart from the material properties governing the sputter process are the ion's impact angle and velocity. Building on this foundation, fully-kinetic Particle-in-Cell (PIC)[6] plasma simulations are necessary, since they can resolve the electron sheath near the wall and accurately represent the non-equilibrium kinetic energy distributions of electrons. Over the past three decades, various advanced models have been put forward to enhance the physical realism of these simulations. These enhancements include the incorporation of detailed unstructured grids for thruster

[6]In classical PIC, electrons are assumed to be isothermal and the plasma in (electrostatic) equilibrium according to the Boltzmann relation.

geometries, secondary electron emission (SEE) from wall surfaces, single- and double-ionization events, CEX, MEX processes, as well as Direct Simulation Monte Carlo (DSMC) collision models.

One of the first 2-D axisymmetric simulations of ion thruster grid erosion were reported by Bond and Latham [16] and Peng *et al.* [17]. Ira *et al.* [18] published among the earliest results using the nowadays de-facto standard code `CEX2D` developed by NASA's Jet Propulsion Laboratory (JPL) for RITs. Farnell *et al.* [19] present results of their general-purpose RIT 3-D code `ffx`, including geometrical erosion and life time predictions of grids. A modified version of `CEX2D` was used by Wirz, Anderson, and Katz [20] to validate the code for RIT lifetime prediction, using the data from the `NSTAR` thruster. A review of codes and tools developed in the 1990s and 2000s is given by Kalentev *et al.* [21]. Parametric studies on RIT grids such as the electron backstreaming problem and eroded grid influence on thruster performance were carried out by Emhoff and Boyd [22]. In a landmark paper by Wirz, Anderson, Goebel, *et al.* [23], the drastic improvements by mounting a third *decel* grid on electron backstreaming and grid erosion of the *accel* grid are discussed. In the recent decade, however, the focus of published literature on EP erosion seems to have gravitated towards HET, which will be described in the following paragraph.

Comprehensive studies on HETs that are focused on discharce channel erosion employ PIC with either Monte-Carlo Collisions (MCC) or DSMC for the plasma and semi-analytical erosion yield models. One of such were carried out by Cheng [24], illustrating excellent agreement with experimental data up to 1500 h of operation. Comparable results were obtained by Koizumi *et al.* [25] for operating times up to 2000 h, employing a similar approach. Cho *et al.* [26] put forward one of the first publications performing simulations with a fully-kinetic PIC-DSMC code. They were able to obtain small deviations from measured thruster performance and implemented a simplified erosion model. Cao *et al.* [27] exercised extensive numerical analyses of pre-ionization effects on discharge channel erosion, demonstrating that high pre-ionization ratios increase the ion incidence angle. A long-life low erosion HET was developed by Giannetti *et al.* [28], targeting thrusters with anisotropic magnetic field topologies. Modeling plasma and discharge channel plasma-wall micro-structure interaction numerically using the ray-tracing method was thoroughly analyzed by Schinder *et al.* [29], thus providing among the earliest insight on atomic sputtering in HET discharge channels. Recent advancements include a study by Passet *et al.* [30], where they coupled the `HYPICFLU2` code to a sputtering model particularly tuned to Xe-BN-Si_{02} interaction. They conclude that sputtering might also occur due to thermal spikes produced by heavy ion irradiation,

resulting in local evaporation of the lattice. Furthermore, it is assumed that the wall temperature itself may have a larger influence on yields of eroded material than is commonly presumed. They refer the reader to the thermal spike model[7] suggested by Parida *et al.* [31] for HET based on their experiments, originally proposed by Dessauer [32], and modified by Toulemonde *et al.* [33]. Finally, Jenkins [34] summarize the activities of erosion modeling of the XR-5 thruster in their institution, giving insights on the advancements and methods used in the industry for predicting HET discharge channel erosion. Due to their higher erosion rates compared to RITs, HETs are still an area of active research for numerical modeling.

Industrially speaking, plasma sputtering has become an important process for manufacturing hard disk drives [35], semiconductor manufacturing [36, 37], thin-film transistors [38–40], and scanning electron microscopy (SEM) [41, 42]. This complex process has attracted researchers to extend or adapt the classical MD technique, resulting in sophisticated interatomic potentials, direct electron, and additional force field models. Kim, Lee, *et al.* [43] reported one of the first molecular dynamics (MD) simulations of plasma sputtering while Prskalo *et al.* [44] investigated sputtering using Ar^+ ions with energies ranging from 20 – 1000 eV. Temperature effects on self-sputtering yields were studied by Metspalu *et al.* [45] for a range of ion impact energies and alternative approaches such as the Monte-Carlo (MC) method presented by Ono *et al.* [46]. Neyts and Brault [47] and Brault [48] published elaborate studies on multiscale MD simulations of plasma sputtering, and a follow-up paper [49] provided an even more detailed picture of the theory. Ahn *et al.* [50] give a thorough analysis of interatomic potentials when modeling inert gas impingment of He, Ne, and Xe. One of the first works on MD simulations modeling the irradiation of graphite by fast neutrons in nuclear reactors was performed by Christie [51] and a in a follow-up publication, Christie *et al.* [52] emphasized on the lack of a thermal spike region in graphite, leading to lower sputter yields but permanent point defects. A TTM-MD model was developed by Phillips *et al.* [53] for the simulation of the insulator quartz, and they conclude that the rather simple description of the electronic subsystem in non-metallic compounds is still able to substantially improve the simulations compared to “bare” MD simulations.

Ions with atomic mass greater than C and kinetic energy above the MeV range are referred to as *swift heavy ions* (SHI), with electronic stopping[8] power dominating

[7] The TSM concept is built on the assumption that a small region of the discharge channel wall evaporates due to ion irradiation locally energizing (i.e., temperature increasing) the surrounding atoms, also by means of electronic stopping.

[8] Due to inelastic collisions with electrons and subsequent transfer of kinetic energy, the impacting ion loses energy with each collision within the collision cascade.

over nuclear stopping [54]. In this scenario, electronic stopping can be analytically described by the formula of Bethe [55], but has to be modified for impact energies below 100 keV [56]. MD simulations of these cases inherit similarities of plasma sputtering, but require additional models to account for electronic stopping. Interestingly enough, with increasing energy, the electronic stopping decreases and the penetration depth becomes larger. Rymzhanov *et al.* [57] and Abdullaev *et al.* [58] published articles on numerical analyses of damage inducing SHI using MD simulation, while Lang *et al.* [59] reviews advances of modelling SHI irradiation of silica. A shortcoming should be addressed in this review, since most of the mentioned numerical studies employ one of two types of simplifications for instantiating the ion impact. Both have in common that they completely omit the presence of the ion in order to avoid complicated hybrid interatomic potentials describing the interaction between the target atoms themselves and additionally between the ion and the target atoms. The first approach is to initiate one or multiple primary knock-on atoms (PKAs) based on the kinetic energy of the impacting ion. The second one is often used in very high energy cascades with impacting energies in the MeV regime. Here, a specific (uniformly distributed, cylidrical) electron temperature profile is set at $t = 0$, assuming that the fast ion only interacts with the electronic subsystem, releasing its entire energy into it. The present study includes the impacting ion, the electronic subsystem, and the hybrid interaction potentials mentioned before.

The cornerstone providing reference data for sputter yields are sophisticated experiments carried out by researchers and engineers working on EP thrusters, fusion reactors, and ion-matter interaction related fields. For titanium, the detailed study from Tartz, Heyn, Bundesmann, Zimmermann, *et al.* [60] was taken advantage of, providing invaluable data for all the investigated impact energies and angles analyzed in the present study. Nakano *et al.* [61] provided similar datasets for graphite. The low keV irradiation range of xenon ions on quartz is not a well studied regime, however, some data for certain angle-energy combinations could be found, including the work from Tartz, Heyn, Bundesmann, and Neumann [62], Nenadović *et al.* [63], and Yalin *et al.* [64]. The same is true for silicon carbide, where only the estimated data from Ecke *et al.* [65] could be used as a reference. Detailed reviews of sputtering studies are given by Yim [66] and Polk [67], focusing on xenon irradiation of thruster compounds.

Finally, the work of Ziegler *et al.* [68] should be mentioned, who provide the freely available software TRIM–2013, which is used as a reference for comparison of the sputter yield and penetration depth with the MC method. After reviewing the literature on EP erosion, plasma sputtering, and SHI, it is evident that the

topic of the present study is situated in a dynamic and vibrant research area. Ongoing advancements and findings from theoretical, semi-analytical and experimental publications presented in this literature review will greatly add to the outcomes of this thesis.

Keep your eyes on the stars, but remember to keep your feet on the ground.

— T. Roosevelt

2 Theory of ion beam sputtering

Contents

2.1 Temporal evolution of the sputtering process 19
2.2 Two-temperature model 22
2.3 Nuclear and electronic stopping 22
2.4 Synopsis 25

Surfaces subjected to ion irradiation undergo a cascade of energetic displacement on the atomic scale. A schematic of this process is shown in Figure 2.1, outlining the kinetic energy of the impacting ion, prompting various aftereffects. The stopping of ions in matter depends on various different factors and is still not conclusively understood due to the local electronic excitation, ionization, and material specific melting or evaporation occurring inside the lattice near the surface [33].

In addition to the type of ion and substrate material, the sputtering process and developed models describing the occurring phenomena are significantly influenced by the kinetic energy of the impacting ion. The impact energies encountered by surfaces exposed to ion irradiation in HETs and RITs are located in the regime of few hundreds of eV up to 2 keV, depending on the operating acceleration potential [70].

2.1 Temporal evolution of the sputtering process

Based on the spatial coordinates and impact angle of the ion, a collision with the target occurs within the first few layers of atoms, initially with a single atom referred to as primary knock-on atom (PKA). During the first 10 fs of the primary knock-on

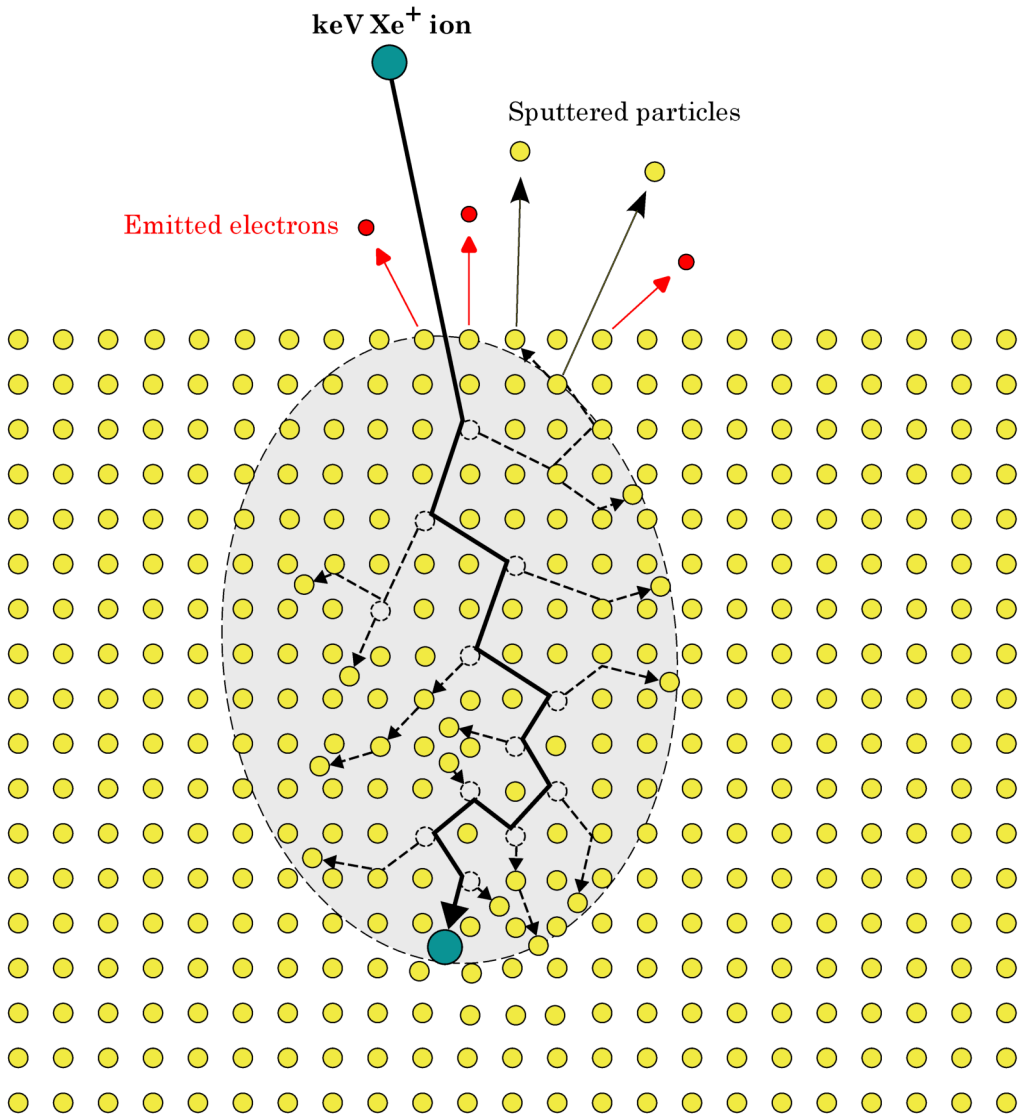


Figure 2.1 Schematic of knock-on collision cascade by low keV ion irradiation dominated by nuclear stopping. The affected lattice volume is indicated by the grey area. The primary ion trajectory is denoted by the solid black line; secondary, tertiary, etc. displacements are denoted by the dashed lines. Since the kinetic energy of the impacting ion is much higher than the displacement energy threshold, permanent defects are induced. Energetic, non-primary collisions close to the surface of the lattice leads to sputtering of atoms, and, depending on the target material, SEE. Schematic based on Fig. 2 from Volkert and Minor [69].

event, a portion of the ion's energy is deposited to *primary* electrons through inelastic collisions, and some atoms within the vicinity of the xenon ion are ionized through electron cascade thermalization. Highly energetic electrons may be emitted to the ambience in the form of SEE. Within the subsequent few hundreds of femtoseconds, the collision process repeats and produces secondary, tertiary, etc. electrons, while

the impacting ion continues to collide with other atoms through elastic collisions. Within this timeframe, electronic bombardment of surrounding atoms results in the so-called *electronic thermal spike* and primary lattice atoms start to collide with other atoms, initiating the formation of energetic *phonons*[1] that lead to an *atomic thermal spike*. The latter have the potential to eject lattice atoms if the transferred collision energy is above the threshold displacement energy (TDE). The peak temperature is reached within the first picoseconds after initial collision of the ion with the PKA. Due to the investigated impact energies ranging up to only 1.5 keV, the *electronic thermal spike* is expected to not be as pronounced as the *atomic thermal spike*. Depending on the target material, the ion comes to rest within the first few picoseconds after the PKA event, osing all it's kinetic energy through inelastic collisions within the target. The electronic subsystem continues to interact with the lattice through electron-phonon coupling. Energetic phonons transport the locally high kinetic energy of individual atoms outwards through the target accompanied by a shockwave and rapid heating of the affected lattice region well beyond the melting or sublitemperature, as well as cooling of the electronic subsystem through electronic friction with atoms, until both systems have reached thermal equilibrium.

Sigmund [71] emphasizes that knock-on sputtering, which is the primary sputtering mechanism of metals in the low keV regime, can be categorized into three different knock-on sputtering types:

1. **Single-knock-on**: Results in the ejection of secondary atoms close to the target surface without sufficient energy to initiate cascades of sputtered atoms.

2. **Linear cascade**: Recoil atoms receive enough energy to procude a linear cascade of knock-on atoms that might be ejected, however, collisions with the affected lattice volume remain sparse.

3. **Spike regime**: Atoms in the affected lattice volume are subject to thermal excitation, producing a high temperature zone with melting, gasification, and randomly ejected atoms.

Assigning a certain knock-on sputtering type before carrying out simulations or experiments is complicated by the dependency of the ion-target combination. Thus, it has to be asserted that the employed numerical models and experimental equipment are capable of capturing these different phenomena when analyzing these scenarios.

[1] Excited lattice interactions through random (vibrational) interaction.

2.2 Two-temperature model

In order to describe the interactions between the electronic and the atomic subsytem as well as their respective temporal temperature, the TTM model was developed by S.I. Anisimov [72]. Since its introduction, further source terms and improvements have been incorporated to account for various additional effects, which will be discussed in the chapter illustrating the employed methodology, 3. The TTM model is built upon the assumption that a thermal non-equilibrium is rapidly established as soon as high specific energy inputs excite the system of valence electrons due to the markedly different inertia between the lattice atoms and electrons. A necessary presumption is that the valence electrons feature relatively free movement within the lattice and can be regarded as an electron gas. In most scenarios, such as ultrafast laser or SHI ion irradiation, the electronic subsystem heats up to initially much higher temperatures than the lattice subsystem. Thermal relaxation between the two systems takes place through interaction between electrons and lattice atoms until an eventual equilibrium temperature is reached. The two governing equations of the TTM model are written as:

$$C_e \frac{\partial T_e}{\partial t} = \nabla \left(\kappa_e \nabla T_e\right) - g_p \left(T_e - T_l\right) + S(\mathbf{x}, t) \,, \tag{2.1}$$

$$C_l \frac{\partial T_l}{\partial t} = \nabla \left(\kappa_l \nabla T_l\right) + g_p \left(T_e - T_l\right) \,, \tag{2.2}$$

where C is the heat capacity, T is the temperature, g_p is the electron-phonon coupling factor, κ is the thermal conductivity, and $S(\mathbf{x}, t)$ a source term. The subscripts e and l denote electronic and lattice quantities, respectively. Eqns. (2.1)(2.2) can be regarded as heat diffusion equations, describing the temporal and spatial transport of heat based on initial conditions. In ultrafast laser and SHI applications it is common practice to include a (spatially and temporally varying) source term $S(\mathbf{x}, t)$ in Eq. (2.1) to account for processes that only excite the *electronic subsystem* due to femtosecond laser exposure or collision cross sections of MeV ions indicating that in this particular energy regime, collisions and thus energy transfers are occurring mainly with electrons.

2.3 Nuclear and electronic stopping

As described earlier, the impacting ion interacts with both the lattice and the electronic subsystem. With increasing kinetic energy of the ion, the fraction of inelastic collision events with the electrons increase, significantly altering the

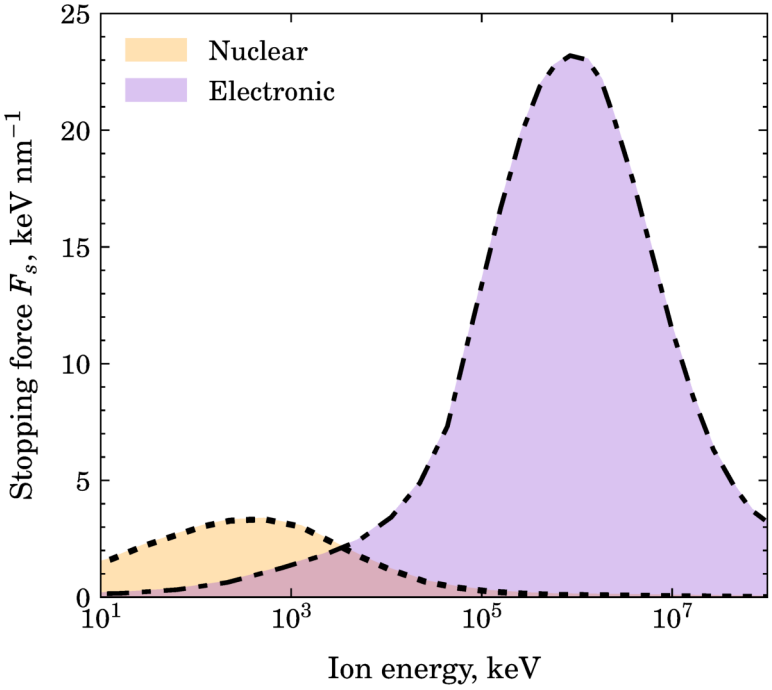


Figure 2.2 Stopping force of Au^+ ions iraddiated onto SiO_2 substrates [73].

ion trajectory through the bombarded substrate, while elastic collision events with lattice nuclei are decreasing. The *material stopping force* F_s is defined as the ability of matter to reduce kinetic energy of the impacting ion per unit path length, expressed as

$$F_s(E_k) = -\frac{\partial E_k}{\partial x}. \tag{2.3}$$

As the ion continues to collide with the substrate matter, the collision cross-section σ and stopping force F_s reach their maximum depending on the instantaneous kinetic energy of the ion. In MeV irradiation, this occurs just before the ion comes to rest, which is referred to as the *Bragg peak*. However, in the case of low keV bombardment, the stopping force is the highest at the beginning of the collision cascade. An exemplary plot highlighting the energy-dependent stopping force of SiO_2 exerted on Au^+ ions is displayed in Figure 2.2.

To understand the kinetic energy loss through nuclear stopping, one usually starts from the classical elastic scattering model [74]. One important assumption within the recoil process is the conservation of angular momentum according to

$$V(r_{ij}) = \frac{1}{4\pi\epsilon_0}\frac{Z_1 Z_2 e^2}{r_{ij}}\varphi\left(\frac{r_{ij}}{r_s}\right). \tag{2.4}$$

In Eq. (2.4), V is the interatomic (Coulomb) potential, ϵ_0 is the vacuum permittivity, r_{ij} is the distance between the two colliding nuclei, e is the elementary charge, Z_i

is the $i-$th atomic number, φ is the screening function, and r_s is the screening radius. The screening radius and screening function account for shell electrons screening the atomic nuclei from each other. Biersack and Ziegler [75] developed the following expressions for r_s and φ, respectively:

$$r_s = r_0 \left(Z_1^{0.23} + Z_2^{0.23}\right)^{-1} , \tag{2.5}$$

$$\varphi(x) = 0.1818e^{-3.2x} + 0.51^{-0.9423x} + 0.2802e^{-0.4023x} + 0.02817e^{-0.2016x} . \tag{2.6}$$

In Eq. (2.6), r_0 denotes the Bohr atomic radius ($r_0 = 53\,\text{pm}$) and $x = r_{ij}/r_s$. The determination of an analytical model describing friction with the electrons throughout a wide range of energy regimes proved difficult, since collisions and state changes of the ion are much more frequent than interactions with nuclei [56]. A popular model describing high energy electronic stopping is the model proposed by Bethe [55]. It is applicable to charged particles with $E_k > 100\,\text{keV}$ and describes the electronic stopping force as a function of the mean excitation energy I as

$$\begin{gathered} F_s(I) = \frac{4\pi n_e z^2}{m_e c^2 \beta^2} \left(\frac{e^2}{4\pi\epsilon_0}\right)^2 \cdot \left[\ln\left(\frac{2m_e c^2\beta^2}{I(1-\beta^2)}\right) - \beta^2\right] \\ n_e = \frac{N_A Z \rho_M}{A M_u} \qquad \beta = \frac{v}{c} \end{gathered} \tag{2.7}$$

where m_e, c, n_e, v, A, and M_u denote the substrate electron mass, the speed of light, the substrate electron number density, the impacting particle velocity, the substrate atomic weight, and molar mass constant respectively. An example of the electronic stopping force calculated by the Bethe model is shown in Figure 2.3 (left), which predicts a drastic decrease of $F_s^e < 100\,\text{keV}$, which was proven incorrect by several measurements [76, 77]. Therefore, corrections must be applied below this threshold ion energy.

The mean excitation energy can be roughly defined as

$$I = \Gamma \cdot Z \qquad \Gamma = \text{const.} = 10\,\text{eV} . \tag{2.8}$$

However, experimental measurements by Deasy [78] showed *nonlinear* dependency on the atomic number, which is illustrated in Figure 2.3 (right).

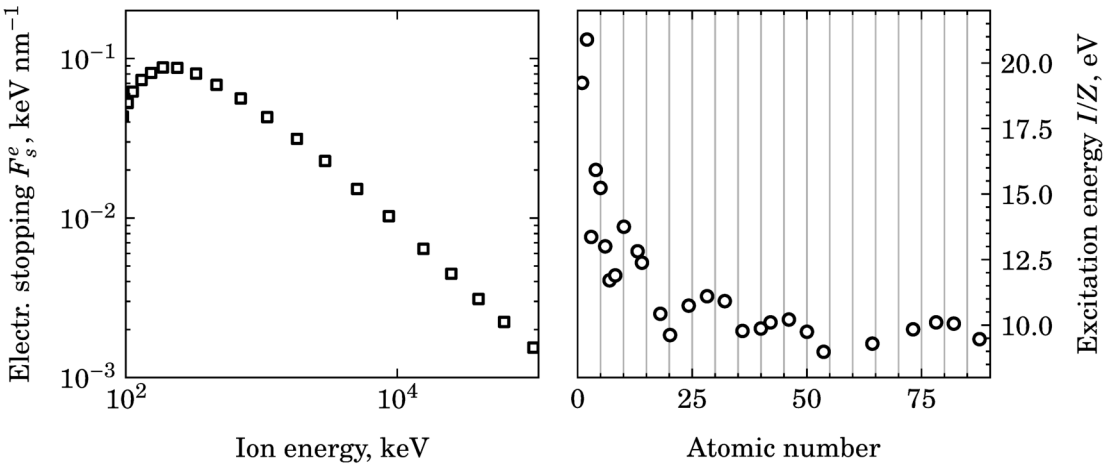


Figure 2.3 **Left:** Electronic stopping force of Al substrate irradiated by H^+ ions. **Right:** Mean excitation energy measurements (see [77]).

2.4 Synopsis

This chapter presents a comprehensive theoretical analysis of the physical phenomena associated with ion sputtering. Various models that describe the sputtering process across different spatial and temporal dimensions are introduced. The relationships between these models and their corresponding mathematical formulations are portrayed, with detailed discussions on three key models: the thermal spike model, the collision cascade model, and the TTM model. Furthermore, the chapter evaluates the capacity of these theoretical frameworks to characterize and quantify the underlying phenomena, while also addressing their limitations in relation to specific impact energies and temporal scales.

Experience without theory is blind, but theory without experience is mere intellectual play.

— I. Kant

3 Methodology

Contents

3.1 Irradiation cases 27
3.2 Two-temperature molecular dynamics 30
3.3 Interatomic potentials 35
3.4 Computational details 38
3.4.1 Simulation framework 39
3.4.2 Numerical details 39
3.4.3 Deriving macroscopic and structural properties 46
3.4.4 Obtaining initial atomic configurations 47
3.4.5 Impact simulations 50
3.5 Synopsis 54

This chapter provides an overview of the simulated irradiation cases, the employed computational methods, and the customizations that were implemented into existing software. Furthermore, the mathematical and physical models, and computing techniques that build the foundation of the individual codes are outlined. The goal is to give the reader a comprehensive overview of the underlying methods and how the results of this thesis were produced.

3.1 Irradiation cases

Since xenon remains the most widely used propellant for EP today, the considered impacting ion is a singly-charged Xe^+ ion. In typical EP operation, Xe^+ ions account for more than 95 % of the ionized propellant [79], with traces of doubly-charged

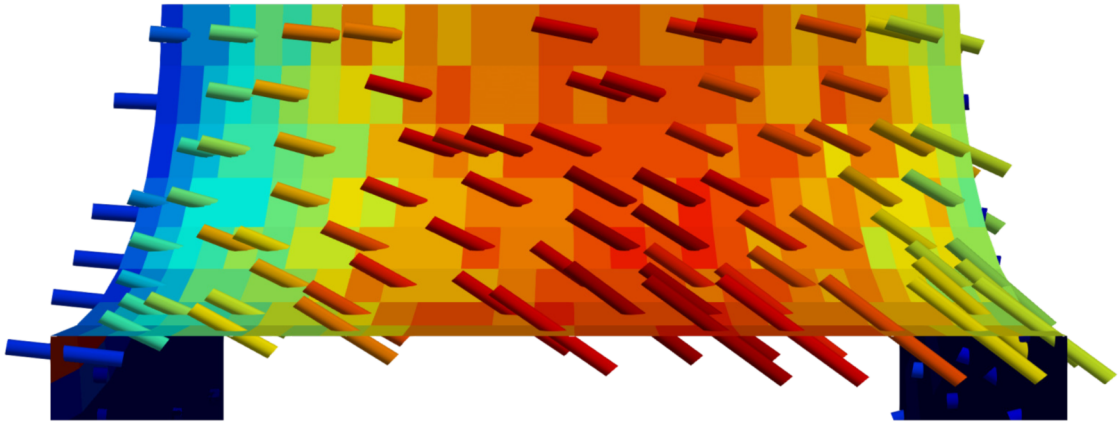


Figure 3.1 Surface properties of RIT accel grid from PIC-DSMC simulation. The length of the vectors indicates the ion impact energy, the surface coloring the ion impact flux, and from the vector itself the ion impact angle can be derived. Results are scaled by $E_k^{\max} = 1.5\,\mathrm{keV}$, $\beta_{\mathrm{imp}}^{\max} = 75\,\mathrm{deg}$, and $J^{\max} = 1.5 \times 10^{19}\,\mathrm{m^{-2}\,s^{-1}}$. From: Maigler, Maaß, *et al.* [10].

Xe^{++} ions. The irradiation cases are reasonably organized on the basis of the most important properties and impact parameters.

In Figure 3.1 a time-averaged result of coupled PIC-DSMC simulations by Maigler, Maaß, *et al.* [10] is illustrated. It outlines the impact flux, energy, and angle of Xe^+ ions on the surface of a RIT acceleration grid. Starting from there, the ranges of these quantities were determined and discretized. In RITs and HETs, typical operating conditions yield a maximum energy of $E_{Xe^+}^{\max} \approx 1.5\,\mathrm{keV}$, depending on the application and required thrust. Conveniently, there is experimental data available by Tartz, Heyn, Bundesmann, Zimmermann, *et al.* [60], where sputter yields from $0.2 - 1.4\,\mathrm{keV}$ and $0 - 85°$ incidence of Xe^+ ions on Ti targets were obtained. This data is ideal for validating the established numerical model for the titanium case.

Another commonly used material in RITs is graphite[1] which features, according to the data of Nakano *et al.* [61] an excellent yield of just $0.8 - 1$ atoms/ion at 1 keV Xe^+ irradation and normal incidence, roughly 4×lower than the yield of Ti and is preferably used in RIT accel grids. Quartz (SiO_2) enjoys applications in HET DCs and casings of RITs due to its suitable dielectric properties and exhibits sputter yields similar to Ti at normal incidence [66]. Silicon carbide (SiC) is a semiconductor with great mechanical strength and may be a beneficial additive when used in compounds where the best physical properties of different materials are combined. In the study of Gascon and Barral [15], HET discharge chamber wall effects were analyzed, and a too high SEE yield observed, making SiC as a *standalone* compound

[1] In the form of amorphous, high density, and pyrolytic graphite, see Polk [67].

unfavourable for usage in these thrusters. Still, fundamental analysis of SiC can benefit the development of new compounds that combine the features of other materials with lower SEE yields such as BN (borosil).

The most important parameters which are the impact energy and the impact angle of the xenon ion were discretized by 5 and 4 values, respectively. For example, the minimum and maximum investigated values of the impact angle are 0 and 70 deg, and the chosen values between those are 30, 45, and 60 deg. The same approach was applied to the impact energy where the closest values based on the availability of experimental data were chosen. An overview of the parameters and their individual values due to discretization and imporant properties is outlined in Table 3.1.

Table 3.1 Overview of parameter properties.

Parameter	N_{param}	**Values**	**Notes**
Material	4	[Ti; C; SiO_2]	Commonly used materials in RIT grids and HET discharge channels
Impact angle β	5	[0; 30; 45; 60; 70] deg	0° corresponds to normal surface impact
Impact energy E_k	4	[0.2; 0.6; 1.0; 1.4] keV	Corresponds to a range of velocities[1] 27 – 61 km/s
Impact location x_l	5	Randomized impact	Due to channeling effects and *perfect* crystalline structures of initial MD configurations, unrealistic penetration depths may be predicted

The parameters corresponding to the quantities listed in Table 3.1 is given in Figure 3.2. Here, the impact location x_l is the (randomized) variation of axial $x-$ and $y-$ displacement from where the impacting ion is launched from. This procedure is important in order to avoid effects of channeling due to unrealistically perfect alignment of crystalline structures[3] relative to the ion's trajectory. For each impact scenario (i.e., target material, impact energy, and angle) 5 randomized simulations were carried out, where the launch position in $x-$ and $y-$ vector components were randomly varied. The distance between the ion and the surface of the target were kept constant at $\Delta z = 10\,\text{Å}$.

[2]Calculated from: $E_k = \frac{1}{2}mu^2 \quad \leftrightarrow \quad u = \sqrt{2E_k/(M/N_A)}$

[3]A further improvement is realized through initializiation of the MD structure using randomized crystals; for further details see Figure 3.11.

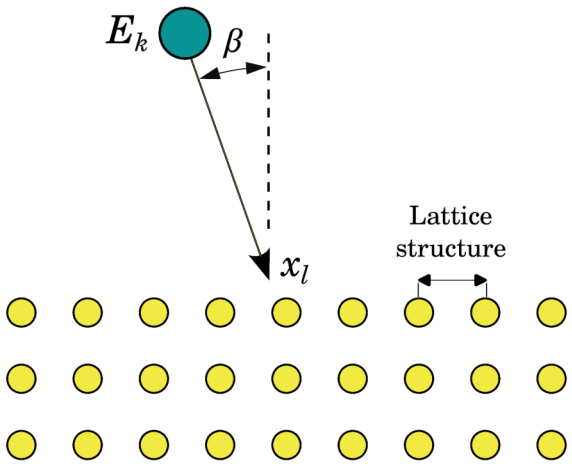


Figure 3.2 Schematic of impact parameters based on quantities outlined in Table 3.1. Due to randomized shifts of the ion's x and y positions at $t = 0$, the initial impact lattice impact position x_l changes each run.

3.2 Two-temperature molecular dynamics

MD is a powerful tool to directly model the trajectories of individual atoms or molecules. It comes at the cost of very high computational requirements when large systems of atoms are analyzed. The history of MD simulation goes back to the 1950s, where condensed matter and phase transitions of hard spheres [80] were analyzed. Improvements were implemented by Rahman [81] and in a landmark paper by Verlet [82], a stable temporal integration scheme as well as an efficient neighbouring list algorithm was proposed that is still used nowadays. Rahman and Stillinger [83] published one of the first works on simulating molecules instead of single atoms and the first publication concerned with MD simulation of a protein was authored by McCammon *et al.* [84]. Since then, many sophisticated models and methods have been implemented into the MD framework, making it an important tool to help understanding a variety of physical phenomena on the atomic scale. An elaborate overview of the history, current state, and future of MD simulation is outlined by Ciccotti *et al.* [85].

The basic idea of MD is to track the movement of single atoms and their interaction. The *ensemble* is a set of atoms, usually all atoms present in the simulation box, from which macroscopic properties such as the (ensemble) pressure, temperature, or density can be derived. One of the crucial parameters of MD is the interatomic potential $V(\mathbf{x}_i)$. It governs the interaction between each individual atom and produces a force, which (in classical MD) only depends on the distance to neighbouring atoms. It is usually implemented with a cutoff radius beyond which interactions are disregarded due to negligibly small forces from distant

atoms. The temporal evolution of the particle ensemble is performed using Newton's second law of motion:

$$\mathbf{F}_i = m_i \frac{\partial^2 \mathbf{x}_i(t)}{\partial t^2}\,, \tag{3.1}$$

where $\mathbf{F}$, $\mathbf{x}_i$, and t denote the force, spatial coordinate of the $i-$th atom, and time. To advance the simulation in time, i.e., to compute the next position $\mathbf{x}_i$ of the $i-$the atom using a discrete time step Δt, the previously mentioned fourth order accurate method proposed by Verlet [82] can be employed and reads as

$$\mathbf{x}_i^{t_n+\Delta t} \equiv \mathbf{x}_i^{n+1} = 2\cdot\mathbf{x}_i^n - \mathbf{x}_i^{n-1} + \frac{\mathbf{F}_i^n}{m_i}\Delta t^2\,. \tag{3.2}$$

In Eq. (3.2), the superscripts $n-1$, n, and $n+1$ indicate the previous, current, and next time step, respectively. Before any actual changes to the atomic ensemble are initiated through ion impacts, it is crucial to establish physically reasonable initial conditions of the ensemble. This step is referred to as *equilibriation* where at the beginning of the simulation a Maxwellian temperature distribution is applied to the ensembe through a randomized discrete sampling on individual atoms. This leads to unphysical contact forces present in the ensemble, which must be relaxed to ensure that the initial configuration is representative of the real behavior of the analyzed system. In order to accomplish this, an equilibriation procedure is performed to achieve a desired macroscpoic temperature by means of a specific *thermostat*[4] (usually the `nvt` ensemble) coupled to the ensemble. When several hundreds of thousands or more atoms are simulated, simple initial configurations might not be representative due to random and chaotic structures of real materials. This includes for instance polycrystalline grains in metals or honeycomb lattices in graphite.

In TTM-MD the TTM equations presented in Eqns. (2.1)(2.2) are coupled to the MD governing equation of motion as expressed in Eq. (3.1). The employed model used in this thesis is based on the TTM-MD model proposed by Duffy and Rutherford [86], which employs a Langevin-type equation of motion including a friction and electronic blast pressure term, given by the following governing equation:

$$\underbrace{m_i \frac{\mathrm{d}\mathbf{u}_i}{\mathrm{d}t}}_{\text{Motion}} = \underbrace{\mathbf{F}_i(t)}_{\text{Potential}} - \underbrace{\gamma_i \mathbf{u}_i}_{\text{Friction}} + \underbrace{\frac{\nabla P_e}{N_i}}_{\text{Electron pressure}}\,. \tag{3.3}$$

[4] **Thermostatting** is the process of adjusting the macroscopic temperature of the ensemble by (randomly) altering the translational kinetic energy of individual atoms to fit a desired Maxwellian distribution. Usually, a damping factor and time period are specified in order to minimize the introduction of artificial, unphysical errors into the system. The `nvt` thermostat enforces conservation of the number of atoms, fixed volume of the simulation domain – both quantities rely on periodic boundary conditions in all spatial directions – and a desired temperature of the ensemble. The damping parameter governs how aggressively the kinetic energy of atoms are adapted each time step.

In Eq. (3.3), the friction term $\gamma_i \mathbf{u}_i$ accounts for energy loss of the lattice atoms through friction with electrons in the lattice and may occur due to two processes, based on the kinetic energy of the individual nucleus. The first one includes electronic stopping if the individual atom exhibits a greater kinetic energy than the cut-off energy:

$$E_k^i > E_k^0 \approx 10\,\mathrm{eV}\,. \tag{3.4}$$

In other words, if the atom moves fast enough it loses kinetic energy through collisions with the electron gas. This may occur through primary and secondary atoms gaining enough kinetic energy by collisions with either the impacting ion or other fast PKAs. In the lower kinetic energy regime, only electron-atom interactions are considered through the coupling parameter g_p included in the term for γ_p. The described relations for γ_i in Eq. (3.3) can be expressed as [86]

$$\gamma_i \left(E_k^i > E_k^0\right) = \gamma_p + \gamma_s \tag{3.5}$$

$$\gamma_i \left(E_k^i \leq E_k^0\right) = \gamma_p\,, \tag{3.6}$$

where the subscripts p and s indicate electron-phonon interaction and electronic stopping, respectively. The electronic subsystem governed by Eq. (2.1) is solved on a cartesian grid using the finite-difference method (FDM). A schematic of the background grid is shown in Figure 3.3.

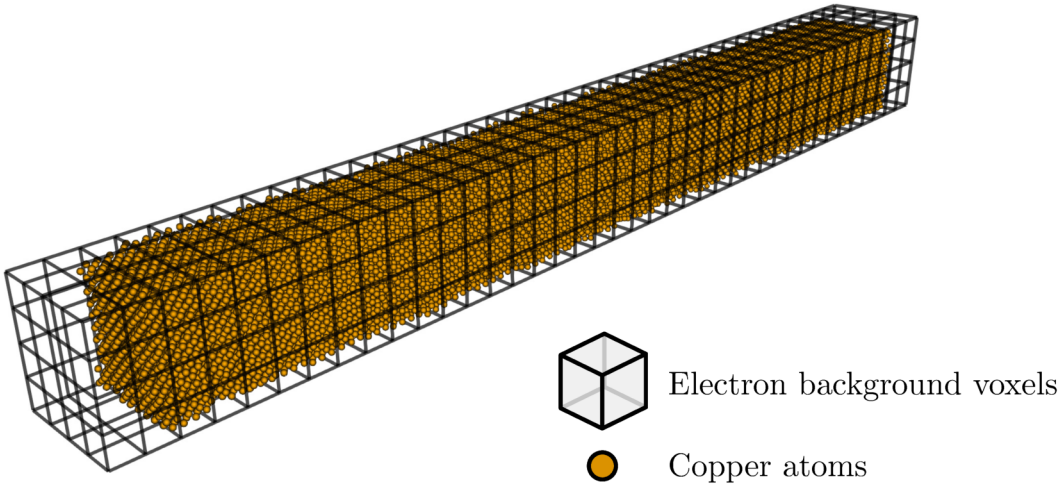


Figure 3.3 Schematic of electron background cells containing a slab of copper atoms. From: Maigler, Held, *et al.* [87]

Each electron background cell is referred to as a *voxel* and may or may not contain a certain number of atoms, which dynamically changes due to the movement of

individual atoms. If a certain threshold of atoms is reached within an electronic voxel, the voxel is activated and the local electron gas allowed to interact with the atoms based on Eqns. (2.1)(2.2). A schematic illustrating the adaptive electron voxels (AEV) is outlined in Figure 3.4.

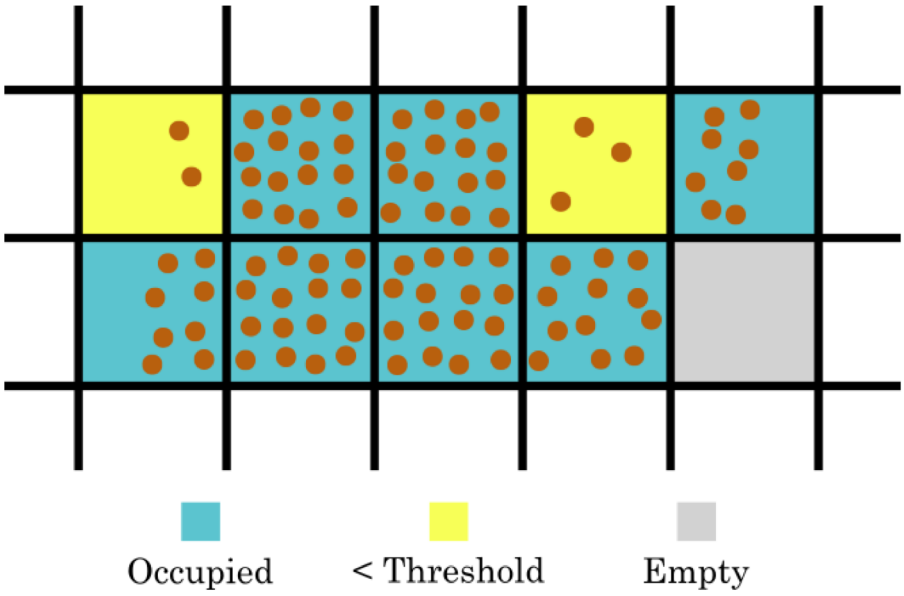


Figure 3.4 Schematic of AEV with different voxel states, based on the contained number of atoms. From: Maigler, Held, *et al.* [87]

The electron-phonon and electronic stopping parameters are calculated employing

$$\gamma_p = \frac{g_p V_i m_i}{3 n_i k_B} \tag{3.7}$$

$$\gamma_s = \frac{g_s V_i m_i}{3 n_i^* k_B} \tag{3.8}$$

with n_i, n_i^*, k_B, and V_i denoting the number of atoms in the i-th voxel, the number of atoms with $E_k > E_0$ in the i-th voxel, the Boltzmann constant ($k_B = 1.381 \times 10^{-23}\,\mathrm{J\,K^{-1}}$), and the i-th voxel volume, respectively. The electron-phonon coupling has been subject of extensive research since the introduction of the TTM by S.I. Anisimov [72] and depends on quantum-mechanical electron band interactions [88] as well as the electron temperature itself. Experimental determination of the coupling parameter is a difficult undertaking often involving complex setups, ultrafast lasers, and sophisticated measuring devices, for the characteristic length and time scales are in the nm and ps regime, respectively. Therefore, numerical modeling is essential and is mostly accomplished in the form of density function

theory (DFT), density of states (DOS) or Monte-Carlo (MC) techniques. One of the standard works providing electron temperature dependent coupling parameters $g_p(T_e)$ for a variety of metals was published by Lin *et al.* [89]. In their publication, they also provided electron temperature dependent values for the heat capacity C_e, which determines the maximum temperature that the ion impact may produce.

The electronic stopping parameter g_s can be found for different materials using the SRIM tables provided by Ziegler *et al.* [68]. The cutoff value below which only electron-phonon coupling is considered can be determined from the cohesive energy[5]. In the works by Duffy and Rutherford [86] and Zhurkin and Kolesnikov [90], a value of twice the cohesive energy of the respective material, for instance $E_0(\mathrm{Fe}) = 2{\cdot}E_c = 8.6\,\mathrm{eV}$, was employed. This corresponds to a cutoff translational velocity for iron of

$$E_0 = \frac{1}{2} m_i u_0^2 \quad \leftrightarrow \quad u_0 = \sqrt{\frac{2E_c}{M_i/N_A}} \approx 5000\,\mathrm{m\,s^{-1}} \tag{3.9}$$

below which effects of electronic stopping are assumed negligible. The remaining parameter in Eq. (2.1) is the electronic thermal conductivity κ_e and governs the spatial transport of heat throughout the electronic subsystem. There are several models available depending on the analyzed scenario with the most simple approach assuming $\kappa_e = \infty$ due to ballistic electrons[6] [92, 93], as the electronic timescale of heat conduction is much smaller than the timescale of atomic heat conduction $\tau_{\kappa_e} \ll \tau_{\kappa_l}$. However, this assumption is only valid for thin slabs with a thickness of few tens of nanometers and zero-dimensional (0D) analysis, where the Courant-Friedrichs-Lewy (CFL) condition [94] does not apply. The second approach is to assume $\kappa_e = \text{const.}$, which is valid for scenarios where the variations of T_e are minor in the system. Finally, when the case involves the existence of large local temperature differences in the order of at least few eV, an electron temperature dependent model should be utilized. A common model is the one suggested by Drude [95], which relates κ_e to C_e, the Fermi velocity u_F and the electron relaxation time τ_e as

$$\kappa_e = \frac{1}{3} u_F^2 C_e \tau_e \qquad u_F = \frac{p_F}{m_e} \qquad p_F = \sqrt{2 m_e E_F}\,, \tag{3.10}$$

where E_F is the Fermi energy. An alternative suitable for individual materials, if available, is to employ semi-empirical fits, which are capable of improving predictions at high electron temperatures [96, 97].

[5] The per-atom energy required to separate a lattice of atoms into free, neutral atoms.

[6] **Ballistic electron heat transport** refers to unrestricted transport of heat by unhindered, fast-moving electrons when their temperature is considerably higher than one of the atoms. The effect was first published by Landauer [91] to describe the unrestricted flow of charges in mesoscopic circuits.

3.3 Interatomic potentials

The most important quantity governing the interaction between individual atoms is the interatomic potential. The development of pair-wise and multibody potentials – recently also with the help of artificial intelligence (AI) – is a vibrant area of research since MD simulations have become a widely used tool that is nowadays extensively applied even in industrial projects.

The objective is to reproduce specific material properties by analytically and/or empirically fitting coefficients to the underlying potential terms. One of the earliest and most widely used type of potentials is the *Lennard-Jones* (LJ) potential introduced by Jones and Chapman [98], defined in 12–6 form as

$$V^{\mathrm{LJ}}(r) = 4\epsilon\left[\left(\frac{\sigma}{r}\right)^{12} - \left(\frac{\sigma}{r}\right)^{6}\right], \tag{3.11}$$

with ϵ and σ denoting the local minimum of potential energy and distance where $V(r) = 0$, respectively. Despite its simplicity, the LJ potential is capable of accurately predicting the behavior of (real) fluids throughout a wide range of pressures and temperatures [99–101]. It performs optimally when the constituent atoms exhibit symmetric, spherical shape and interactions can be considered in a soft repulsive-attractive fashion. The LJ potential cannot accurately model the atomic interactions if valence electrons or many-body interactions play an important role such as in crystalline elements (metals, graphite, etc.) or complex molecules [102].

In 1984, the foundation for the most popular group of potentials for metals and alloys was laid out by Daw and Baskes [103], who published their *embedded atom method* (EAM) based on DFT analysis. It builds upon the work of Finnis and Sinclair [104] (second moment bond theory), where a derivation of interatomic forces in metals is added based on potential *energy* or more specifically the electron density surrounding the individual atoms. The assumption is that these atoms are *embedded* into an gas of electrons, and the embedding energy can be expressed as

$$E_i^{\mathrm{emb}} = \xi_i\left(\rho_i^e\right) . \tag{3.12}$$

In Eq. (3.12), ξ_i and ρ_i^e are the embedding function and electron density of the i-th atom, respectively. ξ_i essentially governs the amount of required energy to embed an atom into the electron gas. The electron density is given by the expression

$$\rho_i^e = \sum_{j\neq i}^{N} \rho_j^e\left(r_{ij}\right) \tag{3.13}$$

and in order to avoid unphysical properties of the total embedding energy $\sum_i U_i^{\text{emb}}$, Eq. (3.12) must be extended with a potential describing pair-wise interaction of atoms [105], given as

$$\phi(r_{ij}) = \frac{1}{2}\sum_i \sum_j r_{ij}\,, \tag{3.14}$$

yielding

$$E_{\text{tot}}^{\text{emb}} = \sum_i \xi_i\left(\rho_i^e\right) + \frac{1}{2}\sum_i \sum_j \phi(r_{ij}) \tag{3.15}$$

when adding Eq. (3.14) to Eq. (3.12). Since in the EAM a spherically averaged, symmetric distribution of electron gas around nuclei is assumed [106], the potential yields good results for atoms exhibiting a similar shape such as copper. For angularly bonded atoms such as aluminum or metals loaded under strong shear, the assumption breaks down [107] and additional approaches must be implemented to account for locally varying electron densities. This lead to the development of the *modified embedded atom method* (MEAM) by Baskes [108] in 1987. In this version, the original EAM model was tailored with a modified pair potential

$$\phi(r_{ij}) = \frac{2}{z}\left\{E_i^{\text{emb}}\left(r_{ij}\right) - \xi_i\left[\rho_i^0\left(r_{ij}\right)\right]\right\}. \tag{3.16}$$

In Eq. (3.16), z is the number of adjacent neighboring atoms and ρ^0 is the background electron density for a reference structure (`fcc`, `bcc`, `hdp`, or `diamond`). The atom-wise energy of a specific reference structure is given by

$$E_i^r = -E_c\,(1+a^*)\,e^{-a^*} \tag{3.17}$$

where E_c is the cohesive energy and a^* includes a term for empirical quantities such as the bulk modulus and nearest-neighbor distance. A detailed overview of the mathematical framework of the MEAM is given by Baskes [109], where he clarifies that MEAM is an entirely *empirical* modification of the EAM aimed at including angular effects of asymmetric electron gas density distributions.

Another group of potentials are *reactive empirical bond order* (REBO) potentials. They are dedicated to producing force fields of carbon-based materials such as hydrocarbons, fullerenes, graphite, or graphene and were originally introduced by Tersoff [110] in 1988. Another significant milestone were the additional terms devised by Brenner [111] for improving the model for hydrocarbon compounds where close-distance reactions play an important role through addition of a LJ term. Finally, Stuart, Tutein, *et al.* [112] proposed the adaptive intermolecular

reactive bond order (AIREBO) potential that includes an additional bond order term that also considers torsion.

The governing equation for potential energy in the AIREBO equation is given by the expression

$$E_{tot}^{\mathrm{AIREBO}} = \frac{1}{2}\sum_{i}\sum_{j}\left[E_{ij}^{\mathrm{REBO}} + E_{ij}^{\mathrm{LJ}} + \sum_{k}\sum_{l}E_{ijkl}^{\mathrm{tors}}\right] \tag{3.18}$$

where E_{ij}^{LJ} is the usual long-range van der Waals interaction given in Eq. (3.11) and E_{ij}^{REBO} incorporates the attractive and repulsive components based on the bond order b_{ij}, given by

$$E_{ij}^{\mathrm{REBO}} = b_{ij}V_{ij}^{\mathrm{att}}(r_{ij}) + V_{ij}^{\mathrm{rep}}\,. \tag{3.19}$$

Building on the work of Brenner [111], the intrinsic long-range bond-order potential (LCBOP) for carbon, specifically suited for modeling carbon systems and graphitization was proposed by Los and Fasolino [113], based on bond order potentials from tight binding models (TBBOPs). The underlying problem, as described by Los and Fasolino [113], is long range interactions playing an important role in carbon systems, compared to similar systems such as in silicon. This is why mechanical properties predicted by REBO-type potentials deviate from experimental measurements. Moreover, they outline that even the improved AIREBO potential with an internal switching function fails to correctly describe interplanar repulsion as encounterd between graphene layers and present in graphite, yielding unrealistic structural defects. To overcome these shortcomings, Los and Fasolino [113] proposed to not include long-range interactions *only* for the nearest neighbors, while the short-range interactions are empirically fitted to predict correct binding and mechanical properties. For a detailed physical description of the mathematical framework, the reader is referred to the original publication [113].

Until now, only single element potentials (Ti–Ti, C–C) have been described. The modeling of multi-element systems such as encountered in silicon carbide and quartz requires additional considerations. In the present study, Vashishta-type potentials were found to perform best for both of these multi-element materials. Vashishta, Kalia, Rino, *et al.* [114] proposed a two-body/three-body potential for SiO_2 where the two-body part accounts for steric repulsion, charge transfer manifesting itself through Coulomb-type interactions, and charge-dipole interactions due to the large electronegativity of oxygen. The three-body covalent part includes angle and

distance dependent functions to describe the three-body interactions of O–Si–O and Si–O–Si. The basic form of their twofold potential is given by the expression

$$V^{\text{vash}} = \sum_{1 \geq i < j \geq N} V_2(\mathbf{r}_{ij}) + \sum_{1 \geq i \geq j \geq k \geq N} V_3(\mathbf{r}_{ij}, \mathbf{r}_{jk}, \mathbf{r}_{ik}) \,. \tag{3.20}$$

The two-body potential can be written as

$$V_2 = \underbrace{\frac{H_{ij}}{\mathbf{r}^{\eta_{ij}}}}_{\text{steric repulsion}} + \underbrace{\frac{Z_i Z_j}{\mathbf{r}}}_{\text{Coulomb interactions}} - \underbrace{\frac{0.5\left(\alpha_i Z_j^2 + \alpha_j Z_i^2\right)}{\mathbf{r}^4} e^{-\mathbf{r}/\mathbf{r}_{4s}}}_{\text{charge-dipole interaction}} , \tag{3.21}$$

where H_{ij} and η_{ij} are the strength and exponent of steric repulsion, respectively, α_i is the $i-$th ion's polarizability, and $\mathbf{r}_{4s}$ the decay length of polarizability. Three-body interactions are governed by the equation

$$V_3 = B_{ijk} f(\mathbf{r}_{ij}, \mathbf{r}_{ik}) \cdot p\left(\theta_{jik}, \overline{\theta}_{jik}\right) , \tag{3.22}$$

with $B_{ijk}, f(\mathbf{r}_{ij}, \mathbf{r}_{ik})$, and $p\left(\theta_{jik}, \overline{\theta}_{jik}\right)$ denoting the three-body interaction strength, bond stretching strength, and bond bending strength, respectively. The success of the Vashishta potential for SiO_2 lead to the development of a similar potential for SiC with modifications to the two-body and three-body parts of Eq. (3.22), taking advantage of the works of Keating [115] and Stillinger and Weber [116] for angle-dependent bonds. For details, the reader is referred to the publication of Vashishta, Kalia, Nakano, *et al.* [117].

3.4 Computational details

This section provides a comprehensive overview of the essential procedures involved in the simulation process, including the setup, execution, and subsequent postprocessing. Specific employed software tools are discussed along with detailed visualizations and descriptions of the initial and boundary conditions. A critical aspect of this study was the establishment of realistic initial conditions for the impact simulations. Utilizing an idealized atomic configuration as the target ensemble would have resulted in unphysical outcomes, underlining the importance of accurate initial condition modeling in ensuring the validity of the simulation results.

3.4.1 Simulation framework

The main three steps of the simulations performed in this work can be structured into

1. **Preprocessing**: Setup of the simulations.
2. **Solving**: Running the simulations.
3. **Postprocessing**: Evaluation of the produced data.

Preprocessing encompasses the drafting of input scripts (based on a validated template and parameters outlined in sec. 3.1). This is mainly performed with the versatile scripting language Python, allowing complex string and file input/output operations. In some cases involving direct interaction with the computing cluster, the Linux-native scripting language `bash` is used, as the cluster operates using `slurm`.

The utilized TTM-MD tool was LAMMPS [118], which is one of the most widely used open source software for running MD simulations due to its vast availability of additional packages, object-oriented programming implemented in C++, and performance. Specifically, the `ttm/mod` implementation from the `ttm` package is used, which is based on the publications of Duffy and Rutherford [86], Chen *et al.* [119], and Pisarev and Starikov [120]. The requirement of time steps much smaller than commonly utilized ones in MD in the realm of $\approx 1 \times 10^{-15}$ s as well as the necessary size of the atomic box with the aim to minimize pressure reflections at the periodic boundaries makes the use of a high-performance computing facility vital. For this thesis, access to the *HSuper* cluster[7] owned by the Universität der Bundeswehr Hamburg was kindly granted, allowing simulations to be performed on up to $128\,\text{nodes} \times 72\,\text{cores/node} = 9216\,\text{cores}$.

After the parametric simulations were performed, the large amount of produced data was prepared for postprocessing. Conveniently, LAMMPS allows the native export of data using the `vtk` library [122], which can be read in by the parallel-computing capable software ParaView [123]. Furthermore, all operations in ParaView can be recorded as script operations using Python, which makes parametric postprocessing convenient and fast.

3.4.2 Numerical details

Thermostatting

Since the simulation domain is small from a macroscopic perspective ($\Delta x_i < 0.1\,\mu\text{m}$), some special boundary conditions need to be applied to the ensemble. Generally

[7] At the time of installation in June 2022, HSuper was located at place 339 in the TOP500 list [121].

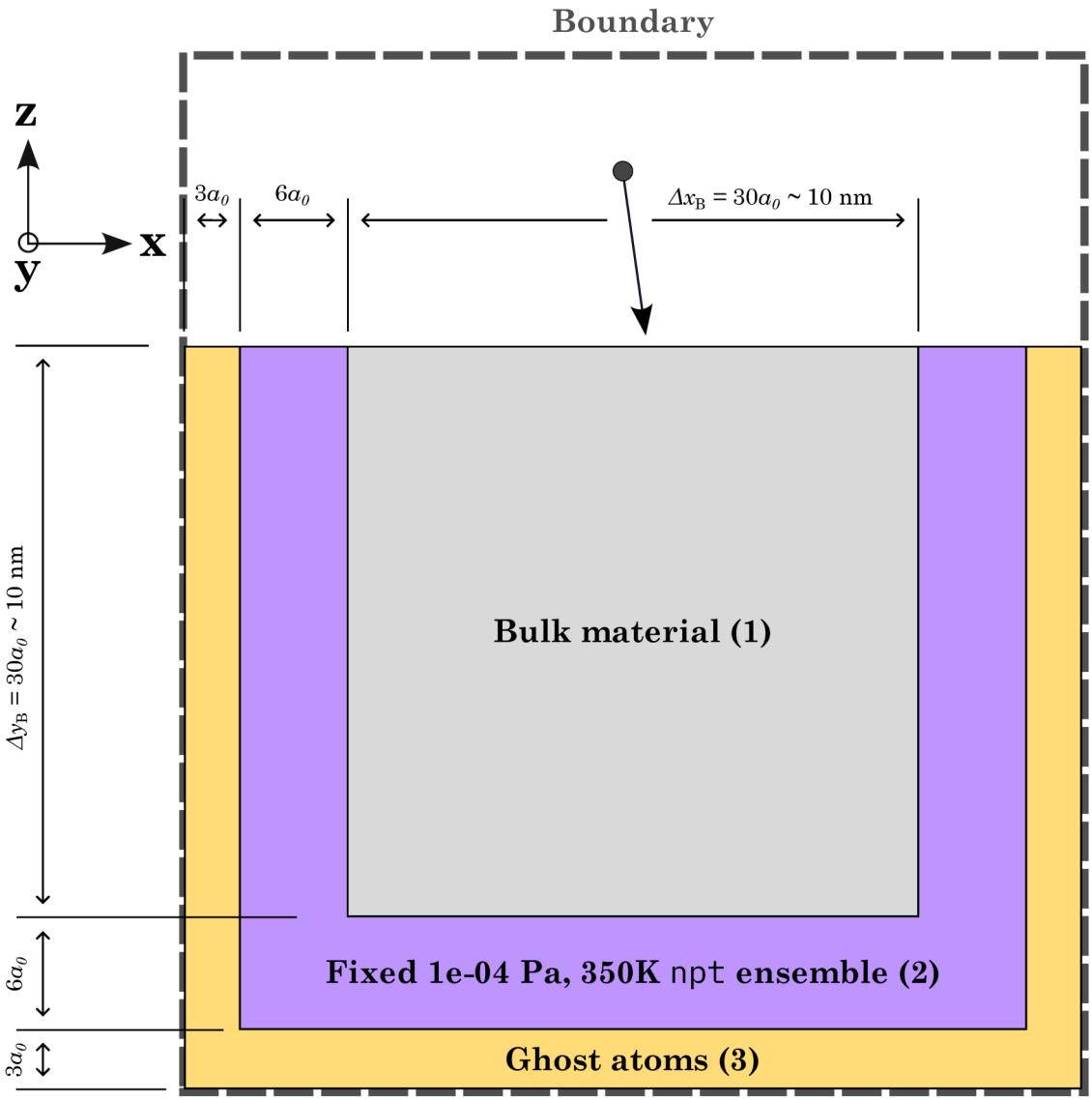


Figure 3.5 Schematic of different ensembles to avoid pressure reflections and atoms crossing periodic boundaries. Ensemble (1) is evolved using the `nve` thermostat, ensemble (2) held at 1 bar pressure and 300 K temperature employing the `npt` thermostat, and ensemble (3) are non-moving *ghost* atoms only allowed to interact with atoms of ensemble (2) through the potential.

speaking, MD simulations are usually carried out using periodic boundary conditions[8] necessary for employing classical thermo- and barostats. The same is true for the present work, where depending on the simulation step a combination of the `nvt`, `npt`, and `nve` thermostats was used. However, the impact of an energetic ion compels the formation of a pressure and temperature shock wave initiated at the penetration path of the ion and subsequently spreading through the bulk material

[8]Particles crossing a boundary condition, for instance `xlo`, will be injected at the opposite domain – in this example `xhi` – using the displacement vector $\vec{\mathbf{x}} = \mathbf{x}_{\mathrm{hi}} - \mathbf{x}_{\mathrm{lo}}$ with the same velocity vector.

at the speed of sound. This circumstance can lead to unphysical results if the shock wave is not dissipated sufficiently before it reaches atoms in the vicinity of a periodic boundary condition, because the reinjection of energetic atoms on the opposite side would eventually lead to a compression of the bulk material. In experiments, the dimensions of the target are at least several magnitudes greater than in simulations, allowing for enough time and space to dissipate the shock wave. Numerically, this may be achieved in two different ways.

The first is the introduction of a spring-damper system to each side of the bulk material, where the spring constant K and damping parameter b must be obtained from the material properties. This method is often used in continuum finite element method (FEM) applications, where beams of spring-dampers act as artificial dissipating media. However, attaching a chunk or individual atoms with one or more springs on the one hand introduces unphysical forces to the system and on the other hand leads to small errors in each time step, as in reality atoms translate and rotate freely.

For this reason the second way is chosen, involving another ensemble of atoms surrounding the inner target atoms. An illustration of this setup is portrayed in Figure 3.5. The surrounding ensemble (2) is held at a constant pressure and temperature (`npt` ensemble with 1 bar and 300 K), allowing heat and pressure to be dissipated smoothly. In order to avoid atoms crossing periodic boundary conditions, a third ensemble is placed around the dissipative ensemble (2). In the *ghost* ensemble (3), atoms are not allowed to move but may interact with the dissipative ensemble (2) through the pair-wise potential. It must be noted that this procedure still requires the target domain to be sufficiently large, considering that slight amounts of kinetic energy are lost at the interface between the target ensemble (1) and dissipative ensemble (2), if $E_k^{(1)} > E_k^{(2)}$.

Potentials

The main factors governing the selection of potentials were the reproducibility of thermal and mechanical properties of the materials. For Ti the MEAM potential published by Hennig *et al.* [125] was employed, which was developed with the focus on pressure-temperature phase transitions of titanium, ideally suited for application in the present study. In order to verify the potential, a numerical study of a $20 \times 20 \times 20 a_0$ Ti sample was performed (a_0 denotes the lattice constant). The temperature was set at 2400 K comparing the pair correlation function $g(r)$ with experimental data obtained by Wang, Yang, *et al.* [124]. The filtered, linearized verification results are shown in Figure 3.6, indicating excellent agreement with the

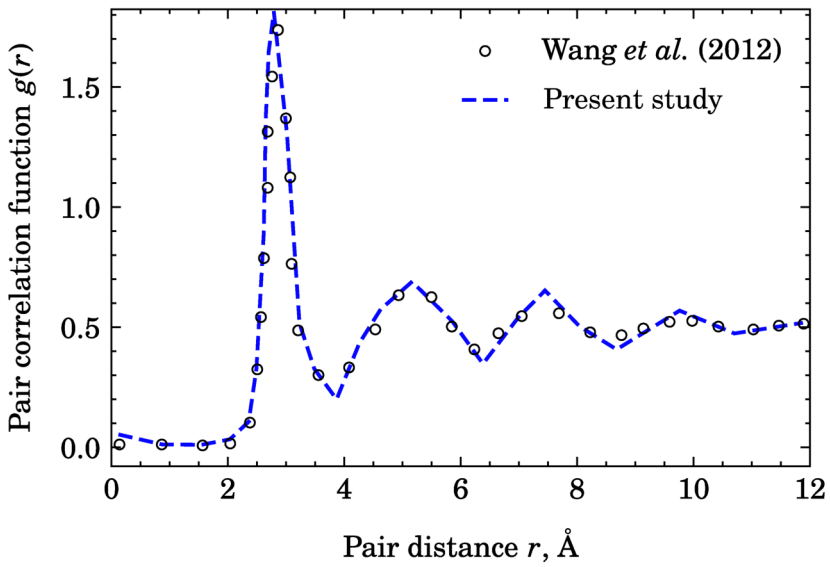


Figure 3.6 Comparison of pair correlation function by Wang, Yang, *et al.* [124] and numerical verification study of Ti at 2400 K.

experimental data. The graphite simulations were carried out using the LCBOP potential while both the SiO_2 and SiC simulations were performed using Vashishta-type potentials, which are already provided within LAMMPS.

Table 3.2 Types of hybrid, overlayed potentials used for species-wise interactions

Interaction	Potential	Notes
Ti – Ti	MEAM	Based on Hennig *et al.* [125]
Xe – Ti	ZBL	Based on Biersack and Ziegler [75], $Z_1 = 54$, $Z_2 = 22$, $r_i = 0.5$, $r_o = 1.0$
C – C	LCBOP	Based on Los and Fasolino [113]
Xe – C	ZBL	Based on Biersack and Ziegler [75], $Z_1 = 54$, $Z_2 = 14$, $r_i = 0.5$, $r_o = 1.0$
SiC – SiC	Vashishta-type	Based on Vashishta, Kalia, Nakano, *et al.* [117]
Xe – Si	ZBL	Based on Biersack and Ziegler [75], $Z_1 = 54$, $Z_2 = 14$, $r_i = 0.5$, $r_o = 1.0$
Xe – C	ZBL	Based on Biersack and Ziegler [75], $Z_1 = 54$, $Z_2 = 6$, $r_i = 0.5$, $r_o = 1.0$
SiO_2 – SiO_2	Vashishta-type	Based on Vashishta, Kalia, Rino, *et al.* [114]
Xe – Si	ZBL	Based on Biersack and Ziegler [75], $Z_1 = 54$, $Z_2 = 12$, $r_i = 0.5$, $r_o = 1.0$

Interaction	Potential	Notes
Xe – O	ZBL	Based on Biersack and Ziegler [75], $Z_1 = 54$, $Z_2 = 8$, $r_i = 0.5$, $r_o = 1.0$

Since nuclear stopping is governed by Coulombic-type interactions during the collision cascade (see sec. 2.3), the ZBL potential described by Eq. (2.6) is employed for modeling the interaction between the impacting Xe^+ ion and the target atoms. LAMMPS allows the use of multiple potentials using the `hybrid` command. The ZBL potential was used to describe Coulomb type interactions between the impact ion and the target atoms, while the potential validated and employed in the equilibriation simulation was used for interactions between the target atoms. A summary of the interaction models is given in Table 3.2.

Electronic properties

A difficult part of this thesis proved to be the acquisition of electronic properties for graphite, quartz, and silicon carbide. These materials have not attracted ultrafast laser ablation or warm dense matter (WDM) research, which are the driving force of determining these properties and lay the foundations for similar work.

For graphene, some data could be found in the literature and its thermal properties may be conveyed to graphite as demonstrated by Hone [126], since the prevailing temperatures are above 100 K. In an experiment carried out by White *et al.* [127], laser-accelerated protons were focused on graphite to heat it close to the melting point. X-ray diffraction (XRD) was employed in order to obtain a (constant) electron-phonon parameter g_p using relative Bragg scattering intensities. They obtained a range of $5.4 \times 10^{15} - 6.6 \times 10^{15}\,\mathrm{W\,m^{-3}\,K^{-1}}$ with an estimated 5 % error range of scattering measurements. Thus, a constant g_p of $6 \times 10^{15}\,\mathrm{W\,m^{-3}\,K^{-1}}$ was used for the TTM-MD simulations of graphite, since no electron temperature dependent data was available at the time of writing.

In a recently carried out study by Xibraku *et al.* [128], a temperature dependent heat capacity at constant volume was derived using DFT. They aimed at developing a new interatomic potential for carbon that includes effects of variable T_e. A plot of of their results for $C_e^{\mathrm{C}}(T_e)$ is given in Figure 3.7. The data was fit to the required LAMMPS input polynomial expression [120] of the form

$$C_e\left(T_e\right) = C_0 + \left(a_0 + a_1 T_e + a_2 T_e^2 + a_3 T_e^3 + a_4 T_e^4\right) \cdot e^{-(bT_e)^2}. \tag{3.23}$$

For Ti, the electron temperature dependent coupling parameter and heat capacity obtained from the simulations of Lin *et al.* [89] were used, which are outlined

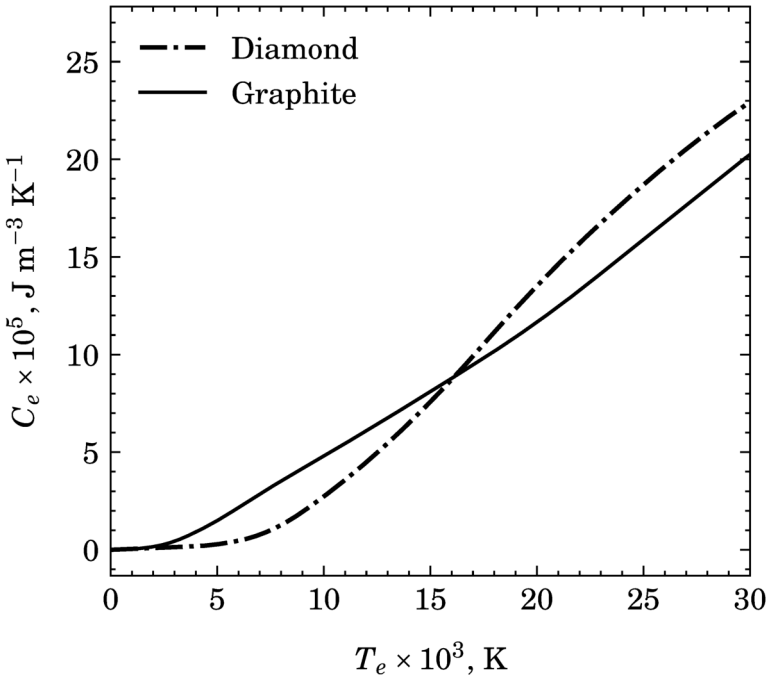


Figure 3.7 Electronic specific heat of graphite and diamond predicted by DFT simulations from Xibraku *et al.* [128]. They provided their values in meV/K/atom, which were converted to SI units using an atomic volume of $V^{\text{Carbon}} = 4/3\pi(150\,\text{Å})^3 = 1.41 \times 10^{-29}\,\text{m}^3$.

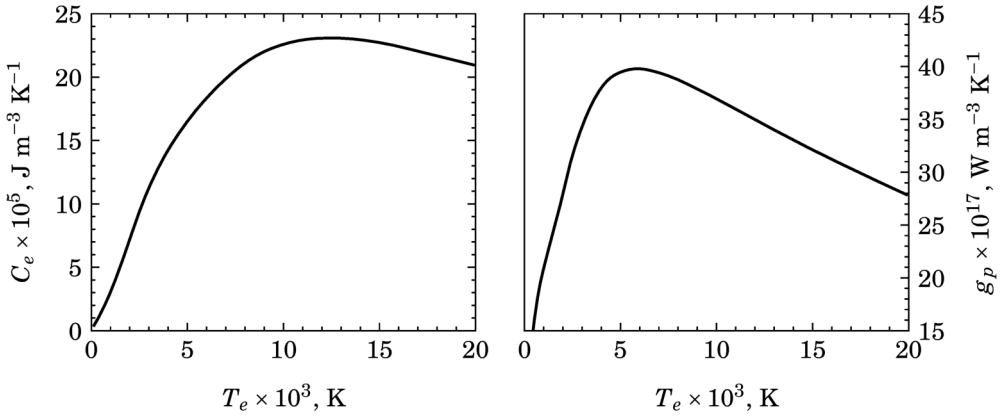


Figure 3.8 Temperature dependent electronic properties of Ti based on DOS simulation from Lin *et al.* [89]. **Left**: Specific heat capacity **Right**: Electron-phonon coupling parameter.

in Figure 3.8. The same polynomial expression given in Eq. (3.23) was used to fit the DFT data to the LAMMPS input polynomials.

In the publication by Ravichandran *et al.* [129], where ultrafast melting through ion irradiation of W−SiC semiconductors was investigated; they used a specific heat capacity for SiC of $2.5 \times 10^5\,\text{J m}^{-3}\,\text{K}^{-1}$ previously adopted by Zhang *et al.* [130] and an electron-phonon coupling parameter of $g_p^{\text{SiC}} = 9.8 \times 10^{18}\,\text{W m}^{-3}\,\text{K}^{-1}$. The

data for $\alpha-SiO_2$ was taken from Phillips *et al.* [53]. They employed the TTM model to simulate radiation damage evoked by laser heating or high-energy cascades and their temperature dependent heat capacity of SiO_2 is shown in Figure 3.9. Leino *et al.* [131] assumed that the TTM-specific coupling parameter γ_p given in Eq. (3.7) can also be derived from the ratio of the (mean) molar mass to the electronic relaxation time

$$\gamma_p = \frac{m_i}{\tau}, \quad m_i = \frac{28.04\,\mathrm{u} + 2 \cdot 16.00\,\mathrm{u}}{3} = 38.706\,\mathrm{u}. \tag{3.24}$$

They estimated $\tau \approx 150\,\mathrm{fs}$, yielding $\gamma_p = 258\,\mathrm{eV/Kelectron}$ (LAMMPS units).

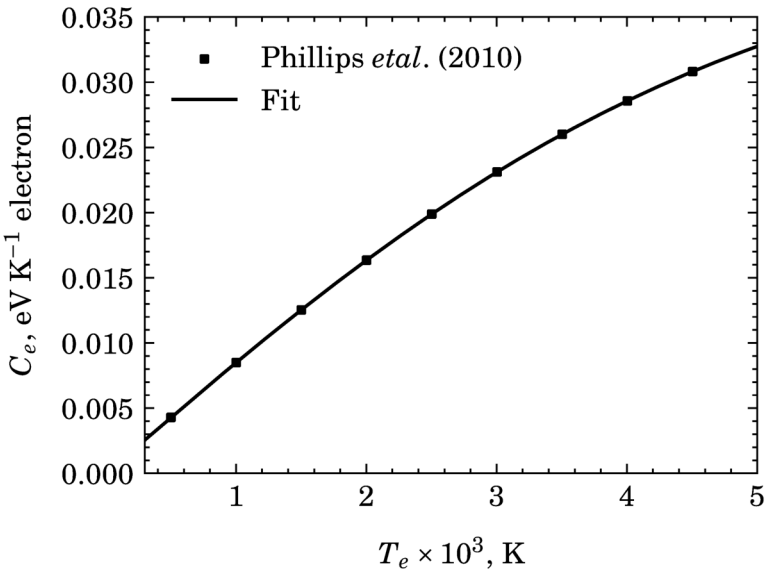


Figure 3.9 Temperature dependent heat capacity of SiO_2 in LAMMPS units; scatter plot represents data from [53], continuous line is the fit according to Eq. (3.23).

The input parameter governing diffusion of heat through the electronic subsystem is the electronic thermal diffusivity, which is defined in the `fix ttm/mod` command of LAMMPS as [120]

$$D_e(C_e) = \frac{\kappa_e}{\rho_e C_e}, \tag{3.25}$$

and depends on the electronic heat capacity, electronic density, and electronic thermal conductivity. κ_e governs how fast electrons are able to conduct heat throughout the electronic subsystem and has numerical implications, since a higher thermal conductivity results in a smaller time step to ensure that the CFL criterion is adhered to. The `fix ttm/mod` package automatically adjusts the time step for

robustly advancing Eq. (2.1) in time based on the local specific heat, because ρ_e and κ_e are assumed constant. An overview of the values utilized for κ_e for each investigated material is given in Table 3.3.

Table 3.3 Overview of material-wise employed values for κ_e

Material	**Value**, $\mathrm{W\,m^{-1}\,K^{-1}}$	**Reference**	**Notes**
Ti	22	[132]	Data used to simulate femtosecond laser ablation.
C	101	[133]	DFT derived data.
SiO_2	0.011	[53, 131]	SiO_2 acts as an (electronic) insulator.
SiC	0	[129]	SiC is a semiconductor, hence $\kappa_e = 0$.

The final parameters required for the TTM-MD simulations are related to electronic stopping. It was shown by Lindhard and Scharff [134], that at energies below several tens of keV, electronic stopping is proportional to the impacting ion energy:

$$\frac{\delta E_{\mathrm{el}}}{\delta x} = \xi \sqrt{E_i}\,. \tag{3.26}$$

In Eq. (3.26), ξ indicates the *constant of proportionality*, from which the electronic stopping parameter γ_s (see Eq. (3.6)) may be determined as [86]

$$\gamma_s = \xi \sqrt{\frac{1}{2} m_i}\,. \tag{3.27}$$

ξ can be calculated from the software SRIM [68], a Monte-Carlo based collection of codes that are capable of calculating various important quantities when (fast) ions penetrate matter and for each impacting energy, ξ must be computed with SRIM.

Next, a threshold energy for atoms inside active voxels must be defined that governs if electronic stopping is active or not. Duffy and Rutherford [86] recommended $2 \times E_c$ (see sec. 3.2), which gives a value of $6300\,\mathrm{m\,s^{-1}}$ for Ti. Any atoms moving faster than this velocity will experience friction with the electronic subsystem and lose kinetic energy, while T_e increases in the respective voxel.

3.4.3 Deriving macroscopic and structural properties

Analyzing individual atoms can only give data afflicted with high statistical noise due to the nature of atomic scale physics. In order to draw a comprehensive picture of the macrophysics, it is necessary to define quantities that are capable of reproducibility.

The most prominent macroscopic quantity is the temperature of the ensemble, which LAMMPS [135] determines from

$$T = \frac{2E_k}{N_{\mathrm{DOF}} \cdot k_B}, \quad \text{with} \quad E_k = \sum_{i=1}^{N_{\mathrm{atoms}}} \frac{1}{2} m_i u_i^2 \quad \text{and} \quad N_{\mathrm{DOF}} = 3N_{\mathrm{atoms}} - 3\,. \tag{3.28}$$

In Eq. (3.28), N_{DOF} indicates the total number of degrees of freedom of the atoms. This computation may be performed for the MD supercell, i.e., all the atoms, or can be done using a background grid similar to the TTM grid, where only atoms within a cell contribute to the cell-wise properties. This allows a spatial resolution of the temperature *within* the MD supercell with the only requirement to have sufficient number of atoms in each cell to minimize statistical noise.



Figure 3.10 Template matching hulls for different lattice structures. From: Larsen *et al.* [136].

An important characteristic majorly influencing the mechanical and thermal properties of metals and graphite is the crystallic structure of the atoms. Larsen *et al.* [136] published a landmark paper that allows a computationally efficient identification of crystalline structures in MD simulations. Their idea was to employ common neighbor analysis to individual atoms and match the neighboring arrangement to polyhedral templates based on a cut-off, illustrated in Figure 3.10. The original algorithm is natively included in LAMMPS using the `compute/ptm` package.

3.4.4 Obtaining initial atomic configurations

A key problem in MD are initial atomic configurations. When initializing an atomic ensemble using a certain lattice spacing, one has to apply a specific kinetic energy to individual atoms corresponding to a distribution function of the macroscopic temperature. Usually, a Maxwell–Boltzmann velocity distribution $f(u)$ is considered, which can be expressed as

$$f(u) = 4\pi \cdot \left(\frac{m_i}{2\pi k_B T}\right)^{\frac{3}{2}} u^2 \cdot e^{-\frac{mu^2}{2k_B T}}\,. \tag{3.29}$$

However, the probability that this initial distribution of kinetic energy and placement of individual atoms is in a low-energy state is highly unlikely, making it necessary to minimize the energy of the ensemble. Furthermore, when simulating larger ensembles with hundreds of thousands atoms, polycrystalline structures become relevant, since real experimental probes are rarely of monocrystalline form. The circumstances described in this section have lead to a tailored process for obtaining realistic initial atomic configurations.

In a first step, the entire box of atoms was initialized in space based on the lattice parameter a_0 and the type of lattice (for instance `fcc` or `hcp`). If the material features polycrystalline characteristics such as Ti, the system was initialized using the `atomsk` software [137]; see Figure 3.11 for an example.

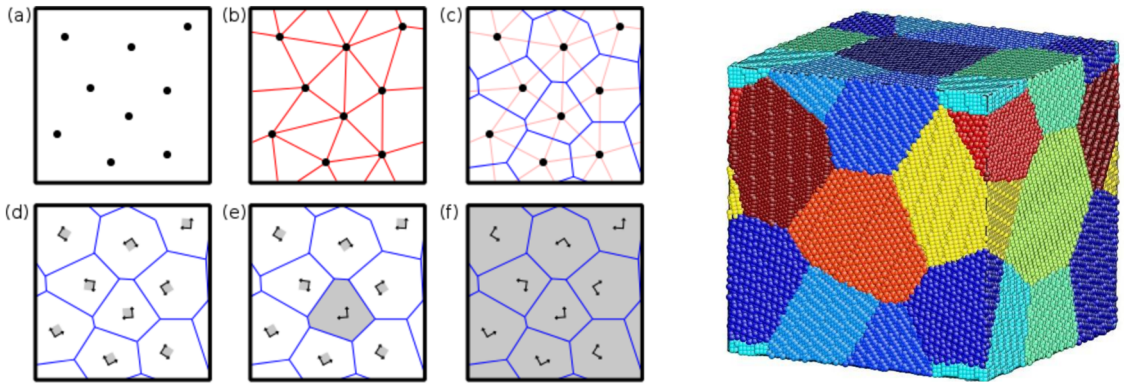


Figure 3.11 Example of polycrystalline initialization using Voronoi tessellation [138] in the `atomsk` code.

Then, the system's energy is minimized at 0 K using the LAMMPS feature `minimize` utilizing certain thresholds after which the process is considered converged. taking typically several thousands of iterations. Thereafter, all atoms were given a kinetic energy based on the macroscopic temperature of 1 K. Subsequently, atoms are slowly heated to $1.5{\times}T_{\mathrm{melt}}$ for a timespan of 1 ns using the `npt` ensemble. The pressure was held constant at 1×10^{-4} Pa, representing the ambient pressure during testing in a vacuum facility or space-like environment. After the ensemble has liquified or sublimated and reached the target temperature, it was held at the same temperature and pressure for another 1 ns (`npt` ensemble). Thereafter, the ensemble was cooled down to the thruster's accel grid temperature of 350 K for 5 ns and finally allowed to relax at this temperature and vacuum facility pressure for another 5 ns (`npt` ensemble). From here, the initial atomic configuration was ready and the individual groups of atoms specified (target, dissipative, and ghost) before the impact process was initiated.

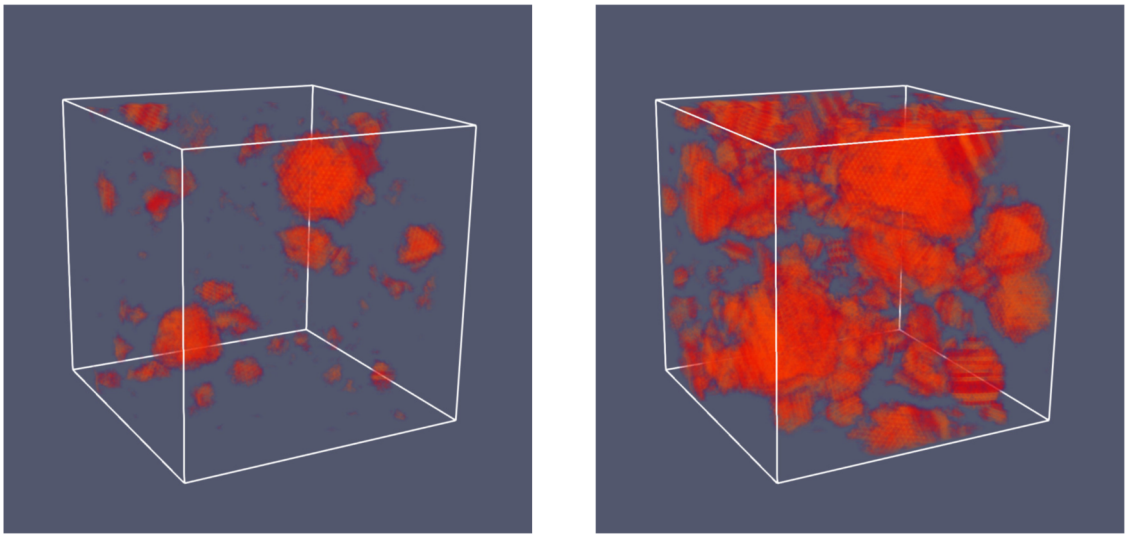


Figure 3.12 SiC supercell during quenching period and equilibriation, colored by PTM identified lattice structures (dcub and dhex) using a continuous volume rendering technique. The left image shows the initial growth of diamond like crystal nuclei from the slowly cooled liquid. The right image illustrates the formation of groups from crystalline nuclei at a later stage during quenching.

A volume rendering of the crystal growth of diamond cubic (dcub) and diamond hexagonal (dhex) crystals (calculated by the PTM method) during the quenching process of SiC is shown in Figure 3.12. It illustrates how small nuclei of dcub and dhex grow into larger groups, eventually forming a random crystalline structure throughout the supercell.

The final supercell of SiC is depicted in Figure 3.13, displaying the formation of mostly diamond cubic and diamond hexagonal lattice structures, with a small portion of intercrystalline atoms, corresponding well to the polymorphic nature of silicon carbide [139]. The figure was obtained by employing bond analysis (available in OVITO [140]) and demonstrates how silicon and carbon atoms form bonds with one another.

A similar figure is presented in Figure 3.14, which depicts the equilibrium silica supercell. On the left side, the non-uniform surface topology is recongnizable while on the right side the positioning of SiO_2 molecules in close proximity to the surface is evident with more blue silicon atoms extending outwards due to their lower capability to attract bulk atoms.

In Figure 3.15, the MD supercell after melting, quenching, and equilibriation is shown for the Ti case. The cooling rate of $10\,\mathrm{K\,ps^{-1}}$ resulted in 85 % of α–Ti, 10 % of crystallic boundary atoms (not in any crystallic structure), and 4 % of β–Ti with small amounts of fcc atoms ($< 1\,\%$) present, corresponding to observations of phase transitions and co-existence of hcp and bcc phases in stable Ti [141].

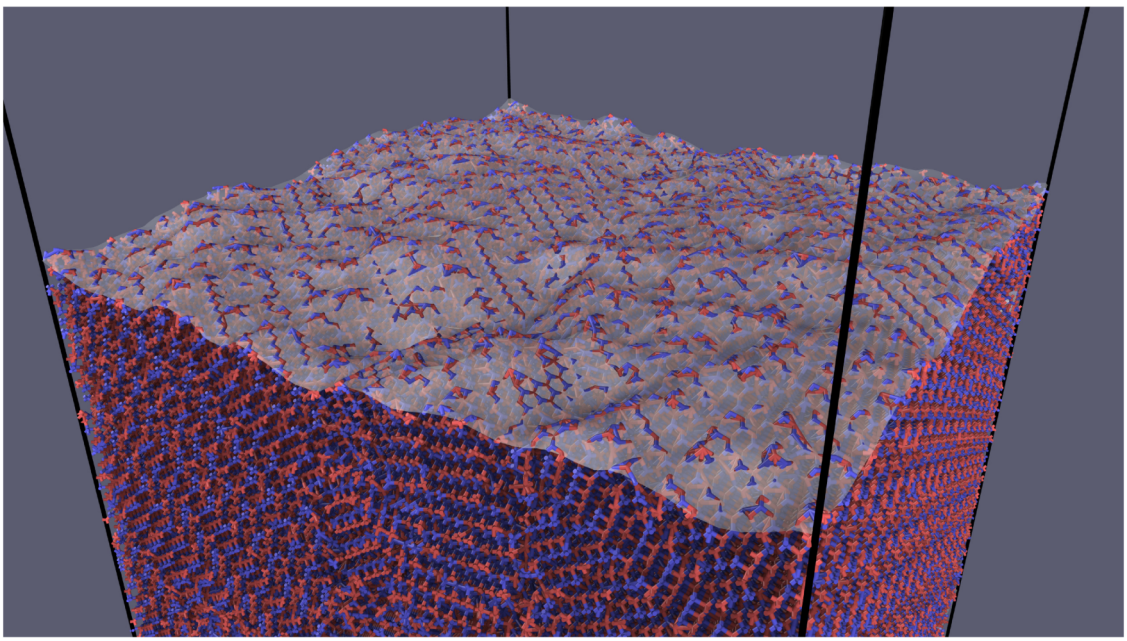


Figure 3.13 SiC supercell after equilibriation, melting, and quenching; portrayed as atomic bonds, colored by atom type (**blue**: Si, **red**: C). A surface-mesh of the supercell was generated to outline the formation of non-uniform topology during quenching. Crystalline boundary: 19 %, diamond cubic dcub atoms: 60 %, diamond hexagonal dhex atoms: 21 %.

Since the mechanical properties of graphite and quartz vary greatly with the lattice orientation relative to the load, a randomized rotation is applied around each axis and the global origin coordinate system:

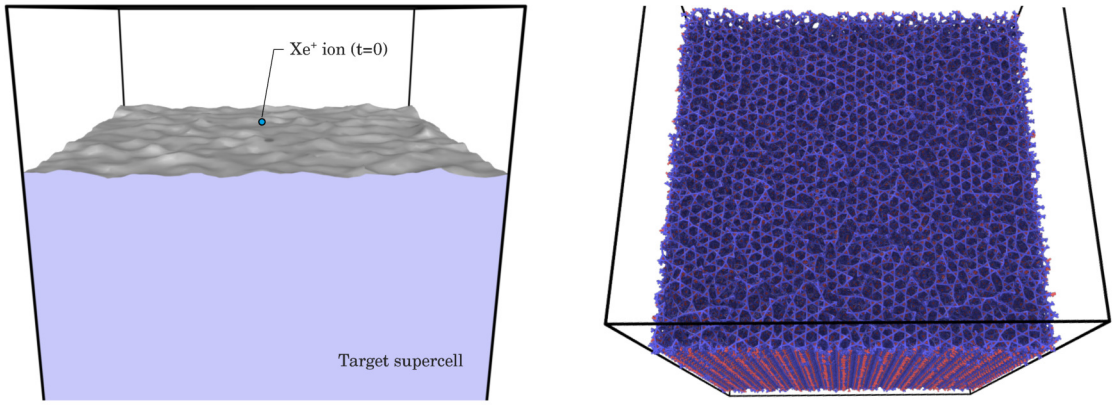
$$\theta_1 \in \{0, \dots, 360\}\,\text{deg} \quad \theta_2 \in \{0, \dots, 360\}\,\text{deg} \quad \theta_3 \in \{0, \dots, 360\}\,\text{deg}\,. \tag{3.30}$$

Thereafter, the simulation box is adjusted accordingly to ensure correct dimensions of the atomic supercell before the impact simulation commences.

The total number of atoms in the MD simulation box was $\approx 350\,000$ atoms.

3.4.5 Impact simulations

A Python script was devised that reads in a `meta.yml` file which contains the minimum and maximum values for the impact energy and angles, respectively. For each target material, a folder is then created based on a unique combination of those parameters, and the input files adjusted accordingly. Since the trajectory of ions traversing through the bulk material depends in particular on the impact angle – and to furthermore avoid channeling effects – a *randomized* $x-$ and $y-$component of the impacting ion's initial position was enforced for each of the 5 simulations that



Generated surface mesh Top view of bonds

Figure 3.14 SiO_2 supercell after equilibriation, melting, and quenching. Left: generated surface mesh of final configuration before irradiation with Xe^+ ion at $t = 0$. Right: portrayal of atomic bonds, colored by atom type (**blue**: Si, **red**: O), showcasing amorphous topology and bulk structure.

were carried out for each parameter combination. An example of how the resulting case folder structure looks like for the $E = 1000\,\text{eV}$ impact energy parameter is given in the code block below (Listing 3.1):

Listing 3.1 Example of folder structure for a 1000 eV impact case

```
- E_1000eV
    - beta_0deg
        - rcase0
        - rcase1
        - rcase2
        - rcase3
        - rcase4
    - beta_30deg
        - rcase0
        - rcase1
        - rcase2
        - rcase3
        - rcase4
    - beta_50deg
        - rcase0
        - rcase1
        - rcase2
        - rcase3
        - rcase4
    - beta_70deg
```

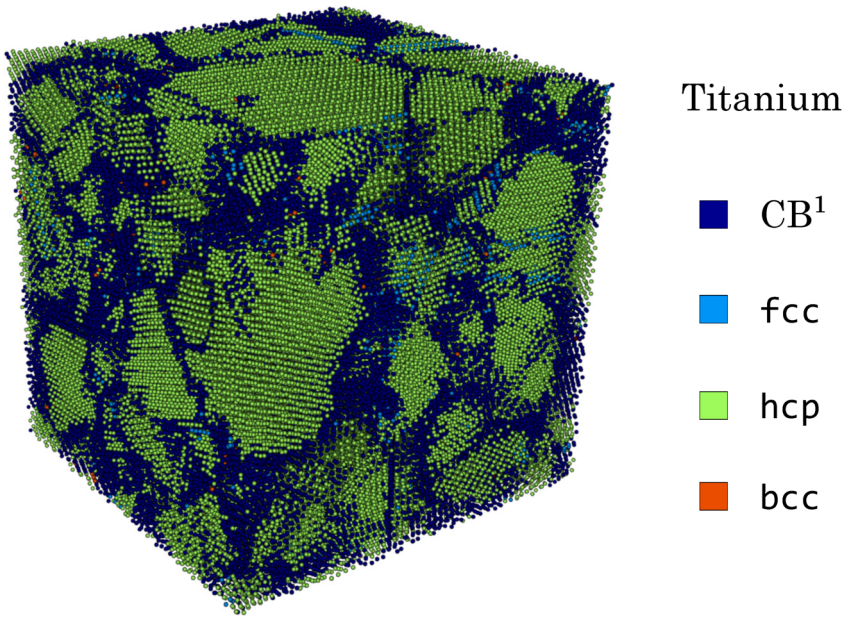


Figure 3.15 Ti supercell after melting, quenching, and equilibriation, colored by PTM identified lattice structures. [1]Crystalline boundary atoms: 10 %, face-centred-cubic fcc atoms: 1 %, hexagonal close packed hcp atoms: 85 %, body centred cubic bcc atoms: 4 %.

```
21          - rcase0
22          - rcase1
23          - rcase2
24          - rcase3
25          - rcase4
```

A Simple Linux Utility for Resource Management (SLURM) job is then submitted for each case and LAMMPS run on up to 16 nodes. The first step in the `in.ttm` file (for input file parameters see in the appendix, Chap. A) is to read in the equilibriated supercell and generate the atom groups according to Figure 3.5. Next, the electron background voxels are initiated based on the extensions of the domain and desired grid volume. From the equilibrium temperature of 350 K, the temperature dependent electronic properties are calculated, while the custom algorithm checks for voxels that are occupied with a threshold of more than a certain number of electrons ($N_i > 20$ for the voxel to be activated, i.e., $T_e \neq 0$). Then, the individual ensembles are enforced using the `nve` ensemble to advance the TTM group in time and the `nvt` ensemble for the penultimate atom group with a very strict temperature dampening parameter in order to quickly allow the ensemble to dissipate incoming pressure and temperature waves.

After the target material groups and numerical settings are established, the impacting Xe^+ ion is placed based on a random uniform distribution 2 Å above the

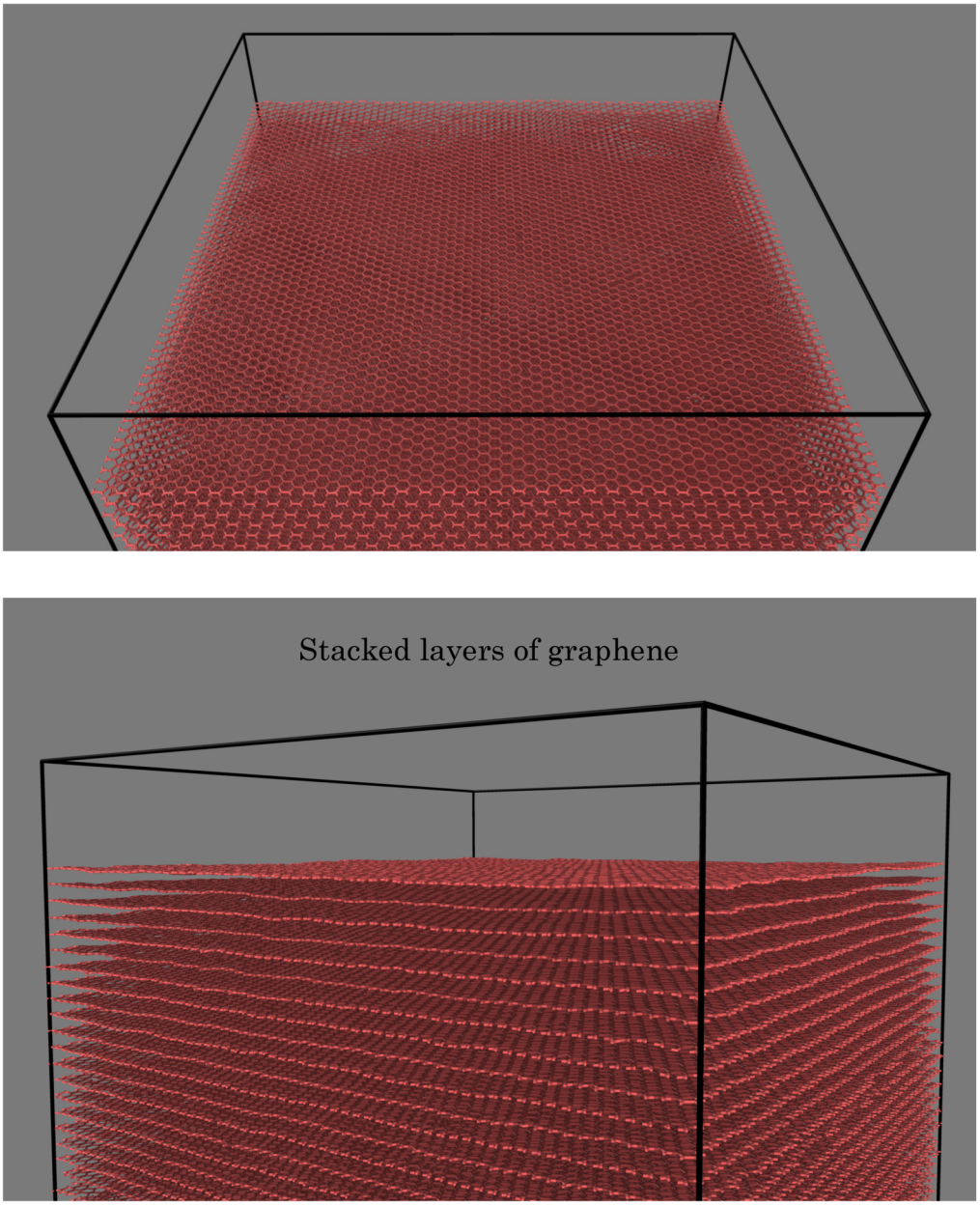


Figure 3.16 Graphite supercell after equilibriation, illustrating stacked layers of graphene and array of hexagonal carbon rings building graphite.

target in the $xy-$plane, where also u_x and u_y are randomly varied to minimize the effects of numerical channeling[9]. The impacting ion is solved using the nve ensemble and a global time step of 0.2 fs is set to advance the solution in time, ensuring that the maximum distance an atom travels per time step is

$$\Delta x_{\max} = u_{\max} \cdot \Delta t = 50\,000\,\mathrm{m\,s^{-1}} \cdot 0.2 \times 10^{-15}\,\mathrm{s} = 0.1\,\text{Å}\,. \tag{3.31}$$

[9]Still, an exact impact angle is ensured using the relation $|u| = \sqrt{u_x^2 + u_y^2 + u_z^2}$ with $|u|$, u_z, and β as the boundary conditions.

The solution output deliveres the following quantities every 25 time steps, i.e., 5 fs:

- Xe^+ atom spatial coordinates and velocity
- TTM target atoms spatial coordinates, velocity, and PTM type (see Figure 3.10)
- Electron voxel temperature
- Background grid temperature and velocity

The total simulation time is 3 ps = 10 000 timesteps, enough time for the impacting ion to traverse through the target and come to rest. During this time, the collision cascade should produce fast secondary, tertiary, etc. atoms through momentum exchange. The upper $z-$boundary of the simulation domain is located in a way that during the solution time, the escaping atoms from the bulk material have enough time to reach this boundary plane. They are then trapped and considered *sputtered atoms*, sufficiently far away to not interact through the potential with the target atoms anymore. Since multiple simulations are carried out for one angle-energy combination, an average yield may then be calculated for each combination based on the mean number of trapped atoms.

The simulated bulk sample is approximately 10 nm wide in each spatial direction (see Figure 3.5). To give an example of the transport of information through the target, we consider a Ti case. The time a pressure or temperature wave requires to reach the penultimate `nvt` ensemble is

$$t = \frac{\Delta x}{a_{\mathrm{Ti}}} = \frac{0.5 \cdot 100 \times 10^{-9}\,\mathrm{m}}{6100\,\mathrm{m\,s^{-1}}} \approx 8.2\,\mathrm{ps}\,, \tag{3.32}$$

where a is the material specific speed of sound [142]. The simulation time of 2 ps is well below the time of the pressure wave reaching the penultimate `nvt` ensemble but long enough for the thermal spike to reach its maximum. As a result, the region affected by the irradiation starts to relax and cool down after the thermal spike while the pressure waves continue to spread through the target.

3.5 Synopsis

This chapter presents an overview of the manner in which a connection is made between the theoretical descriptions outlined in Chap. 2 and the numerical models utilized in this thesis. Moreover, a comprehensive review is provided of the selection of models utilized in this thesis with respect to the electronic and atomic subsystems. The reader is introduced to the actual setup used for running the simulations including the software, customizations, and choice of temporal and spatial resolution.

Finally, the combination of the inherently different TTM (continuum PDE based) and MD (ab-initio discret) models is demonstrated, as well as the approach for analyzing the vast parameter space in realistic timeframes.

In order to capture both the electronic and nuclear stopping described by the TTM and MD models, respectively, the coupled TTM-MD method was applied. The TTM model serves as the approach capable of characterizing the electronic stopping of the impacting ion and fast target atoms affected by the *initial* collision cascade as well as the dissipation of thermal energy from excited electrons to the ions through the electron-phonon coupling parameter. On the other hand, the MD method serves as the model capturing the nuclear stopping and interatomic interactions by the collision cascade, especially after electronic stopping becomes negligible and the target is purely governed by thermal interactions and relaxation of the hot collision cascade zone. Conversely to most research data available in the literature, the full electronic and atomic interaction is simulated including the ion-target, target-target, and electronic subsystem interactions by using the TTM-MD technique and hybrid potentials. These potentials are realized by coupling together high-resolution potentials available for each respective material with the ZBL potential for close-range highly repulsive interactions which occur between the ion and PKA and subsequent fast primary and secondary atoms affected by the initial collision cascade.

Scepticism is as much the result of knowledge, as knowledge is of scepticism.

— Homer, The Iliad

4 Results and discussion

Contents

4.1 Titanium 58
4.1.1 Principal analysis 58
4.1.2 Parameter study 70
4.2 Graphite 74
4.2.1 Principal analysis 74
4.2.2 Parameter study 78
4.3 Quartz 83
4.3.1 Principal analysis 83
4.3.2 Parameter study 86
4.4 Silicon carbide 90
4.4.1 Principal analysis 90
4.4.2 Parameter study 93
4.5 Synopsis 97

In this chapter, the postprocessed results of the simulations are presented and critically discussed. Furthermore, comparisons with experimental and other computationally derived data are made. For each material, principal analyses of the underlying physical processes of the collision cascade that were obtained from the TTM-MD simulations, are presented. In this section, atomic trajectories as well as continuum data (i.e., temperature) obtained from the background voxels are used to analyse the collision cascade temporally. The PTM method serves as a crucial tool to support the identification of local melting, phase transitions, and atoms being extracted from their local lattice structure. The principal analysis is carried out for the highest impact energy case at both normal $(\beta = 0\,\mathrm{deg})$ and maximum incidence

$(\beta = 70\,\text{deg})$. It is demonstrated that despite the highly statistical nature of ab-initio MD simulations, the application of an appropriate potential, knowledge of electronic properties and a well-defined initial configuration (in particular for crystal dominated atomic structures), it is possible to gain a fundamental understanding of the evolution of the collision cascade, the electronic temperature, the lattice temperature, and bulk structure affected by the impact through the PTM algorithm.

In the subsequent parameter study section the present analyses are connected to real-world applications through predictions of numerical values of significant engineering quantities. These are the ion penetration depth and the sputter yield, which can be compared to other methods such as SRIM-2013 and experimental data available in the literature. In order to establish well defined results for the sputtering yield the average number of bulk atoms escaping the upper MD boundary were determined, based on the performed runs for a single case. In these sections dedicated to parameter studies, all impact energies and angles are taken into account.

4.1 Titanium

4.1.1 Principal analysis

The first analyzed case in this section was that of maximum energy and normal incidence, corresponding to $E = 1400\,\text{eV}$ and $\beta = 0\,\text{deg}$. In Figure 4.1, results of time-dependent ion velocity and penetration depth are illustrated for the five cases with randomized impact positions. Note that in the lower plot, the ion launch location is 2 Å above the target, while the grey area delineates the bulk atom region. Clearly, the importance of carrying out multiple runs with randomized initial ion locations is underlined, since a clear outlier is visible where the artificial channeling effect occurred (run 1). The other runs exhibited trends similar to one another, with the majority of inelastic momentum exchange collisions occurring during the initial 0.25 ps and their respective penetration depth values close to the final one. Unique high energy collision events manifest themselves as a huge decrease in velocity, for example run 3 (orange line) at 0.05 ps, run 4 (red line) at 0.15 ps and run 1 (blue line) at 0.3 ps. Taking the mean of all cases, indicated by the black dashed line, reveals a quasi exponential decay of both the ion velocity and penetration depth. In all cases, the ion comes to rest after about 0.6 ps at an average penetration depth of 48 Å with slight changes to the implanted location afterwards due to Ti atoms that were thermally excited through the collision cascade interacting with the ion.

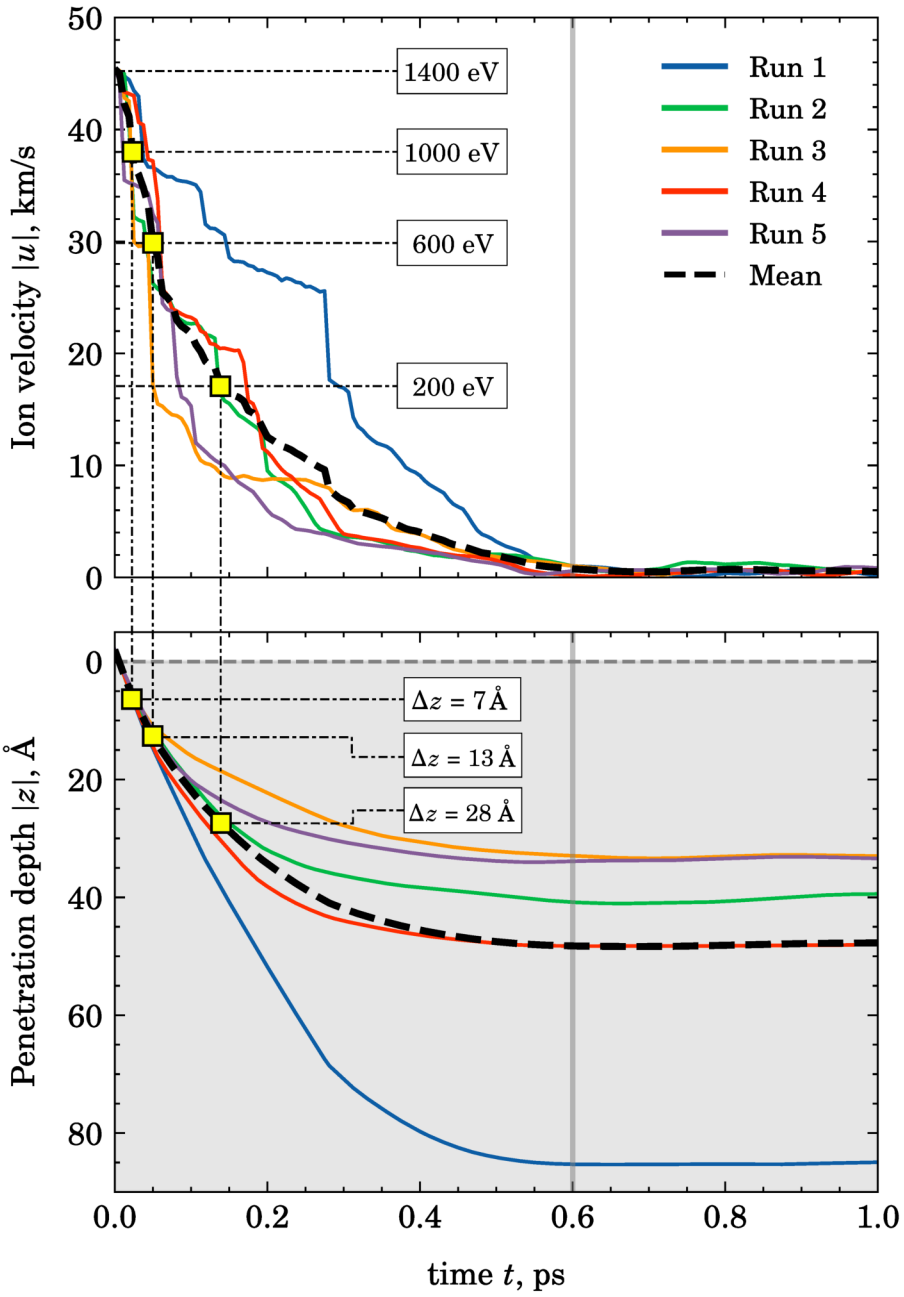


Figure 4.1 **Case:** $E_{\mathrm{Xe+}} = 1.4\,\mathrm{keV}$, $\beta = 0\,\mathrm{deg}$. Top: Time-dependent ion velocity of the five different runs with mean indicated by dashed black line. Bottom: Time-dependent total penetration depth $|z|$. The time when the ion comes to rest in all cases is indicated by the vertical gray line.

A closeup of the MD supercell after 2 ps is illustrated in Figure 4.2. In this figure, the Ti atoms are colored by their PTM calculated cystalline structure and the ion trajectory throughout the simulation denoted by the colored streamline. It is observed that the initially normal trajectory of the ion is significantly altered after the first few collision events. Besides, it can be seen that the coloring of the velocity changes rapidly with each of the first collisions, while decreasing much more

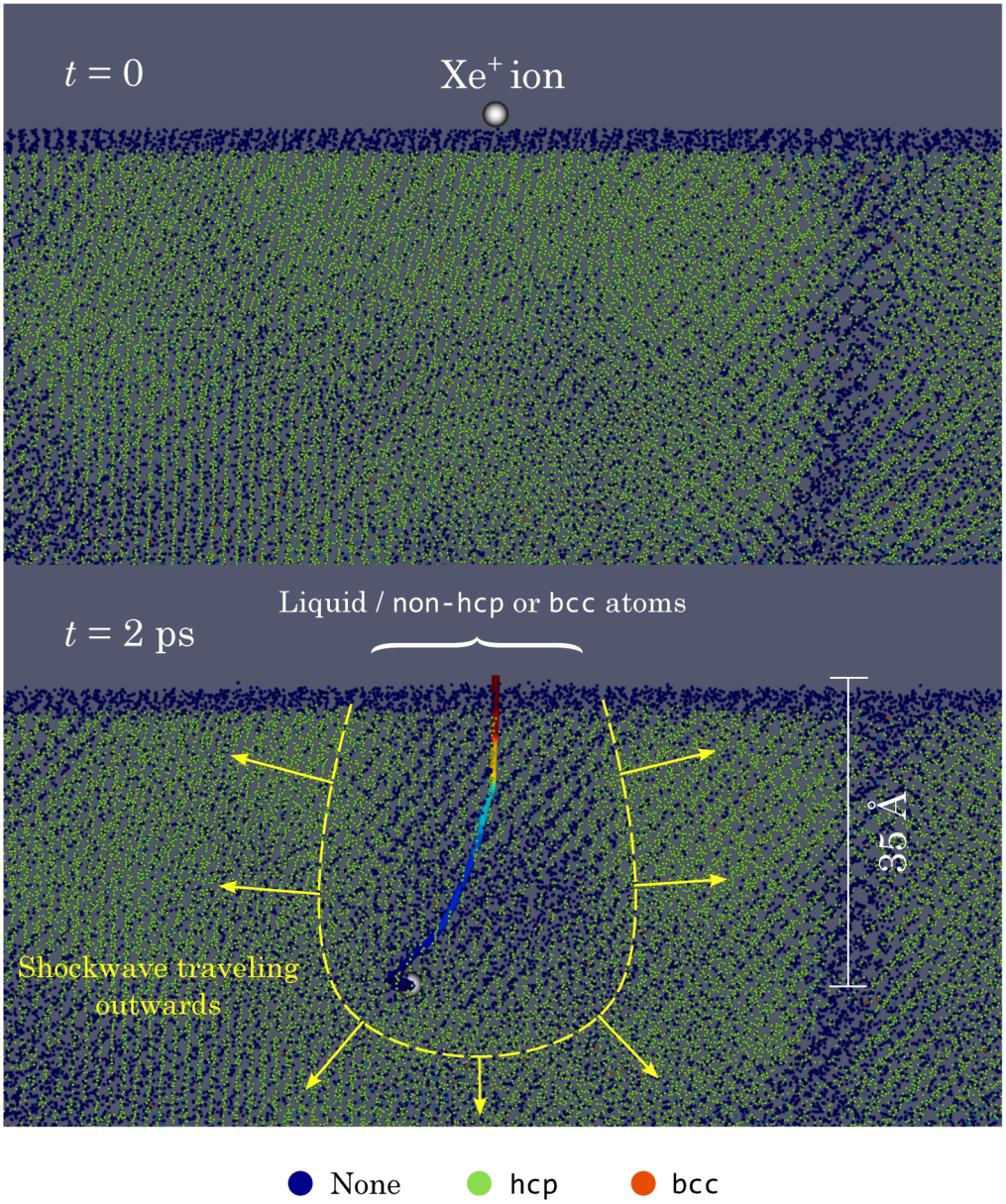


Figure 4.2 **Case:** $E_{\mathrm{Xe+}} = 1.4\,\mathrm{keV}$, $\beta = 0\,\mathrm{deg}$, run 3. Region affected by ion irradiation after 2 ps. The collision cascade produces fast atoms escaping their lattice structure (indicated in blue as *None*), generating a region of liquid titanium, which relaxes after the ion and cascade have come to rest. In this simulation, 1 titanium atom left the bulk material and crossed the upper boundary condition ($Y = 1$) while the region marked in yellow featured a temperature of roughly 1200 K, slowly relaxing towards the initial temperature. Ion velocity colored from red: ≡ 50 km/s to blue: ≡ 0 km/s.

smoothly when the ion has lost most of its kinetic energy due to collisions taking place in a more elastic manner. The collision cascade results in the production of a liquid region, where most of Ti are neither of hcp or bcc type, indicated by their blue

color. Further, the exchange of momentum within the hot liquid leads to the upper surface moving slightly outwards. In order to gain further inside on the thermal spike, excitation and relaxation of the liquid zone, it is necessary to study the atomic and electronic temperature in this region. As described in detail in sec. 3.4.3, the background voxels for the electronic temperature were also used to calculate an average atomic temperature in each voxel, given that the number of atoms inside an individual voxel is higher than the predefined threshold of 20[1].

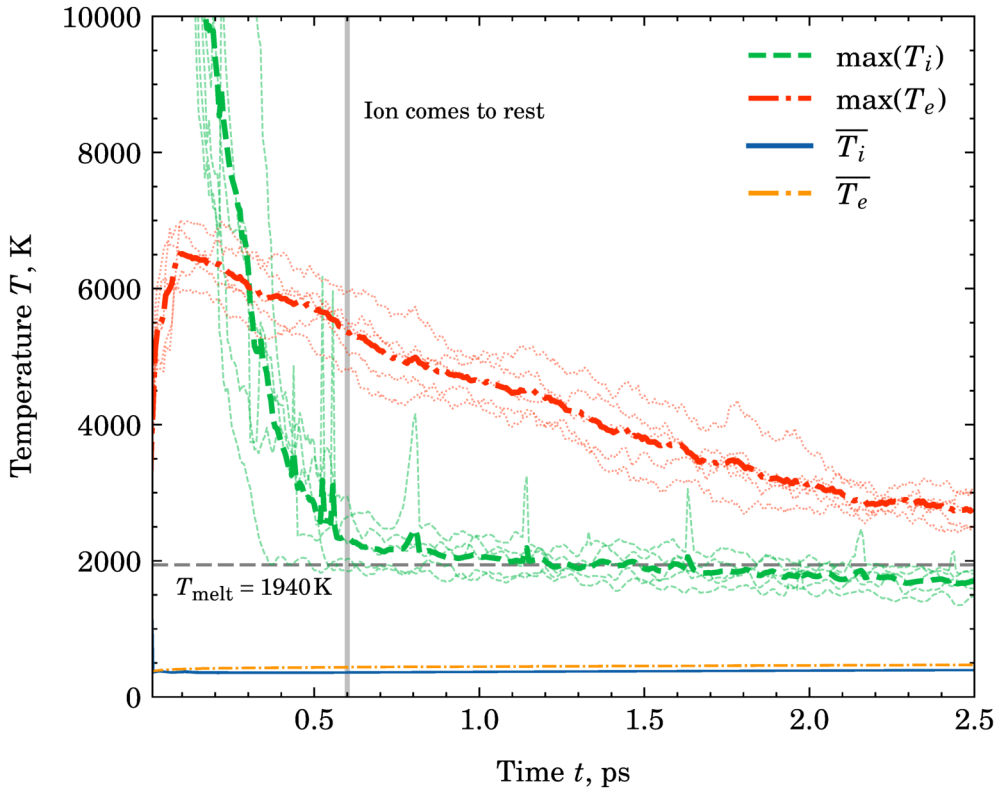


Figure 4.3 **Case:** $E_{\text{Xe+}} = 1.4\,\text{keV}$, $\beta = 0\,\text{deg}$. Temporal evolution of mean and max atomic and electronic temperature. The thick dashed lines respresent the averages of the five runs for each quantity; the melting temperature of Ti is indicated by the horizontal, gray dashed line; the time when the ion comes to rest according to Fig. 4.1 is given by the vertical gray line.

The temporal evolution of the voxel atomic and electronic temperatures is outlined in Figure 4.3. For each temperature the mean voxel temperature of the entire domain and maximum encountered individual voxel temperature is plotted. Within the first 250 fs after the PKA event, the temperature rises up to 50 000 K, although this value must be dealt with cautiously, since LAMMPS calculates the

[1] In the initial, equilibriated configuration at $t = 0$, each voxel contained about 30 atoms at a total number of 8000 voxels spanning the simulation domain.

temperature entirely based on the (translational) kinetic energy of the atoms inside a voxel. Since the first collision events result in *single* very fast secondary atoms that initially do not interact with their surroundings, one should not interpret this result as a temperature in a Maxwellian sense. After 250 fs, the first collision events have taken place and the cascade is initiated. At this point, the maximum voxel temperature is about 7000 K and the maximum number of voxels are located above the melting temperature, visible in Figure 4.3. Due to their mobility and friction with the fast ion, the maximum electronic temperature is reached already after about 100 fs. Thereafter, the ion velocity is not large enough to heat the electronic subsystem anymore and interactions are mainly dominated by nuclear stopping. From $t = 100$ fs onwards, the electronic subsystem starts to cool and disperse the locally high kinetic energy outwards into the bulk system through the electronic thermal conductivity while contributing to the heating of the lattice through the electron-coupling g_p. After 400 fs, the gradient of newly converted atoms that previously were in hcp or bcc lattice reaches its maximum as seen in Figure 4.4, which is also the time when the impacting ion has lost most of the kinetic energy. From there, the conversion rate remains constant for the next 2 ps, despite that at 1.5 ps, almost all voxels are below the melting temperature.

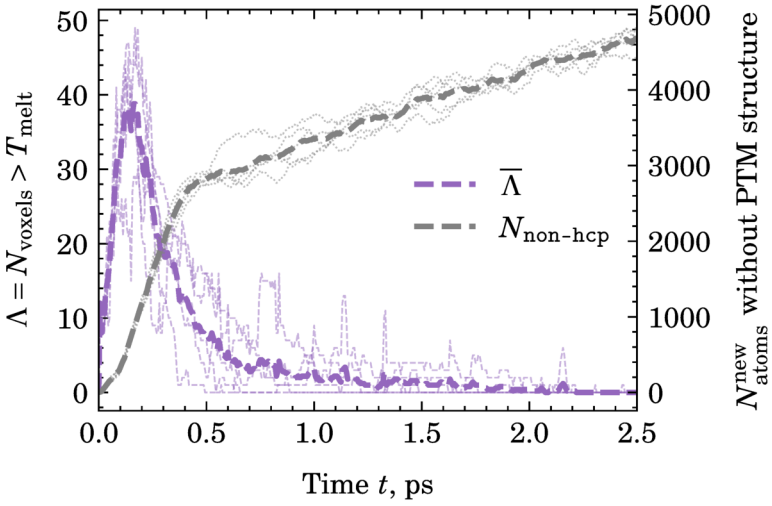


Figure 4.4 **Case:** $E_{\text{Xe+}} = 1.4$ keV, $\beta = 0$ deg. Temporal evolution of voxels with (atomic) temperatures above T_{melt} and number of atoms leaving the hcp or bcc structure compared to the initial number at $t = 0$ (see Fig. 3.15).

This indicates that the conversion of lattice solid to liquid atoms is not entirely temperature driven but also due to effects of the strong shockwave traveling outwards from the collision cascade affected zone.

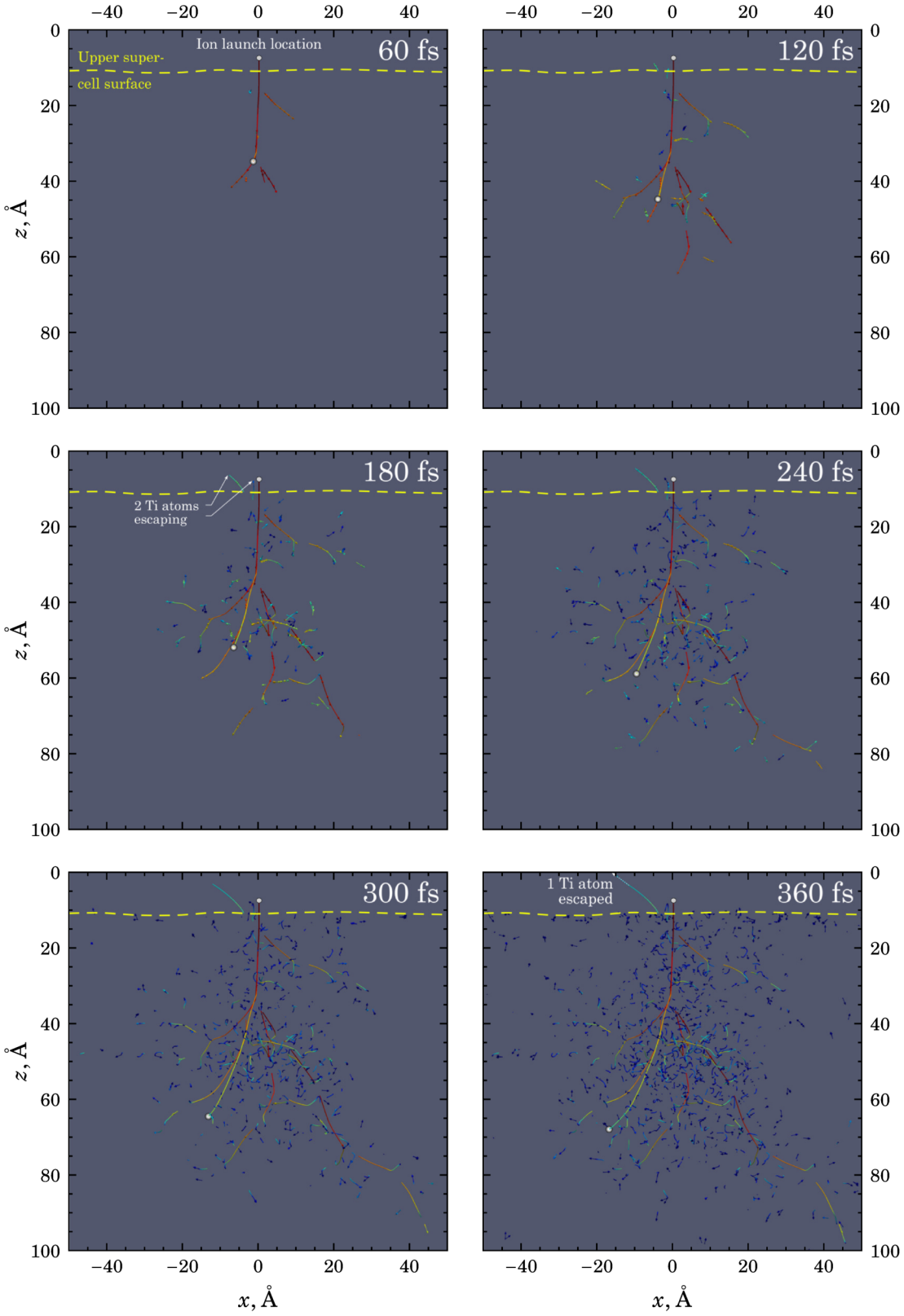


Figure 4.5 **Case:** $E_{\mathrm{Xe+}} = 1.4\,\mathrm{keV}$, $\beta = 0\,\mathrm{deg}$, run 1. Snapshots of collision cascade the first 360 fs after the ion is launched onto the Ti target.

Snapshots of atomic trajectories the first 360 fs of the collision cascade are shown in Figure 4.5. The pathlines are filtered to only show trajectories which are longer than 2 Å and are colored by their velocity magnitude, logarithmically scaled from $0.1 - 50\,\mathrm{km\,s^{-1}}$. The dashed yellow line denotes the upper surface boundary of the initial MD supercell. The first collision of the ion with the PKA occurs at 15 fs, which experiences a drastic velocity decrease of $5\,\mathrm{km\,s^{-1}}$, visible in the snapshot at 60 fs, where the PKA is launched throughout the bulk material to subsequently collide with several secondary and tertiary atoms (see $t = 120$ fs onwards). Further, it can be observed how the ion experiences a second and third collision ($\Delta z \approx 35$ Å) losing another $10\,\mathrm{km\,s^{-1}}$ of velocity during these processes. At 120 fs, the collision cascade can be considered initiated, while at $t = 180$ fs *two* Ti atoms are ejected with high velocity outwards from the target material (see annotation), crossing the initial yellow upper surface boundary. However, the kinetic energy of the second atom (close to $x = 0$) is not sufficient to overcome the attractive potential energy of the surrounding bulk atoms and subsequently returns to the target (see $t = 300 - 360$ fs). This is not the case for the first escaping, more energetic atom which is capable to overcome the attraction and crosses the upper MD $z-$domain boundary condition and can be considered a *sputtered* atom.

The second step in carrying out principal analyses was the case of maximum impact energy at 70 deg impact angle. In this scenario, the PKA and secondary collision events play an even bigger role, since their location and kinetic energy vectors are the major quantities influencing how many atoms will be sputtered in total. In Figure 4.6, two 3D views at $t = 0$ and $t = 2$ ps after impact are shown, similar to Figure 4.2. In this particular case (run 3), 4 atoms were sputtered and a clear region of blue, non-hcp atoms is visible. Furthermore, compared to the normal incidence case the ion implantation location has shifted drastically upwards with the ion residing very close to the surface boundary after it has come to rest. Actually, the non-hcp liquid region is located *behind* the implantation location, indicating that the highest lattice temperature region is produced within the vicinity of the first collisions in the 70 deg case. In the first few hundreds of femtoseconds, atoms are forced out of their local hcp structure due to their kinetic energy absorbed from collisions with the impacting ion and primaries. Since these events take place in a very small region around the ion trajectory through the bulk, one cannot regard this conversion as a process related to Maxwellian type temperature but to *individual* atoms with enough kinetic energy to overcome the attractive forces of the surrounding hcp lattice. This process continues until enough collisions occurred with neibouring atoms in order for the highly non-equilibrium temperature distribution

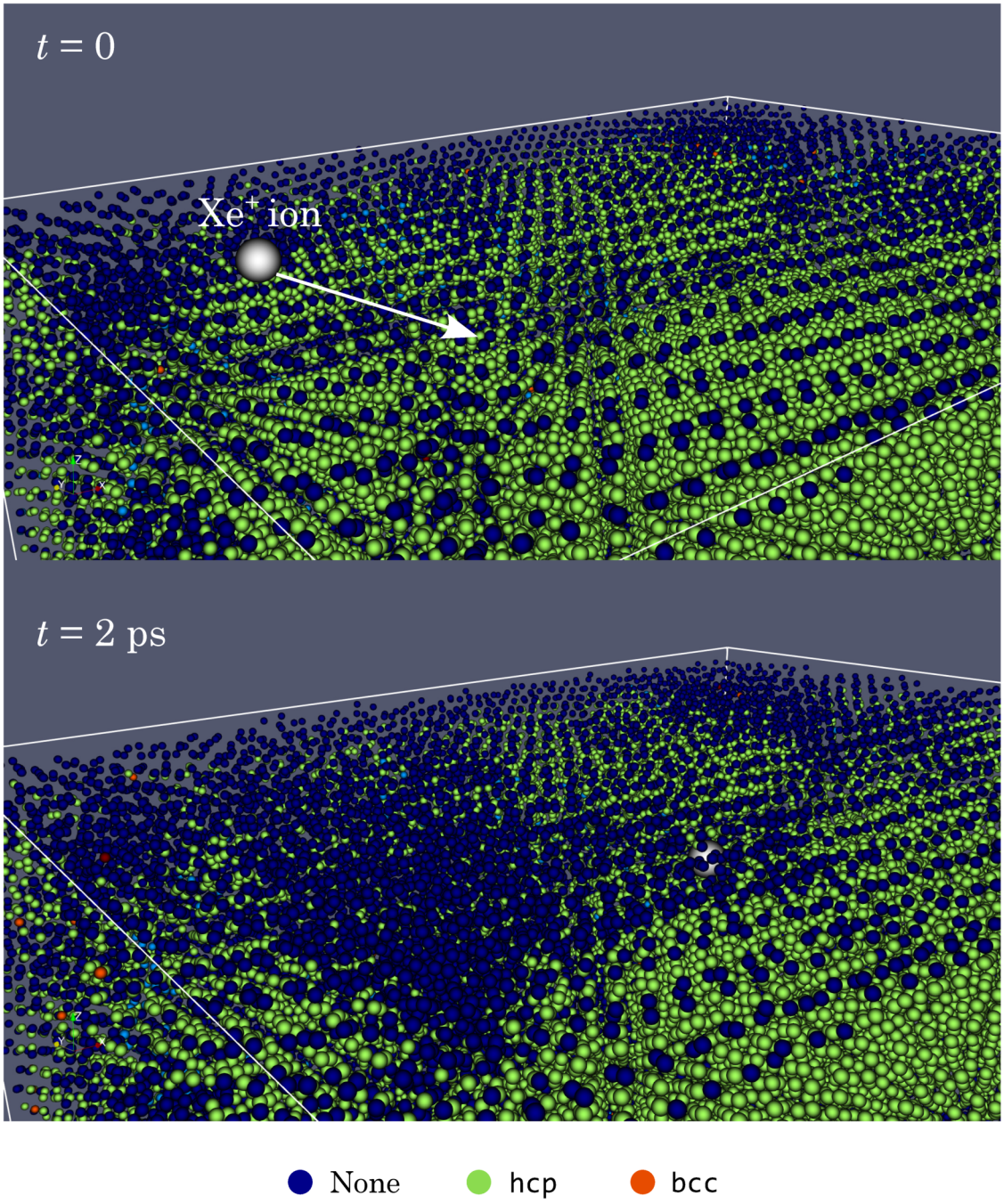


Figure 4.6 **Case:** $E_{\mathrm{Xe+}} = 1.4\,\mathrm{keV}$, $\beta = 70\,\mathrm{deg}$, run 3. Comparative illustration to Fig. 4.2; impact zone with blue atoms indicating atoms in liquid state.

becoming of Maxwellian type, responsible for melting in outer regions which are not immediately affected by the impacting ion.

Plots of the temporal evolution of the ion velocity and penetration depth are shown in Figure 4.7. The plots of major energy losses look similar to Figure 4.1, however, the duration for the ion to reach resting velocity increases to 0.7 ps, while

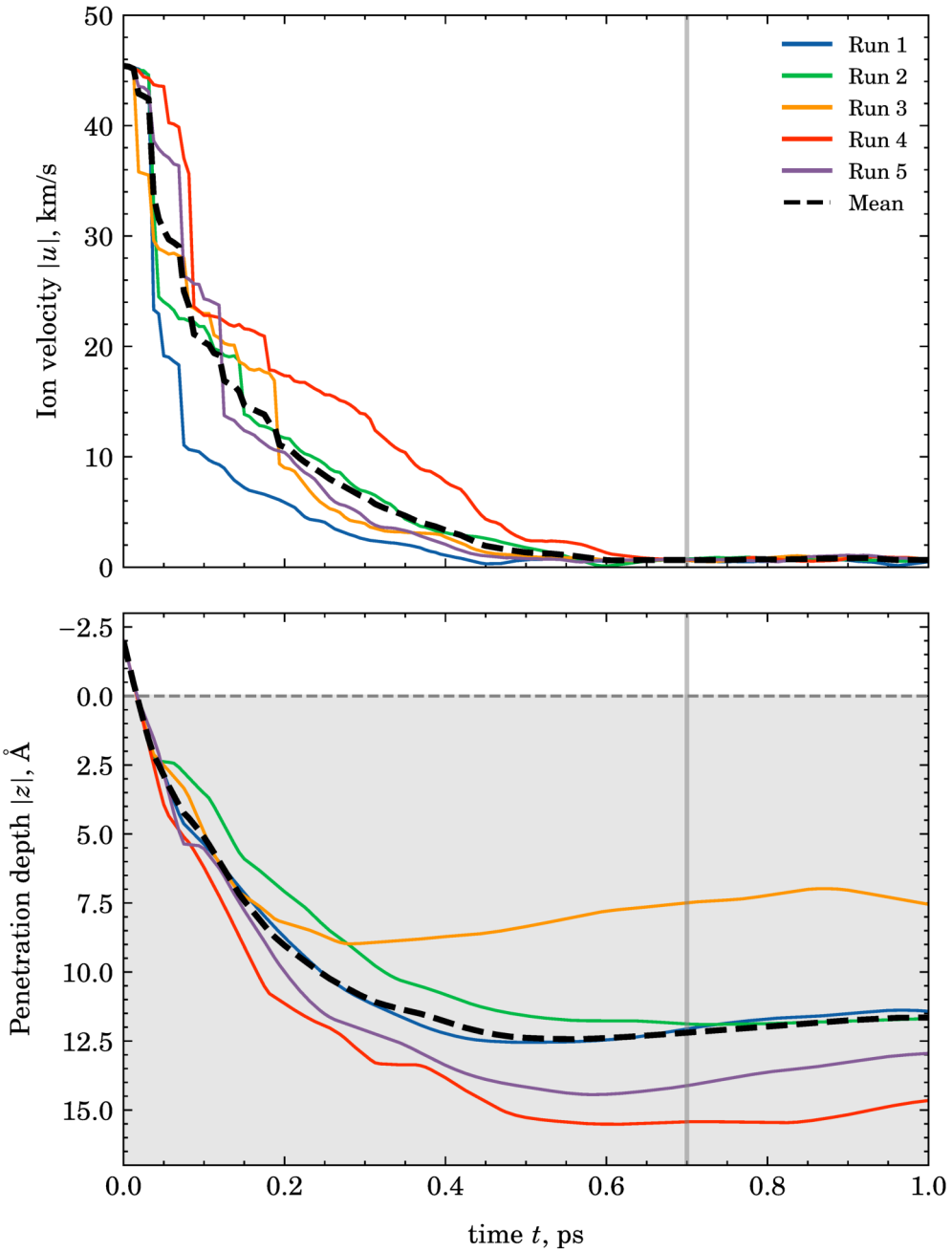


Figure 4.7 **Case:** $E_{\mathrm{Xe+}} = 1.4\,\mathrm{keV}$, $\beta = 70\,\mathrm{deg}$. Comparative illustration to Fig. 4.1. The mean penetration depth decreases by a factor of 0.3 to 12 Å; the mean duration for the ion to come to rest increases from 0.6 to 0.7 ps.

the total penetration depth $|z|$ decreases by a factor of 3 to about 12 Å. An interesting aspect is that the variance of $|z|$ has reduced significantly. The mean difference from the mean penetration depth is just 1.5 Å and no clearly visible outlier is evident. Analyzing the trajectory after the ion has virtually come to rest reveals a small rebound by a few Å, which is attributed to the ion being pushed back by the last

lattice plane it interacted with before losing most of its kinetic energy. This effect clearly manifests itself at run 3 in Figure 4.7.

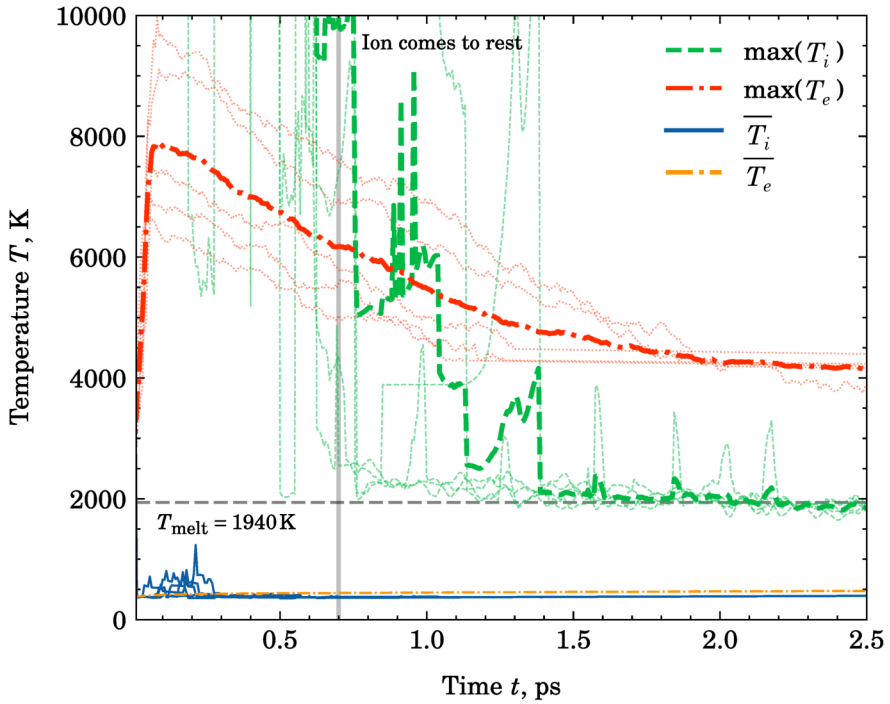


Figure 4.8 **Case:** $E_{\mathrm{Xe+}} = 1.4\,\mathrm{keV}$, $\beta = 70\,\mathrm{deg}$. Comparative illustration to Fig. 4.3. The thermal spike is much more pronounced accompanied by a higher maximum electron temperature of 8000 K compared to normal incidence.

A comparative plot of the time evolution of the voxel atomic and electronic temperatures for the 70 deg case is shown in Figure 4.8. It is evident how the maximum atomic temperature is much higher compared to the one depicted in Figure 4.3 throughout the first 1.5 ps. This circumstance indicates that the thermal spike experienced by the target is more pronounced for higher impact angles. However, it should be noted that energetic atoms ejected from the target into empty vacuum voxels contribute to the huge jumps of T_i since LAMMPS calculates the temperature of voxels based on the atoms inside them, regardless of a threshold. This effect becomes more severe with increasing impact angles as the sputtering rate increases, making it necessary to analyze the electron temperature where this effect was corrected through the implementation of the adaptive electron voxel checking algorithm (see Figure 3.4). A review of the red dashed plot of T_e in Figure 4.8 reveals that the maximum value of T_e approaches 8000 K, representing an increase of more than 20 % compared to the normal incidence case. This observation provides further evidence that a higher thermal spike occurs when β becomes large. After

2.5 ps, the maximum electronic temperature has decayed to 4000 K vs. 2750 K in the normal incidence case at the same impact energy. In both cases, the mean electronic and atomic temperatures of the entire supercell only slowly increase, which is due to the fact that the supercell is large compared to the initially affected irradiation region, and the thermal conductivities κ_e and κ_i of titanium are very low compared to other metals.

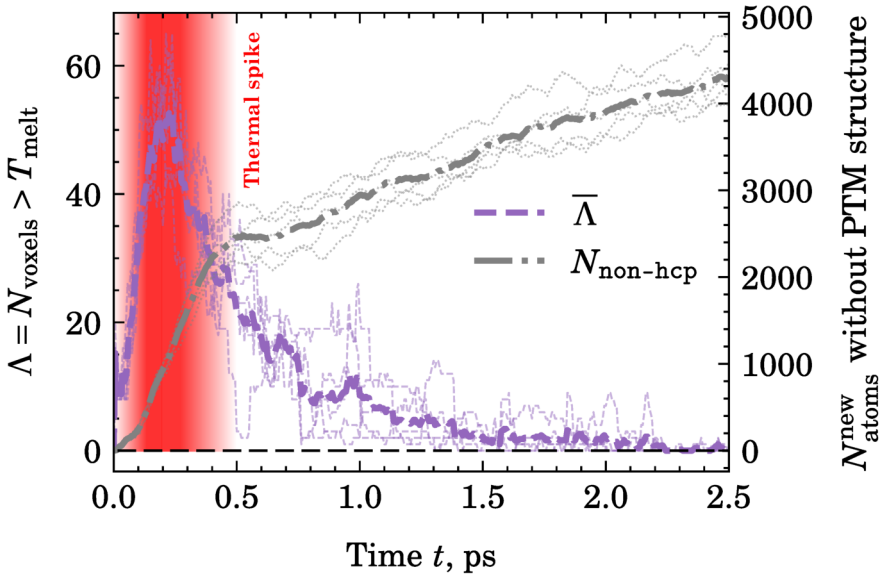


Figure 4.9 **Case:** $E_{\text{Xe+}} = 1.4\,\text{keV}$, $\beta = 70\,\text{deg}$. Comparative illustration to Fig. 4.4. Thermal spike indicated by red zone from 0 – 0.5 ps after impact, maximum number of voxels above T_{melt} at 0.2 ps.

The thermal spike appearing the first few hundreds of femtoseconds is shown in Figure 4.9. The maximum number of voxels with a temperature above T_{melt} is, on average, 35 % higher compared to the normal incidence. Interestingly enough, the number of non-hcp atoms is 15 % lower. This effect may be attributed to the region of primary and secondary atoms being closer to the target surface, thus a reduced number of neighboring atoms is encountered by them and results in the total kinetic impact energy absorbed by fewer atoms and would support the finding of the increased thermal spike for high impact angles.

An illustration of the atomic trajectories during the first 360 fs of the collision cascade at $\beta = 70\,\text{deg}$ incidence are portrayed in Figure 4.10. The trajectories were filtered with a cutoff of 2 Å, only showing atoms which have traveled more this distance in the current timeframe. Compared to normal incidence (see Figure 4.5), the PKA immediately gets ejected ($t = 90\,\text{fs}$) while the ion continues to collide with atoms close to the surface, producing more sputtered atoms. If the velocity

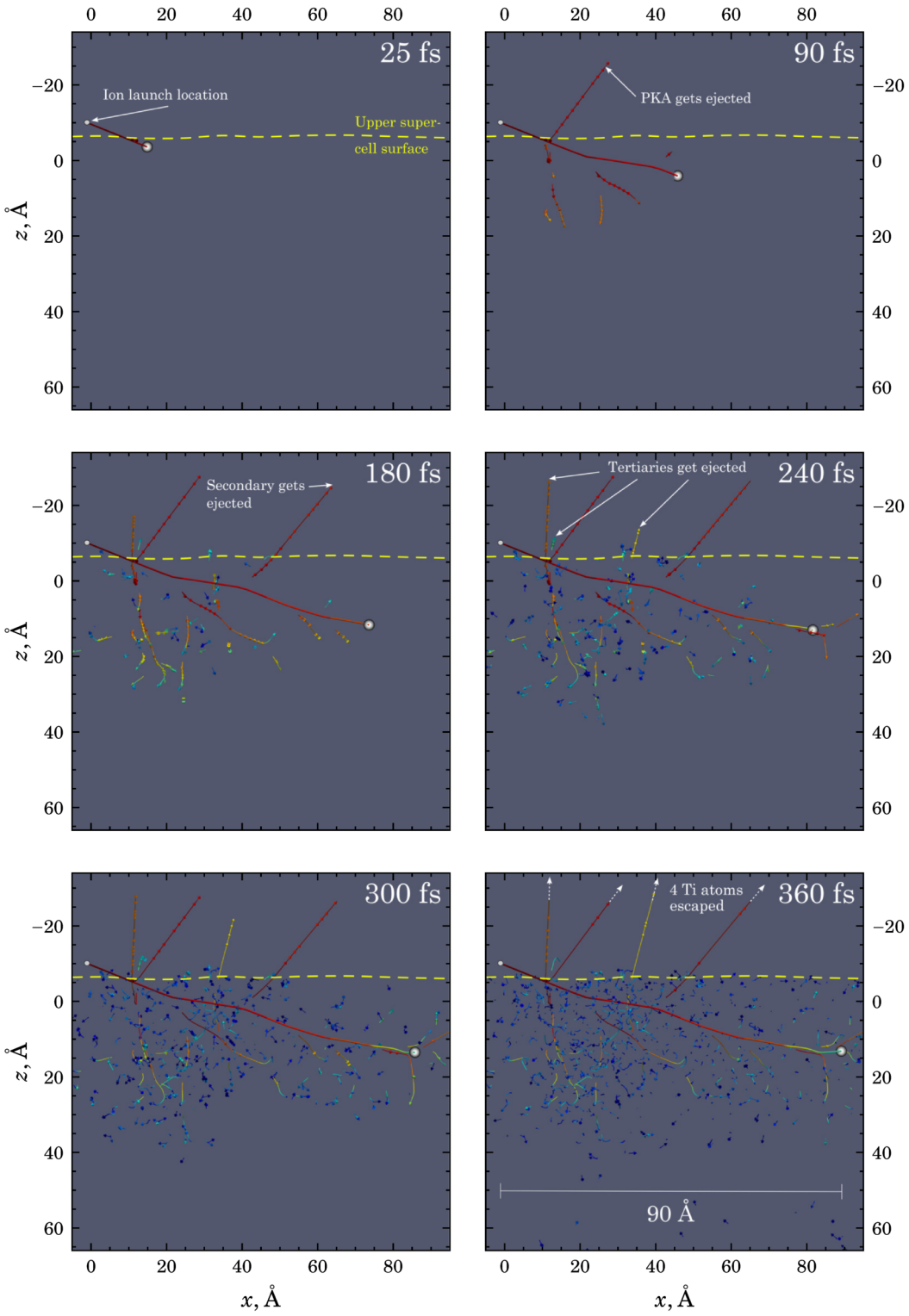


Figure 4.10 **Case:** $E_{\mathrm{Xe+}} = 1.4\,\mathrm{keV}$, $\beta = 70\,\mathrm{deg}$, run 5. Comparative illustration to Fig. 4.5. Atomic trajectories of collision cascase the first 360 fs with 4 sputtered atoms. Logarithmic velocity contours from $1 - 50\,\mathrm{km\,s^{-1}}$ (blue to red).

vector after collision with the ion or primary atoms points into the target, the collision cascade commences from there and becomes less intense the more the ion penetrates the target. In this run, the ion traveled an axial distance of 95 Å and was able to penetrate the target up to 14 Å.

Finally, three-dimensional volume rendering contours of the atomic voxel temperature are outlined in Figure 4.11 with the continuous colormap scaled from blue: 350 K to red: $T_{\text{melt}} = 1941\,\text{K}$. At $t = 0.2\,\text{ps}$, during the maximum of the thermal spike, a small zone of extremely energetic atoms is present and sharply defined considering that the contours evolve almost discontinously from red to blue. At $t = 0.5\,\text{ps}$, the impacting ion has already completed most of its total penetration depth and released its kinetic energy to the target atoms. The collision cascade is initiated and the most energetic atoms are able to penetrate the target themselves by few tens of Å indicated by the red voxel zones around the ion. At $t = 1.0\,\text{ps}$ these atoms have traversed the target outwards from their initial knock-on with the surrounding zone affected by the ion already being in a state of relaxation where the voxel temperatures start falling below the melting temperature. At $t = 1.5\,\text{ps}$ the energetic atoms have slowed down and the initially very hot regions commence with equilibriation by lattice heat conduction and electron-phonon coupling (which takes long compared to other metals due to titanium's low thermal conductivity). Finally, At $t = 2.5\,\text{ps}$ all voxels are below the melting temperature. No more individually hot voxels – apart from the impacting zone – are visible and the supercell tends towards thermal equilibrium by slow transport of heat away from the impacting zone.

4.1.2 Parameter study

The theoretical analysis carried out in the previous section laid the foundation for understanding the physical processes governing the dissipation of kinetic energy in the target, specifically the transition from the thermal spike to the collision cascade the first 200 – 500 fs after the PKA is initiated. These analyses are of interest from a theoretical standpoint, however, designers and engineers of EP thrusters and new material compounds are mostly interested in the sputter yield and penetration depth of ions in order to improve life times of EP thrusters. This section is intended to fulfill the aforementioned engineering interests, as well as to establish a connection between fundamentally theoretical analysis and practical applications in the real world. The reader is reminded that the methodology for obtaining sputter yields is described in sec. 3.4.5.

A conclusive figure containing all investigated angles and energies with corresponding yields and penetration depths is given in Figure 4.12. Each row represents

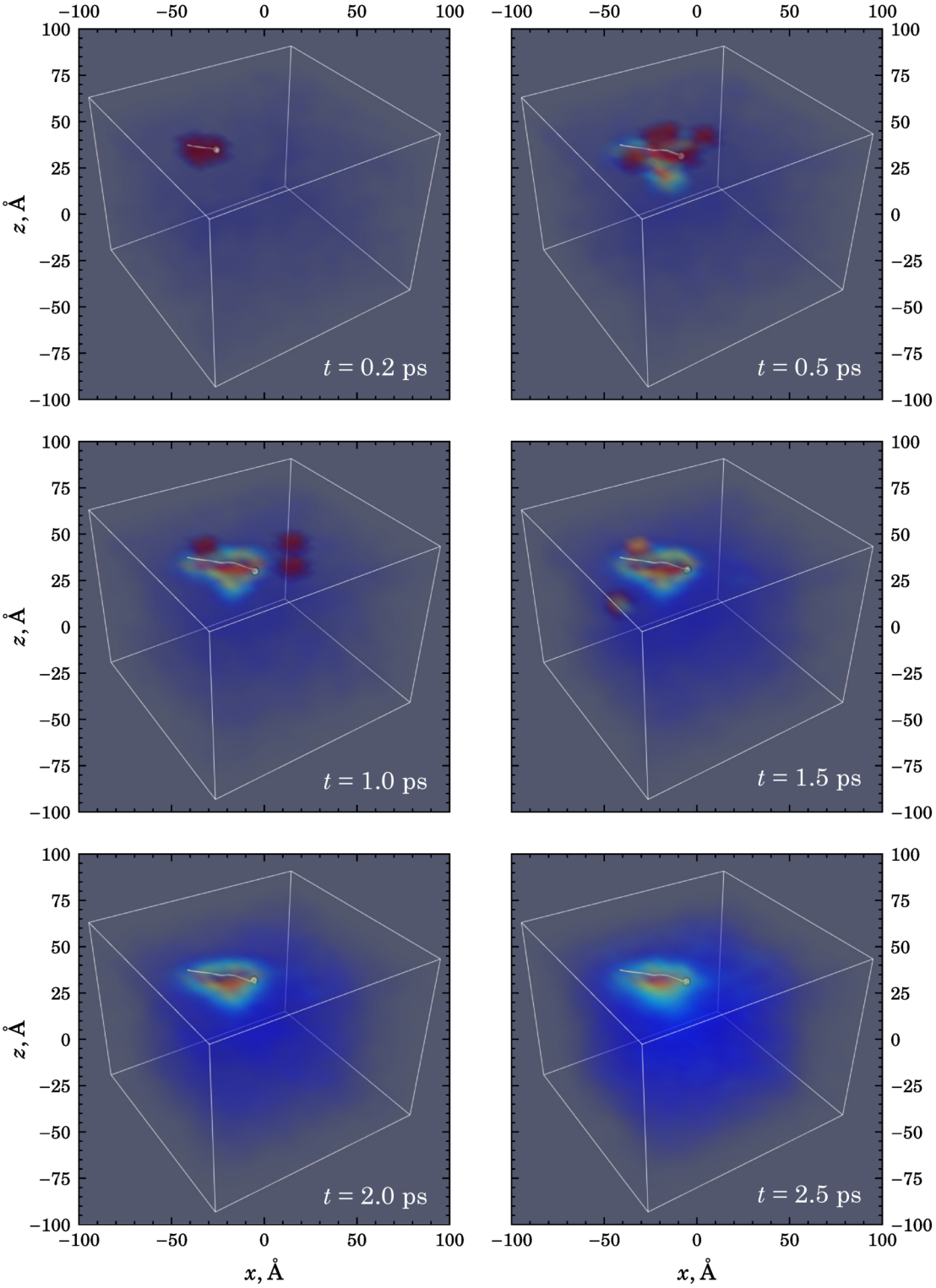


Figure 4.11 **Case:** $E_{\mathrm{Xe+}} = 1.4\,\mathrm{keV}$, $\beta = 70\,\mathrm{deg}$, run 3. Volume rendering of atomic voxel temperature the first 2.5 ps after ion is launched. Colormap scaled to $\min(T) = 350\,\mathrm{K}$ and $\max(T) = T_{\mathrm{melt}} = 1941\,\mathrm{K}$.

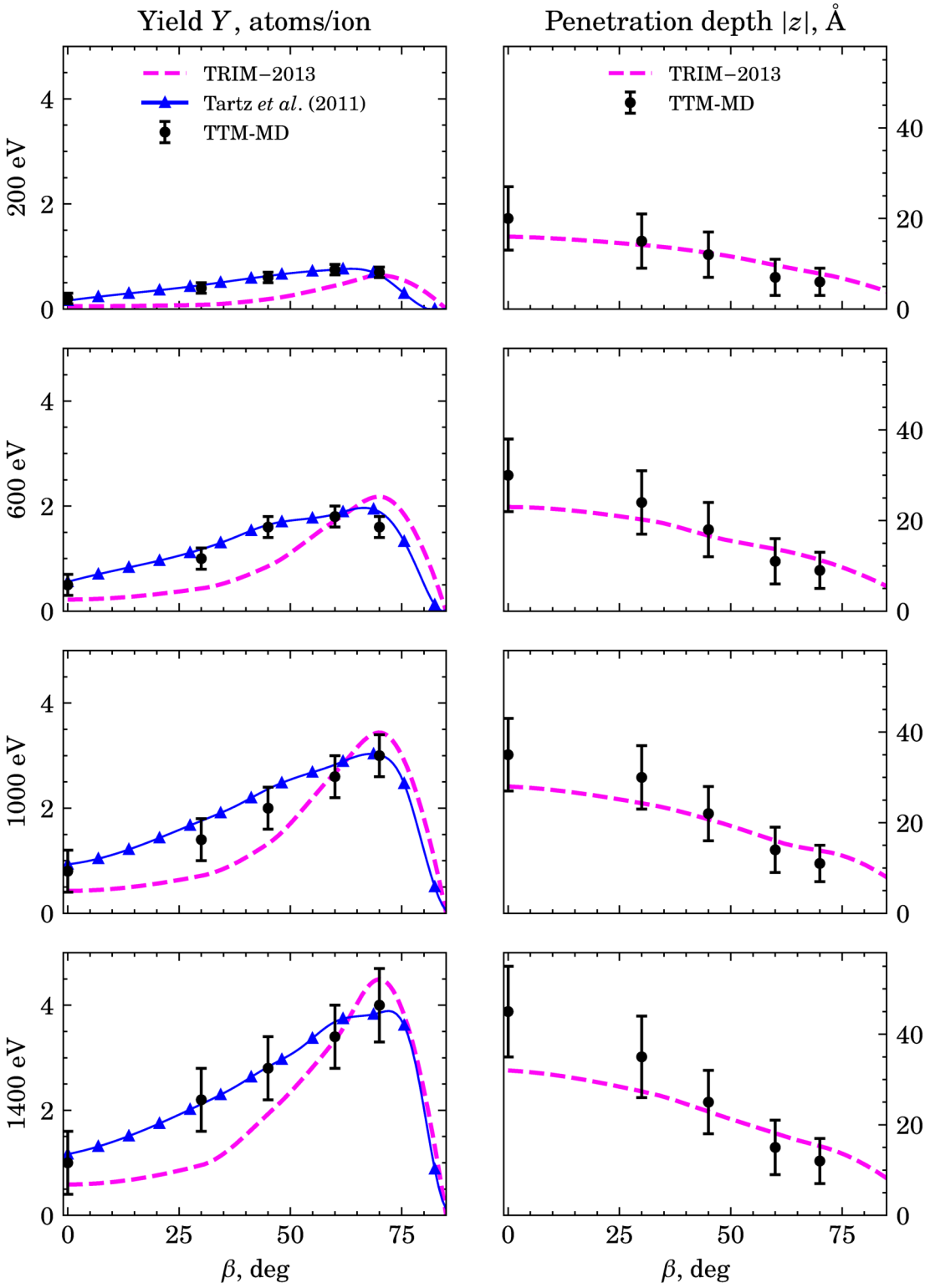


Figure 4.12 Ti parameter study of yield and penetration depth including comparison with experimental data from Tartz, Heyn, Bundesmann, Zimmermann, *et al.* [60] and Ziegler *et al.* [68] (denoted as TRIM–2013).

a specific ion impact energy, and the $x-$axes indicate variations of the impact angle. The left column outlines plots of the yield while the right column denotes the penetration depth. Error bars were determined by taking the average deviation from the average of all runs of a case according to

$$\epsilon\left(\phi\right) = \frac{\overline{\Delta\phi}}{\overline{\phi}}\,, \quad \phi \in \left\{Y, |z|\right\}. \tag{4.1}$$

Since the TTM–MD simulations were carried out 5 times per case, the error bar at $E = 1400\,\mathrm{eV}$ and $\beta = 70\,\mathrm{deg}$ results from the 5 simulations giving a yield and (mean) error of:

$$\begin{aligned} Y &= \frac{Y_1 + Y_2 + Y_3 + Y_4 + Y_5}{5} \\ &= \frac{3 + 4 + 3 + 6 + 4}{5} = \underline{\mathbf{4.0}}\,, \\ \epsilon(Y) &= \frac{\Delta Y_1 + \Delta Y_2 + \Delta Y_3 + \Delta Y_4 + \Delta Y_5}{5} \\ &= \frac{|4-3| + |4-4| + |4-3| + |4-6| + |4-4|}{5} = \underline{\mathbf{0.8}}\,. \end{aligned}$$

Available experimental data, in this case by Tartz, Heyn, Bundesmann, Zimmermann, *et al.* [60], is highlighted by the blue, triangle-marked graph along with results obtained from TRIM–2013 [68] using MC cascade simulations of 1000 ion impacts per case, which is highlighted by the pink dashed graph.

In general, it can be observed that the TTM–MD calculated yields are in good agreement with the experimental data. This agreement is characterized by small deviation of the simulated mean values from the experimental data and the fact that the experimental data remains within the error bars throughout all simulations in contrast to the TRIM–2013 calculated results, which feature underpredictions of the experimental yield data for $\beta < 60\,\mathrm{deg}$ and overpredictions for $\beta > 60\,\mathrm{deg}$. Moreover, the TTM–MD simulation better matches the experimental data especially for high energy domain where using TRIM–2013 results in underpredictions becoming more severe for higher impact energies.

Experimental data of singular ion implantation or penetration depths in the realm of few tens of Å after keV irradiation could not be found, since the research of (xenon) ion implantation depths is mostly focused on MeV irradiation due to practicality reasons [143–145]. Thus, for comparisons with penetration depths, one relies on the results determined from comparisons with TRIM–2013 calculations,

portrayed in the right column. The TTM–MD results show a clear trend of predicting deeper penetration depths at small angles, while smaller penetration depths are generally predicted for $\beta > 50\,\text{deg}$. This observation corresponds well to the trends observed for the yield, where TRIM–2013 underestimates Y towards normal incidence and overestimates Y for large values of β. These differences in the predictions may be explained by the detailed resolution of interatomic interactions governed by hybrid potentials, i.e., Coulomb type close-range interactions between the ion and the target atoms, and the MEAM potential between the target atoms themselves as utilized in this thesis. The detailed description of interatomic forces is not employed in TRIM–2013, rather a semi-analytical approach based on the MC method. Compared to the *ab-initio* method employed in this thesis, the computational cost is smaller and is able to produce a good estimate for titanium, as the trend for the penetration depth is mostly captured and the TRIM–2013 data largely enclosed by the error bars from the TTM–MD simulations.

4.2 Graphite

In this section, results of the TTM–MD simulations of graphitic carbon, commonly used in RIT grids, are presented.

4.2.1 Principal analysis

Comparative plots of the ion velocity and penetration depth with respect to time at maximum energy and normal and 70 deg incidence are outlined in Figure 4.13. In contrast to the temporal evolution of the titanium case, two major differences are observed. Firstly, the variance of both the ion velocity and penetration depth evolution from the mean (dashed black graph) is much smaller as well as no clear outlier is visible. Secondly, the nuclear stopping power is significantly stronger due to the strong bonds between the hexagonal carbon rings. After already 0.4 ps, the ion has dissipated more than 90 % of its kinetic energy and has reached the maximum penetration depth. From there, the ion reaches the *inter–layer bouncing* phase, where it bounces back and forth between the graphene layers. In both the normal incidence and 70 deg case, the ion's velocity linearly decreases for the following 2 ps until it comes to rest and only moves with thermal velocity through interaction with the surrounding carbon atoms. In the $\beta = 70\,\text{deg}$ case, the bouncing phase is reached already twice as early at 0.2 ps, and an increased velocity variance in the first 0.2 ps as a consequence of the ion colliding between the graphene layers due to the relative angle of the trajectory vector with the layer planes, is observed.

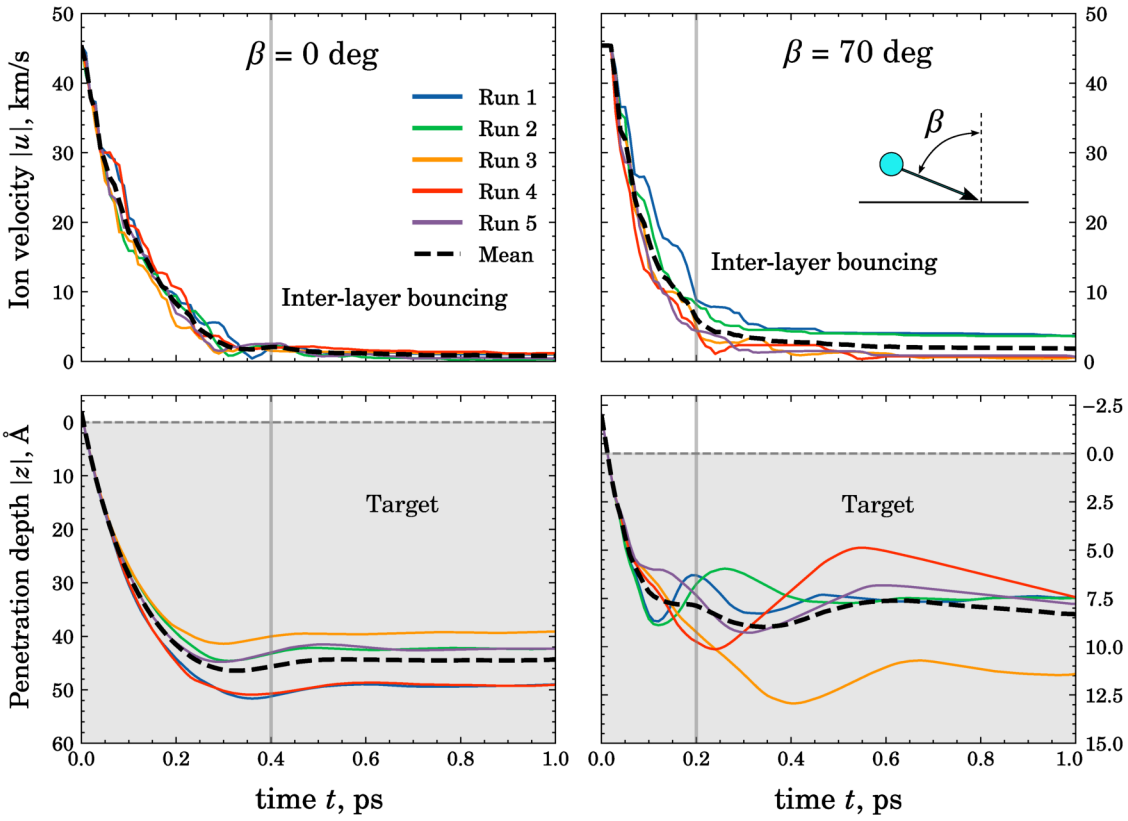


Figure 4.13 **Case:** $E_{\mathrm{Xe+}} = 1.4\,\mathrm{keV}$, $\beta \in \{0, 70\}\,\mathrm{deg}$. Top row: Time-dependent ion velocity of the five different runs with mean values indicated by dashed black line. Bottom row: Time-dependent total penetration depth $|z|$. The time when the ion reaches the *inter–layer bouncing* phase is indicated by the vertical gray line.

The rate of velocity loss when the bouncing phase is reached is comparable to the normal incidence case, however, since the initial velocity at the start of this phase is much higher, the ion still features a velocity of $2\,\mathrm{km\,s^{-1}}$ after 1 ps. For this reason, it is able to axially traverse the target more than 100 Å, just two layers below the surface at an average of 8 Å, in contrast to $|z|\,(\beta = 0\,\mathrm{deg}) = 45\,\text{Å}$. The penetration depth has decreased from 45 Å to 8 Å. In the lower plots, ionic bouncing bewteen graphene layers is more prominently evident, in particular at the $\beta = 70\,\mathrm{deg}$ case, where the penetration depth oscillates around the mean for each case and is dampened with time, respectively.

The temporal evolution of the mean and maximum atomic and electronic voxel temperatures for the normal incidence case at $E = 1400\,\mathrm{eV}$ is shown in Figure 4.14. The aforementioned trend of small variations between the individual runs is also recognizable in this particular plot. The maximum atomic voxel temperature (green dashed line) has small variations and closely follows an exponential decaying curve.

On the other hand, the maximum electronic voxel temperature (red dash-dotted

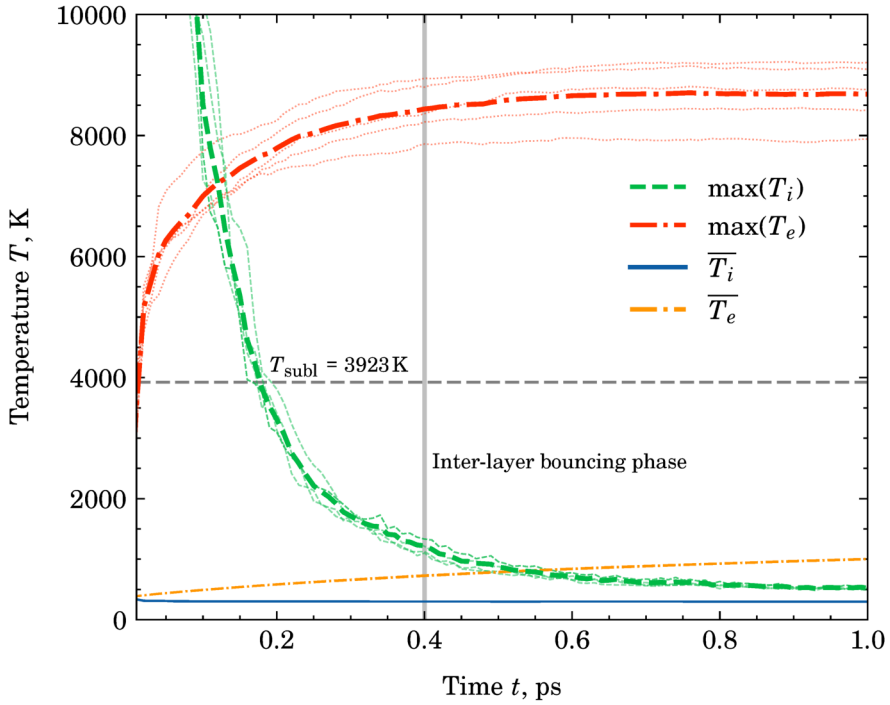


Figure 4.14 **Case:** $E_{\text{Xe+}} = 1.4\,\text{keV}$, $\beta = 0\,\text{deg}$. Temporal evolution of mean and max atomic and electronic voxel temperatures[2].

line) follows a limited growth function, reaching its maximum at $T_e = 8500\,\text{K}$. Due to the very weak electron-phonon coupling parameter of graphite, the dissipation of energy from the electronic to the lattice subsystem leads to the maximum electronic temperature remaining at this high level for the first 1 ps. Simultaneously, heat is dispersed throughout the electronic subsystem as a result of the electronic conductivity, when fast atoms produced by the collision cascade lose parts of their energy through friction with electrons and continues driving the retention of locally high electronic temperature. After 1 ps, the supercell electronic subsystem has reached more than 1000 K, while the atomic temperature is just heated by few tens of K.

Analysing the time-dependent number of voxels above the sublimation temperature of 3923 K reveals that on average a maximum of 10 voxels are situated above T_{melt} only to fall below this level after 0.2 ps at latest. Correspondingly, this specific point in time is also where the maximum number of atoms without PTM structure is reached. The thermal relaxation of the lattice leads to carbon atoms forming bonds again in voxels below the sublimation temperature. An interesting observation is

[2] T_{melt} should be interpreted as the temperature at which carbon sublimates at standard condition. Due to locally very high repulsive forces initiated by PKA and secondary etc. collisions, the "pressure" encountered by individual atoms may be high enough to induce melting instead of sublimation. The author would like to clarify that the usage of the words "melting" or "sublimation" should be regarded to as individual extractions of atoms from PTM identified `graphite` lattice structure to PTM = 0 of the $i-$th atom.

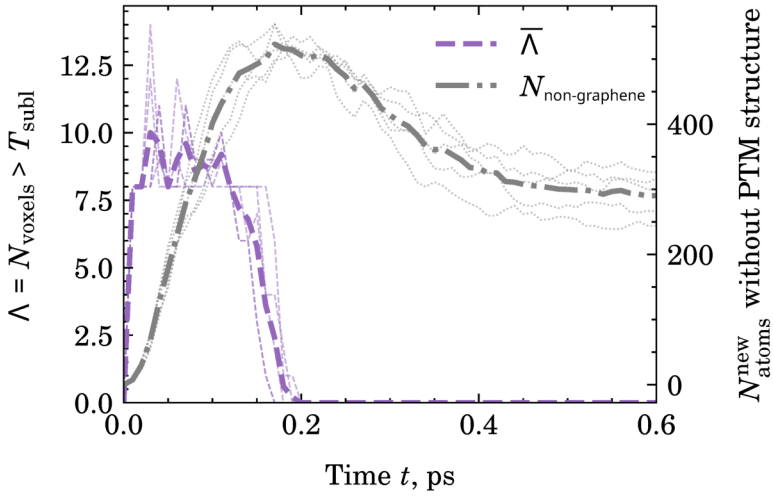


Figure 4.15 **Case:** $E_{\text{Xe+}} = 1.4\,\text{keV}$, $\beta = 0\,\text{deg}$. Temporal evolution of voxels above sublimation temperature and atoms forced out of their graphite lattice structure.

that despite this fact, more than 500 atoms are not located in the graphene lattice, implying that Maxwellian temperature (i.e., continuum type temperature) actually is indeed **not** the main driver of sublimation during ion irradiation[3], at least not the first 1 ps, but the physical dislocation of singular atoms from their lattice.

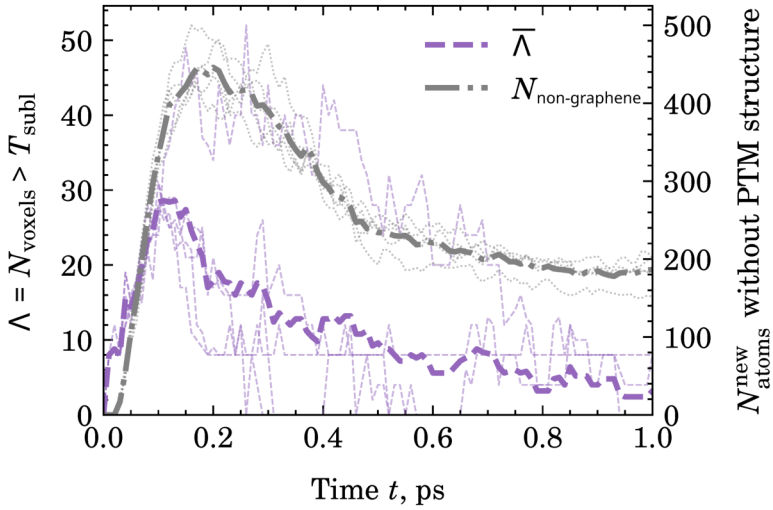


Figure 4.16 **Case:** $E_{\text{Xe+}} = 1.4\,\text{keV}$, $\beta = 70\,\text{deg}$. Temporal evolution of voxels above sublimation temperature and atoms forced out of their graphite lattice structure at high angle of incidence. About 3× as many voxels are forced above T_{melt} but the same number of atoms forced out of their PTM structure.

At high angle of incidence, the irradiation instigates a different trend, where

[3]It is assumed that melting/sublimation is defined as atoms not located in their PTM identified structure at the ensemble temperature according to the phase diagram of the material.

3× as many voxels achieve melting temperature in the same timeframe of 0.2 ps, followed by an exponential decay taking 0.8 ps. Nonetheless, the final value of 300 non-graphene atoms remains the same after 1 ps compared to normal incidence.

A closeup of the atomic trajectory the first 1 ps after the ion is launched onto the target is given in Figure 4.17. In the left column, a bird's eye view looking from $+z$ towards $-z$ direction onto the surface of the target is outlined and in the right column a sideview looking from $-y$ into $+y$ direction is shown, with atoms colored by their PTM identified structure. At $t = 0.1$ ps, the ion traversed the first layer and 2 atoms are ejected directly from the surface layer into the vacuum. Here, fast knockon atoms are launched into their surroundings and produce more non-graphene lattice atoms in the following timeframe. The ion is about to cross the second graphene layer and a deflection wave traveling towards the downside through the target around 30 Å behind the PKA is observable. At 0.4 ps, it has reached the inter-layer collision phase, where it has not enough energy to traverse the fourth graphene layer and force individual atoms out of their graphene lattice, but bounces back and forth between the third and fourth layer. The deflection wave has reached a depth of 20 Å and surface atoms (layer 1) that were of non-graphene lattice type partly start to bind back into the graphene lattice behind the deflection wave through thermal relaxation, which is also visible in the velocity contours becoming weaker following $t > 0.4$ ps.

Christie *et al.* [52] argue that keV radiation damage feedback in graphite is different from metals and oxides due to a lack of a thermal spike and point defects invoked by individual sublimation of C atoms. Although a minor thermal spike is visible in the current study, the sublimation and point defects process can also be reproduced. One of the approaches that Christie *et al.* [52] employed to characterize the relaxation process of the PKA atom[4] was the time-dependent number of atoms with a kinetic energy above 1 eV. They obtained a value of ≈ 0.3 ps and corresponds well with the results of the present study where at normal incidedence and $E_{\mathrm{Xe}^+} = 1$ keV a relaxation time of 0.28 ps for the impacting ion was found. As will be seen in the parameter study (see sec. 4.2.2), Christie *et al.* [52] additionally determined a PKA range very similar to the ion penetration depth identified in this thesis.

4.2.2 Parameter study

Results of the yield and penetration depth parameter study are illustrated in Figure 4.19. Experimentally obtained data of sputter yields were found in the

[4]The existence of the impacting neutron was not taking into account in their study, rather the entire kinetic energy was assumed to be transferred to the PKA.

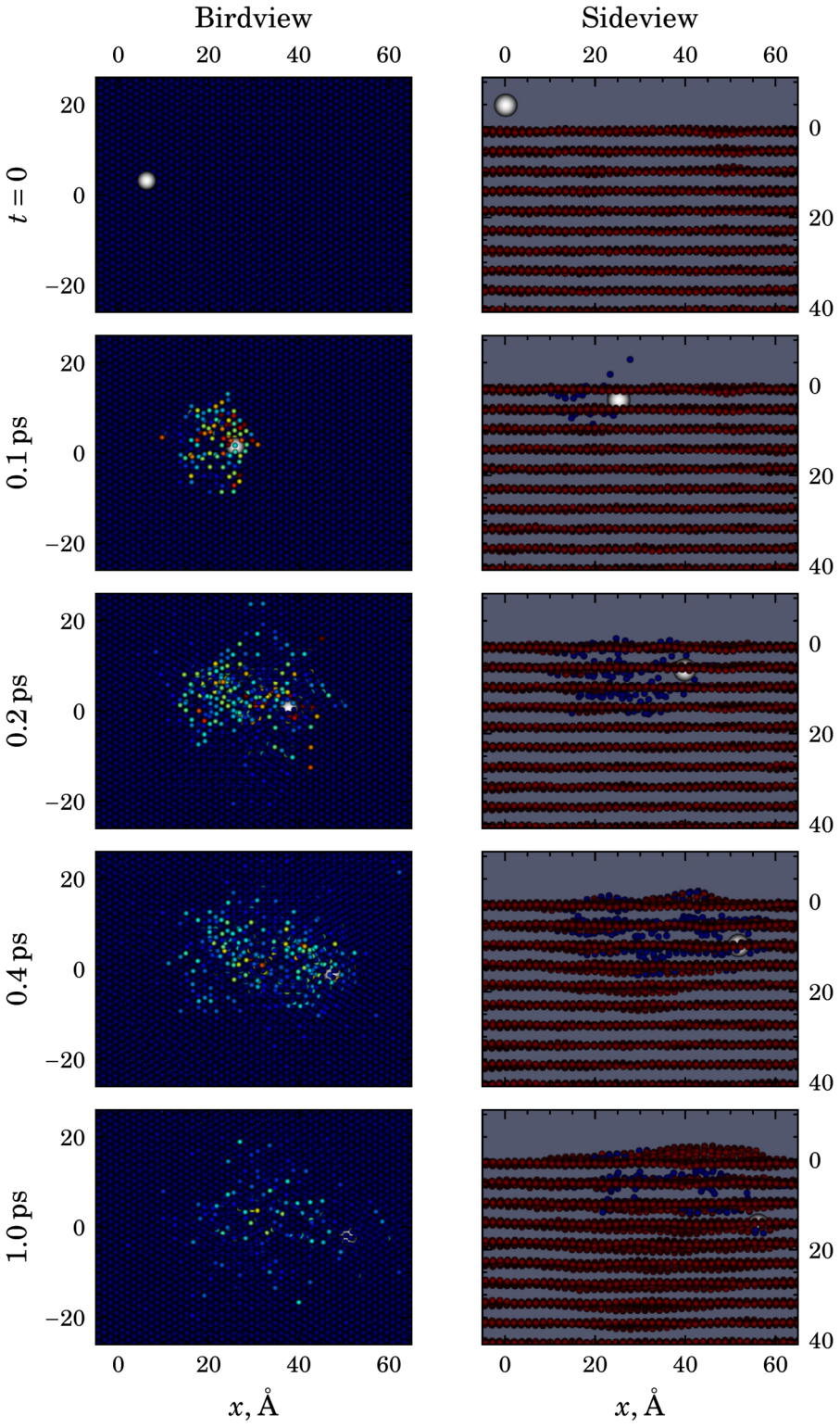


Figure 4.17 **Case:** $E_{\mathrm{Xe+}} = 1.4\,\mathrm{keV}$, $\beta = 70\,\mathrm{deg}$. Closeups of the impact region the first 5 ps. Left: atomic velocity (blue to red: 1 to $100\,\mathrm{km\,s^{-1}}$), right: atoms colored by PTM identification.

publication of Nakano *et al.* [61] in which sputter yields of carbon-carbon composite were semi-empirically characterized built on a developed model and scanning electron microscopy (SEM) images. They tested a 10 cm ion engine with 3-grid configuration (μ−10 EM RIT) and were able to reduce experimental efforts for predicting lifetime of RIT grids.

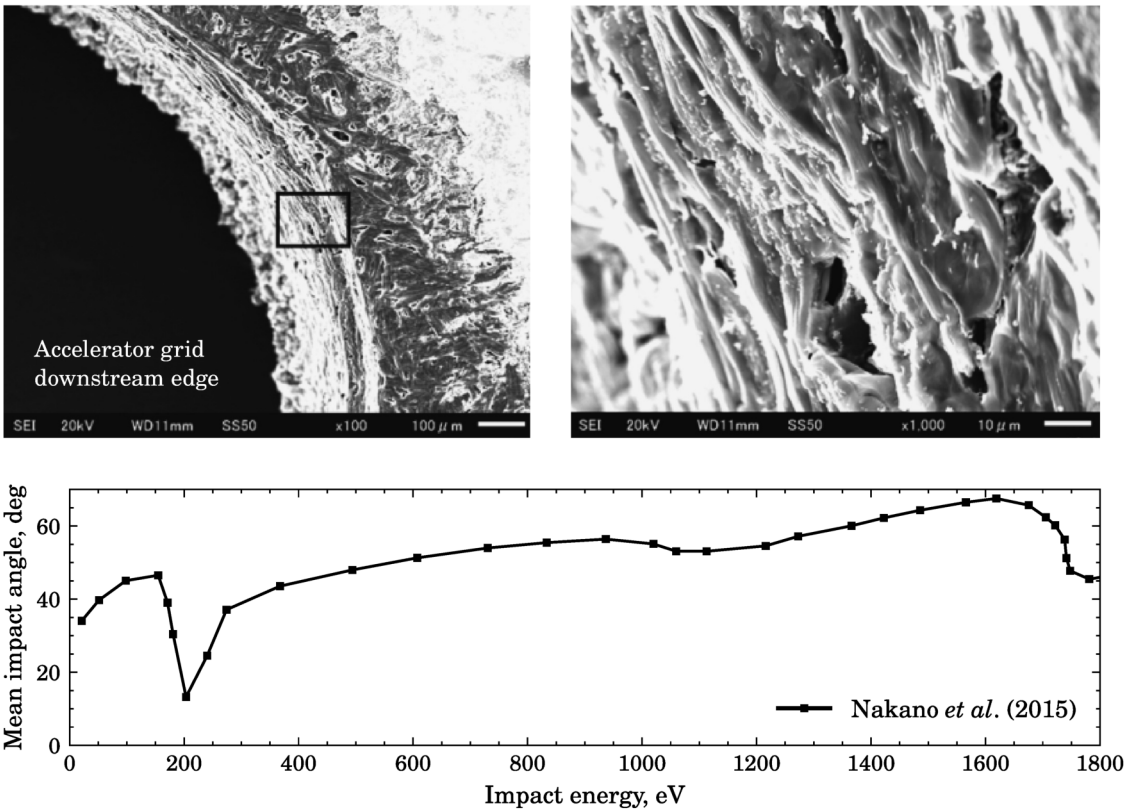


Figure 4.18 Measurements of energy dependent mean impact angle of xenon ions on the μ−10 EM RIT engine accel grid (top) and SEM images of the accel grid downstream edge (bottom left, right). From: Nakano *et al.* [61].

Examples of SEM images of a graphite accel grid subjected to xenon ion irradiation from Nakano *et al.* [61] are shown in Figure 4.18. Additionally, their results of mean impact angles depending on the impact energy are shown in the lower plot. A discernible trend is visible, whereby the impact angle increases in conjunction with the increase in impact energy, reaching a maximum of 65 deg at 1600 eV. Their yield data is plotted as the blue triangle-marked line in Figure 4.19, while the TRIM–2013 calculated data is plotted as the dashed pink line like in Figure 4.12.

For graphite, the results from TRIM–2013 underpredict the yield up to $\beta \approx 40$ deg, after which a subtantial increase of Y is observable, becoming increasingly severe with the rise of impact energy and the impact angle. At $\beta = 70$ deg and

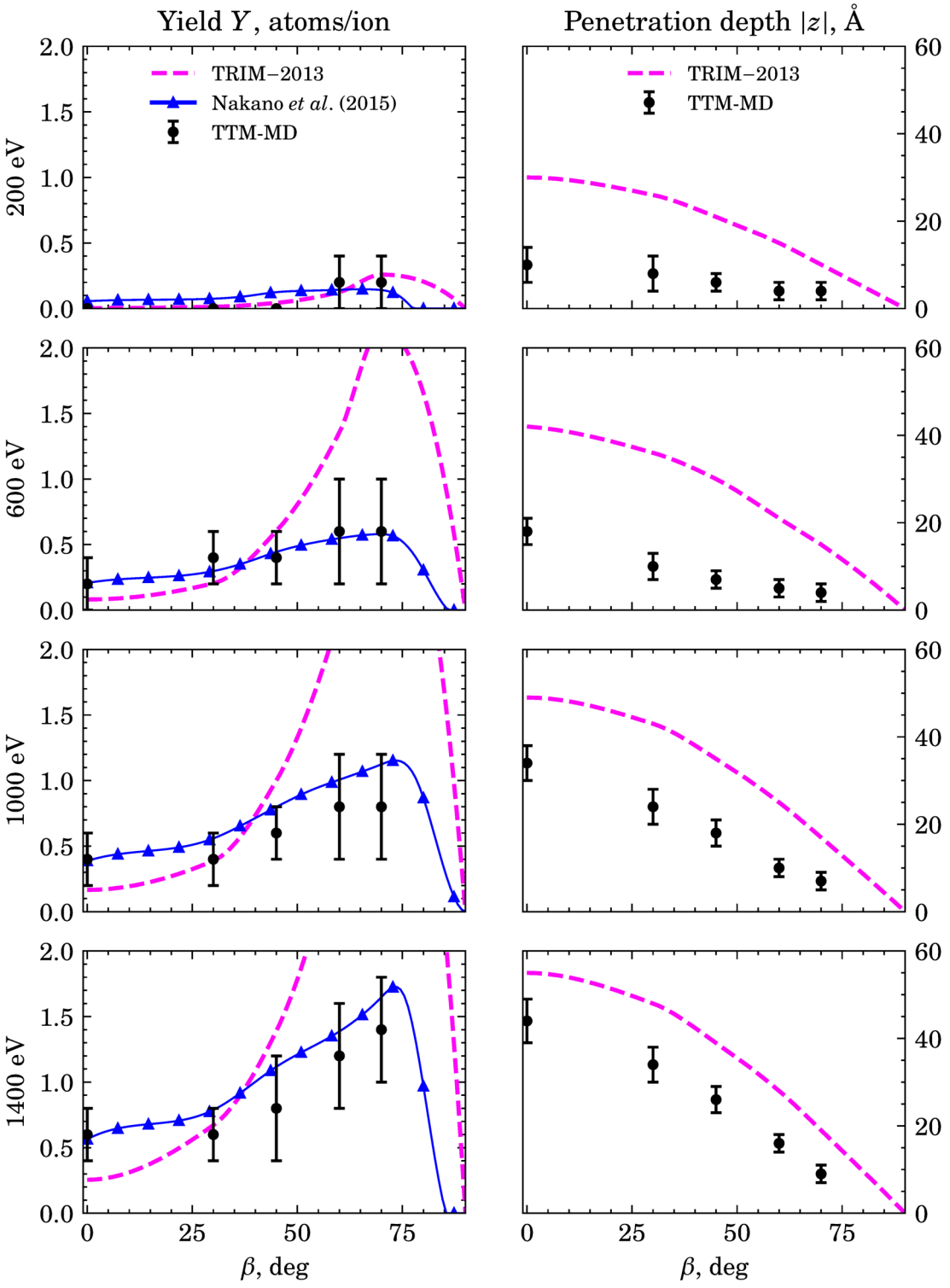


Figure 4.19 C parameter study of yield and penetration depth including comparison with experimental data from Nakano *et al.* [61] and Ziegler *et al.* [68] (denoted as TRIM–2013).

$E = 1400\,\text{eV}$, TRIM–2013 overpredicts the yield by a factor of 2. The TTM–MD results for $E = 200\,\text{eV}$ predict that no atoms are sputtered up to $\beta = 60\,\text{deg}$, hence the error bars are all equal to zero. For $\beta = [0, 70]\,\text{deg}$, 1 out of 5 simulations produced an atom leaving the upper simulation domain, therefore the mean yield is 0.2. Throughout the entire angle range the shape of the penetration depth curve versus angle is similar to the one of TRIM–2013, however, the actual values disagree up to a factor of 3. With higher impact energies, these differences become smaller. For instance, at $E = 200\,\text{eV}$ and normal incidence TTM–MD predicts $|z| = 9\,\text{Å}$ and TRIM–2013 predicts $|z| = 30\,\text{Å}$ while at 1400 eV TTM–MD predicts $|z| = 44\,\text{Å}$ and TRIM–2013 predicts $|z| = 53\,\text{Å}$. This phenomenon can be attributed to the capacity of MD to model the complex carbon-carbon bond interactions, which are crucial for accurate representation in particular in the low impact energy regimes. At elevated impact energies, these bonds are more easily broken, leading to atom-atom interactions that can be assumed of predominantly repulsive Coulomb type fashion as described by the ZBL model. The accurate description of interatomic forces employed in the present MD simulations are underlined by the excellent agreement with the sputter yield experimental data from Nakano *et al.* [61], particularly at an impact energy of 600 eV. At higher impact energies, the trend is closely followed by the TTM–MD predicted data, but the yield is underpredicted by an average of 15 %. Nevertheless, the graphs of the experimental dataset remain well within the error bars of the predicted data.

In the study conducted by Christie *et al.* [52], the MD technique was employed to simulate displacement cascades induced by keV neutron irradiation in graphite. The cascade initiation involved launching a randomly selected PKA of graphite towards the center of the supercell. From a series of up to 20 simulations, the mean ranges of the PKA were determined. Their research explored an irradiation energy range comparable to that investigated in the present study. A comparative analysis of their PKA energy range (100 – 1500 eV) with the data obtained in this study is presented in Figure 4.20. Notably, the error bars in the data by Christie *et al.* [52] results are, on average, twice as large as those in the present study. However, the predicted mean values of the PKA range show excellent agreement between the two studies. This agreement is further supported by the fact that both studies identified similar point defects and local sublimation effects, thereby providing a high level of confidence in the values reported in the current parameter study.

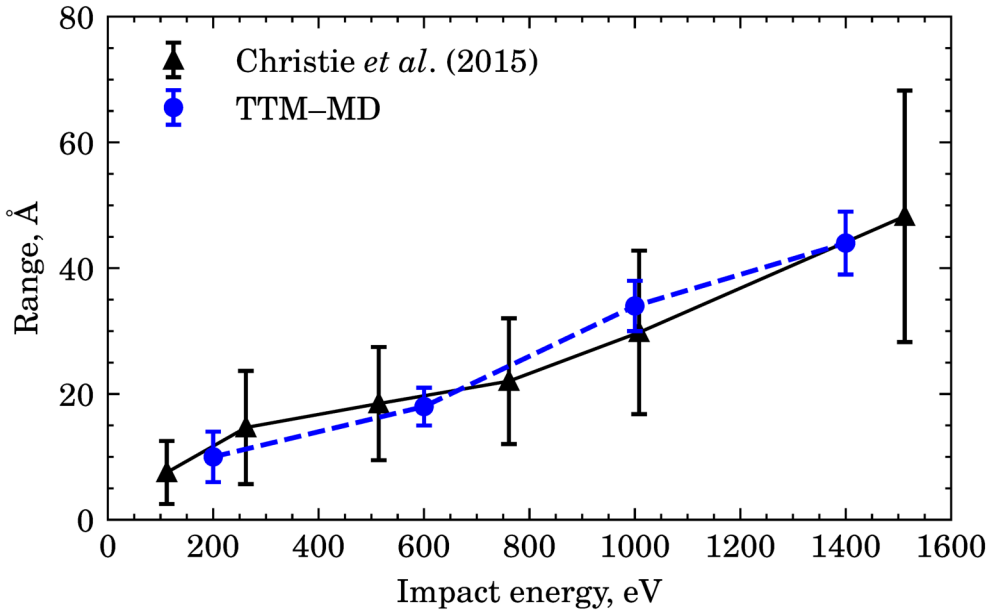


Figure 4.20 Comparison of penetration ranges in graphite subjected to bombardment by fast neutrons (Christie *et al.* [52]) and fast xenon ions (present study, TTM–MD) in the keV regime.

4.3 Quartz

This section addresses the results for quartz (SiO_2), a material commonly utilized in HET channels and RIT discharge chamber walls due to its electrically insulating properties.

4.3.1 Principal analysis

Comparative plots of the ion velocity and penetration depth with respect to time at maximum energy and [0, 70] deg incidence are outlined in Figure 4.21. The initial observation is that the mean penetration depth is markedly greater for the case of normal incidence, down to 130 Å. Indeed, in one run the ion was able to penetrate the target down to the lower boundary conditions, which is why it is not included in the plots of $\beta = 70$ deg. The commonality among all runs is the variance of the temporal evolution of the case-specific velocity relative to the mean velocity evolution is small, with the exception of run 4, representing a minor outlier.

This variance becomes even smaller for the case of $\beta = 70$ deg, except for run 2, where the ion entered the target, experienced 7 collisions while just reaching a maximum of $|z| = 1.5$ Å. Thereafter, one collision led to the ion becoming ejected from the target and subsequently leaving the upper simulation domain. This process occurred after the ion has lost approximately 75 % and 93 % of velocity

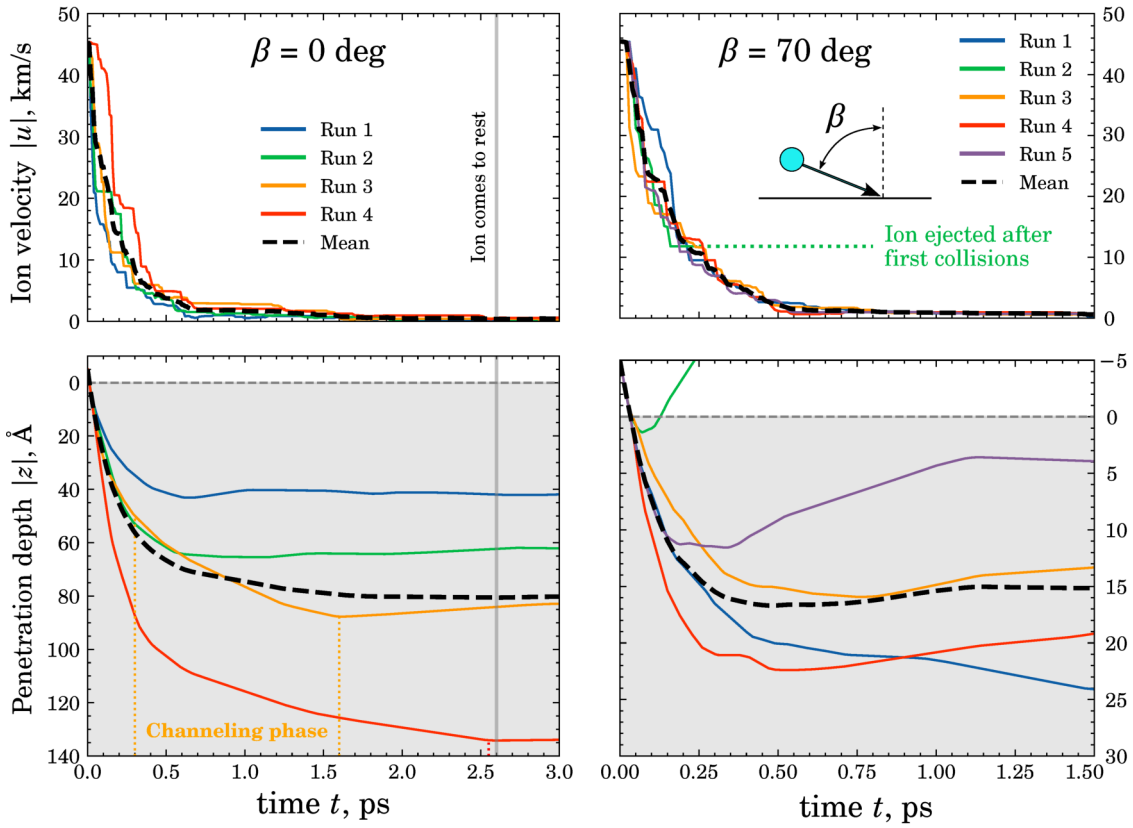


Figure 4.21 **Case:** $E_{\mathrm{Xe+}} = 1.4\,\mathrm{keV}$, $\beta \in \{0,\ 70\}$ deg. Top row: Time-dependent ion velocity of the four different runs with mean indicated by dashed black line. Bottom row: Time-dependent total penetration depth $|z|$.

and kinetic energy, respectively, within the first 0.1 ps. Depending on the alignment of the $\alpha-$quartz layers, channeling effects play an important role in the temporal evolution of the velocity and middle section of the penetration depth, as is the case in this study for normal irradiation incidence. For example, taking run 3 into consideration, the ion first loses most of its velocity the first 0.3 ps after it enters a channel of Si and O atoms. It then keeps bouncing between the surrounding atoms in the channel for 1.3 ps, after it eventually encounters a major collision event at $t = 1.6\,\mathrm{ps}$, which is also the point where the maximum depth is reached. Based on the previously described findings, the entire process of irradiation in quartz can be divided into 3 phases:

1. **Knock-on phase** (0 – 0.5 ps): In this phase the ion collides with the first few layers of target Si or O atoms; on average with 10 collision events, losing more than 90 % of kinetic energy. Depending on the impact angle, the ion may be scattered away from the target, with a probability of $\approx 20\,\%$ at $\beta = 70\,\mathrm{deg}$.

2. **Channeling phase** (0.5 – 2.5 ps): The ion randomly enters a channel and

continously collides with the channel atoms while slowly losing its remaining kinetic energy.

3. **Thermal phase** (> 2.5 ps): The ion encounters a last collision event, either at the end of the channel where a differently oriented crystal grain adjoins, or with an atom inside the channel due to its relative orientation. This virtually brings the ion to rest and it can be considered implanted. From there, it interacts with the thermally governed random movement of the target atoms, at a maximum depth of 80 Å for the $E = 1400$ eV case.

In the present study, most of the crystalline grains were aligned with the $\pm z-$axes, therefore the ion experienced channeling effects mostly for cases where $\beta < 30$ deg. In the absence of these effects, (i.e., at high impact angles) the ion must traverse the higher density of bulk atoms, resulting in a significantly higher collision rate. This is corroborated by the observation that the relaxation time reduces to 0.6 ps.

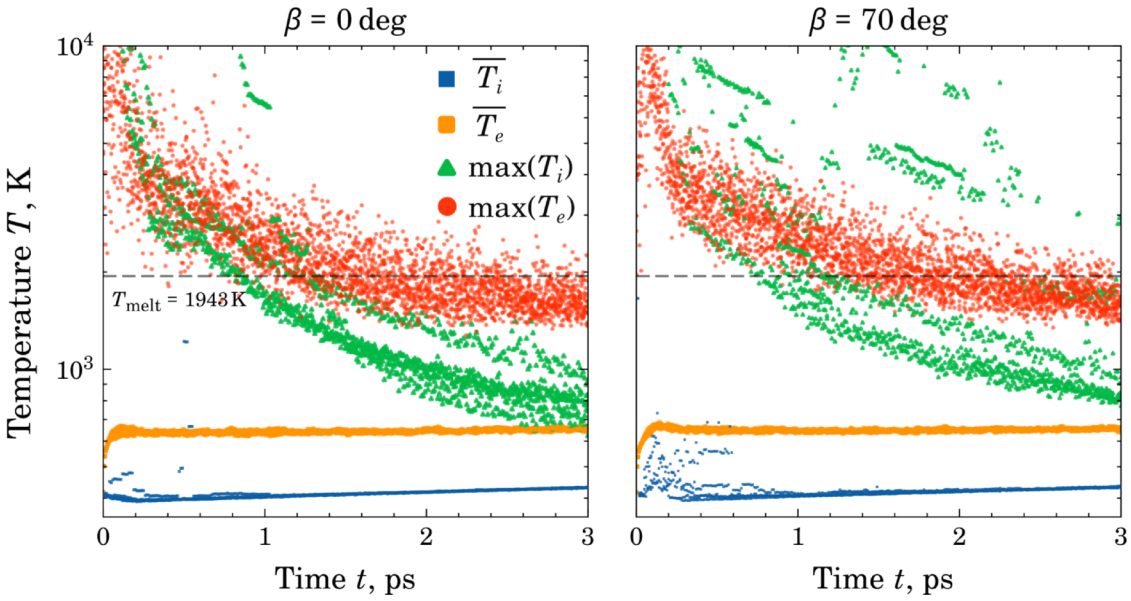


Figure 4.22 **Case:** $E_{Xe+} = 1.4$ keV. Comparison of temporal evolution of mean and maximum atomic and electronic voxel temperatures.

Plots of the atomic and electronic mean and maximum temperature evolution comparing the normal and $\beta = 70$ deg cases are outlined in Figure 4.22. For these plots, a marker-based plotting style was utilized due to the strong noise of data. The scattering of data with many sudden maxima can be attributed to two effects. Firstly, the greater yield producing fast sputtered atoms traversing through empty atomic voxels producing very high maximum temperatures (see elaborations in

sec. 4.1.1). Secondly, the low thermal conductivity of quartz $\lambda = 1.3\,\mathrm{W\,m^{-1}\,K^{-1}}$ resulting in the lattice not being able to transport heat away from the impact affected zones. In the initial 0.5 ps, a multitude of maxima in the mean lattice temperature, denoted by $\overline{T_i}$ are evident in both plots, indicating rapid local heating after which the supercell itself slowly heats up to 450 K compared to the mean electronic supercell temperature reaching 650 K. Similar to the graphite case, the energy required for breaking bonds between Si–O and O–O atomic pairs is so large that already 1 ps after impact, the maximum atomic voxel temperature falls below the melting temperature and after 3 ps the maximum voxel temperature is just ≈ 800 K. Both $\max(T_i)$ and $\max(T_e)$ exhibit exponential decay in similar fashion to the titanium case (see Figure 4.3). although featuring considerably elevated degrees of variance. The maxima in the right plot of Figure 4.22 after $t = 1.0$ ps are fast sputtered atoms traversing atomic voxels from yields reaching up to 15 atoms per case.

Aerial perspectives of the temporal evolution of atomic velocity and ion trajectory length of the first 1.0 ps after the ion is launched at $\beta = 70$ deg is illustrated in Figure 4.23. The plots increase in visual density since the trajectory pathlines of thermal atoms in the bulk also slowly increase in length. The $x-$ and $y-$axis are the axial and radial directions, respectively, while the $\pm z-$axes point in and out of the screen, respectively. At $t = 50$ fs, the ion has experienced 3 collisions with target atoms after having traveled 15 Å. The velocity vectors of the PKAs all point into the target as they initiate the collision cascade, which can be observed at $t = 0.1$ ps and the ion continues to travel through the target closely below the surface undergoing further collisions. In the following snapshot, the ion encounters a collision at $\Delta x = 30$ Å which results in its velocity vector pointing in $+z$ direction. At $t = 0.4$ ps, the straight trajectory of two sputtered atoms can be seen as well as that of the ion, which has left the target and thus is no longer subjected to collisions. An interesting detail can be observed in the vicinity of the initial impact zone, where a Si and an O atom are sputtered. Rather than proceeding along a straight line, these atoms exhibit a behavior akin to orbital motion, driven by their mutual attraction. This phenomenon can be observed a second time at $t = 1.0$ ps, in close proximity to the ion's trajectory.

4.3.2 Parameter study

The results of the parameter study carried out for quartz are shown in Figure 4.24. Acquisition of experimental data for the (total) sputter yield proved to be challenging. The most elaborate dataset that could be found was published by Nenadović *et al.* [63], however, some adaptions were required since they employed argon ions for

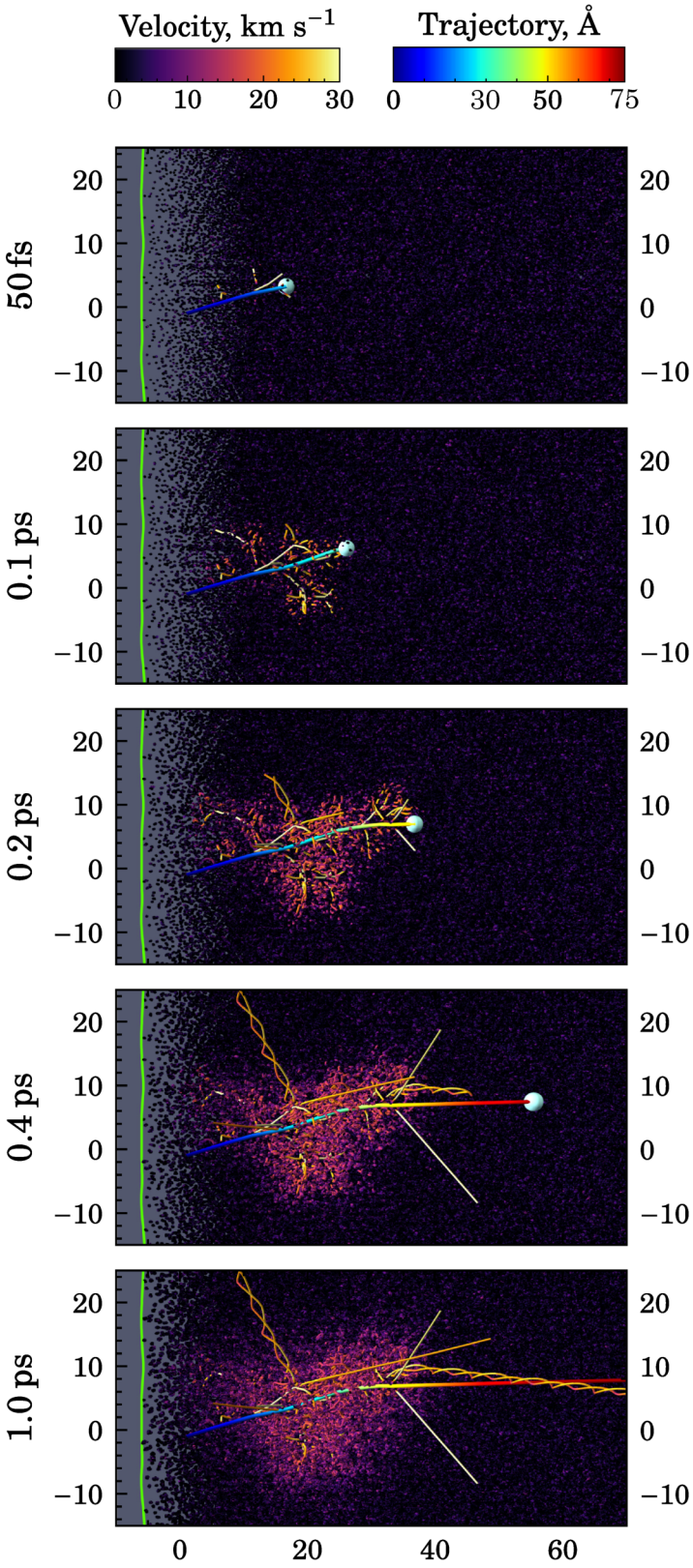


Figure 4.23 **Case:** $E_{\mathrm{Xe+}} = 1.4\,\mathrm{keV}$, $\beta = 70\,\mathrm{deg}$, run 2. Snapshots of temporal evolution of atomic velocity and ion trajectory length.

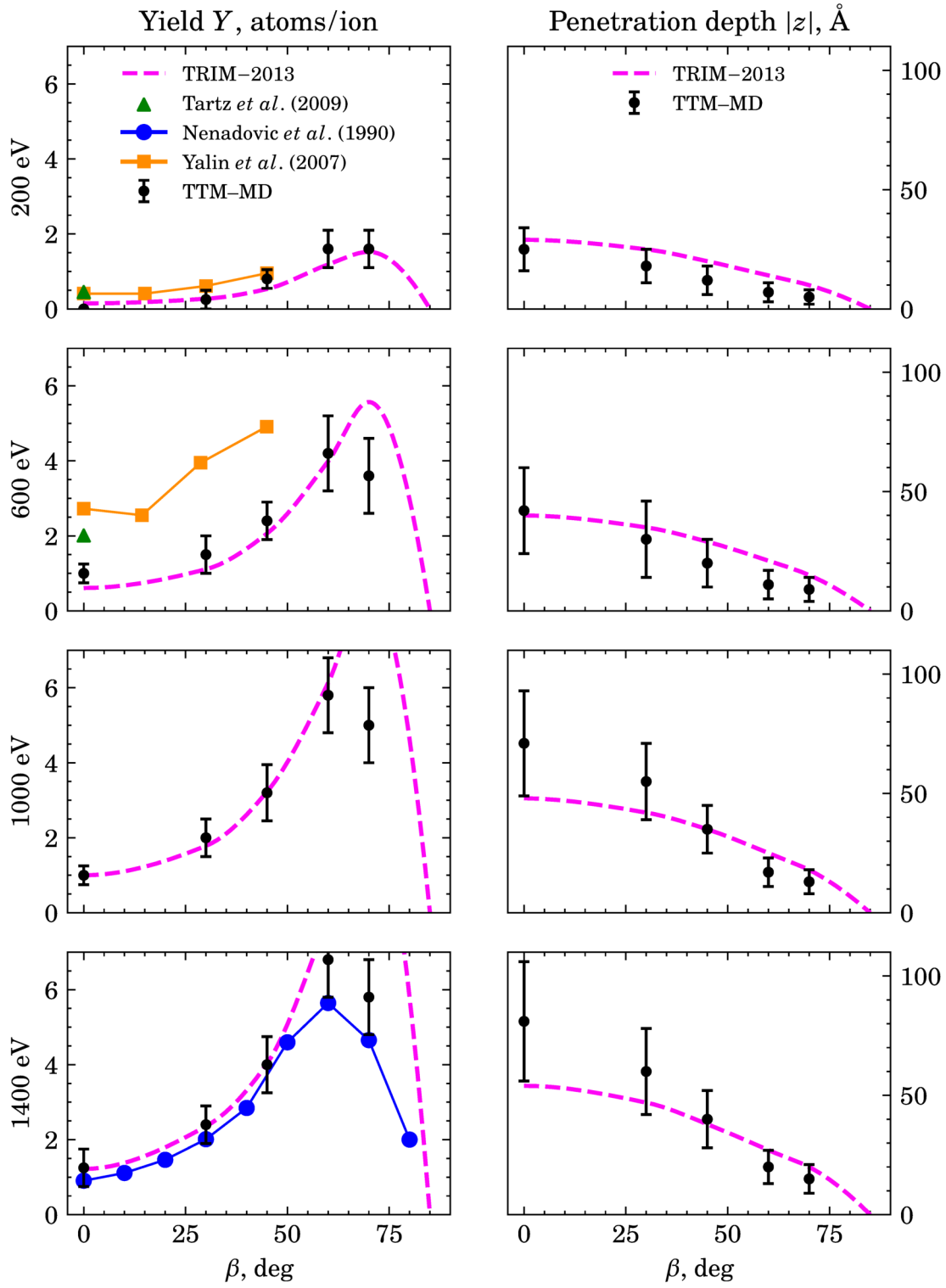


Figure 4.24 SiO_2 parameter study of yield and penetration depth including comparison with experimental data from Tartz, Heyn, Bundesmann, and Neumann [62], Nenadović *et al.* [63], Yalin *et al.* [64], and Ziegler *et al.* [68] (denoted as TRIM–2013).

irradiation. Their lowest energy case was $E_{Ar^+} = 3\,\text{keV}$ and they investigated impact angles up to $\beta = 70\,\text{deg}$. Assuming that collisions between the xenon ion and the target atoms are governed by Coulomb type collisions one can assume that results using a heavier ion can be extrapolated based on the proportional dependence of the ion's kinetic energy on the mass:

$$\Upsilon = \frac{M_{Ar^+}}{M_{Xe^+}} = \frac{40}{131} = 0.31\,. \tag{4.2}$$

Thus, the 3 keV case may be extrapolated to an impact energy of 1.4 keV by means of the following expression

$$Y^{Xe^+}_{1.4\,\text{keV}} = Y^{Ar^+}_{3\,\text{keV}} \cdot \Upsilon \cdot \frac{1.4\,\text{keV}}{3\,\text{keV}}\,. \tag{4.3}$$

The blue, circle-marked plot in Figure 4.24 is the result of applying Eq. (4.3) and exhibits a high degree of correlation with the results obtained from the TRIM–2013 calculated yield values up to $\beta = 50\,\text{deg}$. Two additional datasets were identified, including the normal incidence yields for $E = [200, 600]$ eV by Tartz, Heyn, Bundesmann, and Neumann [62] as well as angle-dependent yields for the same energies by Yalin *et al.* [64]. The overall agreement of the TTM–MD simulations with the experimental and TRIM–2013 calculated data shows increased variance in comparison to the two previously investigated materials. While the agreement of both yield and penetration depth at $E = 200\,\text{eV}$ is satisfactory, the TTM–MD data features a considerable degree of deviation at $E = 600\,\text{eV}$. Here, at lower impact angles both TRIM–2013 and TTM–MD predict a yield between $Y(0 - 45\,\text{deg}) \approx 0.8 - 2.2\,\text{atoms/ion}$ and the experimental data was obtained as $Y \approx 2.5 - 5.0\,\text{atoms/ion}$ in the same angular range. It should be noted that the authors Yalin *et al.* [64] and Tartz, Heyn, Bundesmann, and Neumann [62] utilized the *differential* sputter yield in $\text{mm}^3\,\text{C}^{-1}$ in their analysis. The *total* sputter yield (atoms/ion) of these publications presented in the plots in Figure 4.24 was calculated based on the number of Si and O atoms in quartz per mm^3, assuming a charge of the impacting ion of 1.6×10^{-19} C/ion. Surprisingly, the agreement of TTM–MD and TRIM–2013 data matches excellently even for the high-energy cases up to $\beta = 65\,\text{deg}$. In the $E = 1400\,\text{eV}$ case, the extrapolated experimental data from Nenadović *et al.* [63] remains well within all error bars of the simulations, thereby supporting the validity of the assumptions outlined (see Eq. (4.3)). Furthermore, the different results obtained for lower energy impacts indicate the difficulty of determining sputter yields experimentally as well as consistenly being able to results due to the different types of quartz ($\alpha-$, $\beta-$, and amorphous SiO_2).

The results of the penetration depth from both TRIM–2013 and TTM–MD demonstrate a strong correlation up to an energy of $E = 600\,\text{eV}$. At higher energies, TTM–MD indicates that the penetration depth is significantly greater at normal incidence of (80 ± 20) Å, which can be attributed to the channeling effects observed in the principal analysis section, which TRIM–2013 is unable to resolve. This effect may also be a contributing factor to sputter yields due to the crystalline orientation in close proximity to the surface of the target which would explain the visible variations in sputter yields at lower impact energies. At higher impact angles, TTM–MD suggests a lower penetration depth. It is unlikely for grains to be exactly oriented parallel to the high angle of impacts very close to the surface, resulting in the ion colliding with more atoms and thus traversing the target not as deep as when crystalline channels are aligned with the ion's trajectory.

4.4 Silicon carbide

This section presents the results of the analysis of silicon carbide (SiC), the final material investigated in this thesis. Silicon carbide is widely utilized in surface treatments of high-performance components within the aerospace and automotive industries due to its exceptional mechanical properties. Despite its less favorable electrical characteristics, SiC holds potential to enhance the durability and lifespan of compounds currently in use.

4.4.1 Principal analysis

The temporal evolution plots of the ion velocity and penetration depth for the highest impact energy case ($E = 1400\,\text{eV}$) are shown in Figure 4.25. For the case of SiC, a logarithmic time-scale was selected for the convenience of the reader, given that the variations in velocity and depth between the runs are minimal at normal incidence.

The ion relaxation time at normal incidence is 0.8 ps at a mean penetration depth of $|z| = 48\,\text{Å}$. The high density of Si and C coupled with their strong bonds leads to a minor mean variance from the mean velicty and penetration depth. The ion undergoes, on average, 5 collisions in the first 0.1 ps, which subsequently result in a reduction in velocity of approximately 50 % relative to its initial value. It is noteworthy that the depth of penetration initially increases at a gradual rate, followed by a more pronounced acceleration after $t = 0.1\,\text{ps}$ until $t = 0.5\,\text{ps}$. Rapid collision events yield a nearly exact exponential decay in velocity over the timeframe of $0.1\,\text{ps} < t < 0.7\,\text{ps}$. With the exception of run 4 (red graph), the data indicate that the implantation depth and velocity of the ion become thermally Maxwellian

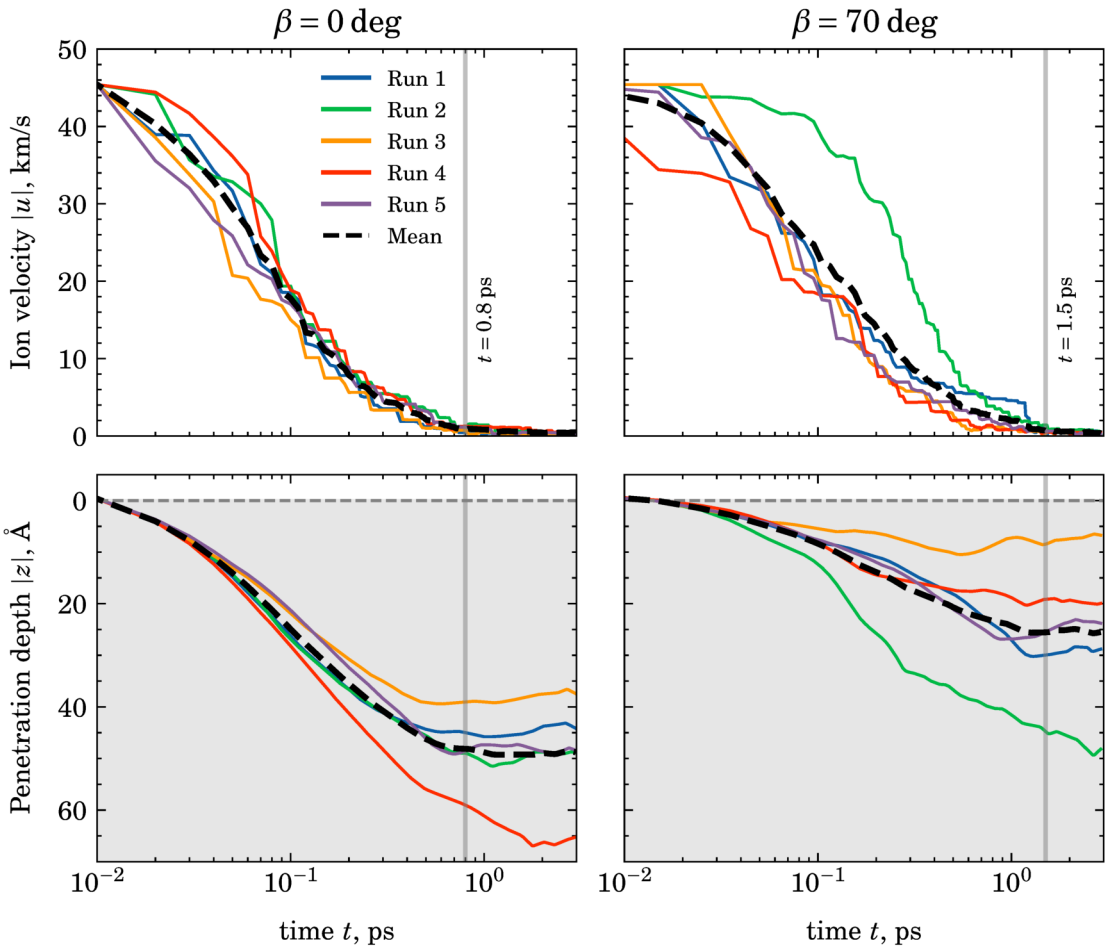


Figure 4.25 **Case:** $E_{\mathrm{Xe+}} = 1.4\,\mathrm{keV}$, $\beta \in \{0, 70\}$ deg. Top row: Time-dependent ion velocity of the four different runs with mean indicated by dashed black line. Bottom row: Time-dependent total penetration depth $|z|$.

governed quite rapidly. This is evidenced by the absence of clearly distinguishable bouncing effects after $t = 0.8\,\mathrm{ps}$. It is suggested that the strong bonds responsible for the hardness and mechanical strength of SiC are able to absorb and dissipate the kinetic energy input from the collision cascade.

In the scenario of $\beta = 70\,\mathrm{deg}$ (right column), mean variations from the mean value become slightly larger with run 2 (green graph) as one potential outlier. The first few hundreds of femtoseconds, the ion is subject to less number of collision events, triggering a slower decrease of velocity. A relaxation time twice as high as observed in the normal incidence scenario is evident $t^{\mathrm{rest}} = 1.5\,\mathrm{ps}$ and the depth of penetration first increases slowly the first 0.1 ps only to become steeper from $0.1\,\mathrm{ps} < t < 0.7\,\mathrm{ps}$ until the ion is implanted, similarly to the normal incidence scenario.

To illustrate the different collision cascade and thermal spike regimes contingent on the ion's impact angle, a comparison of atomic and electronic temperatures in addition to the number of atoms forced out of their dcub or dhex lattice structure

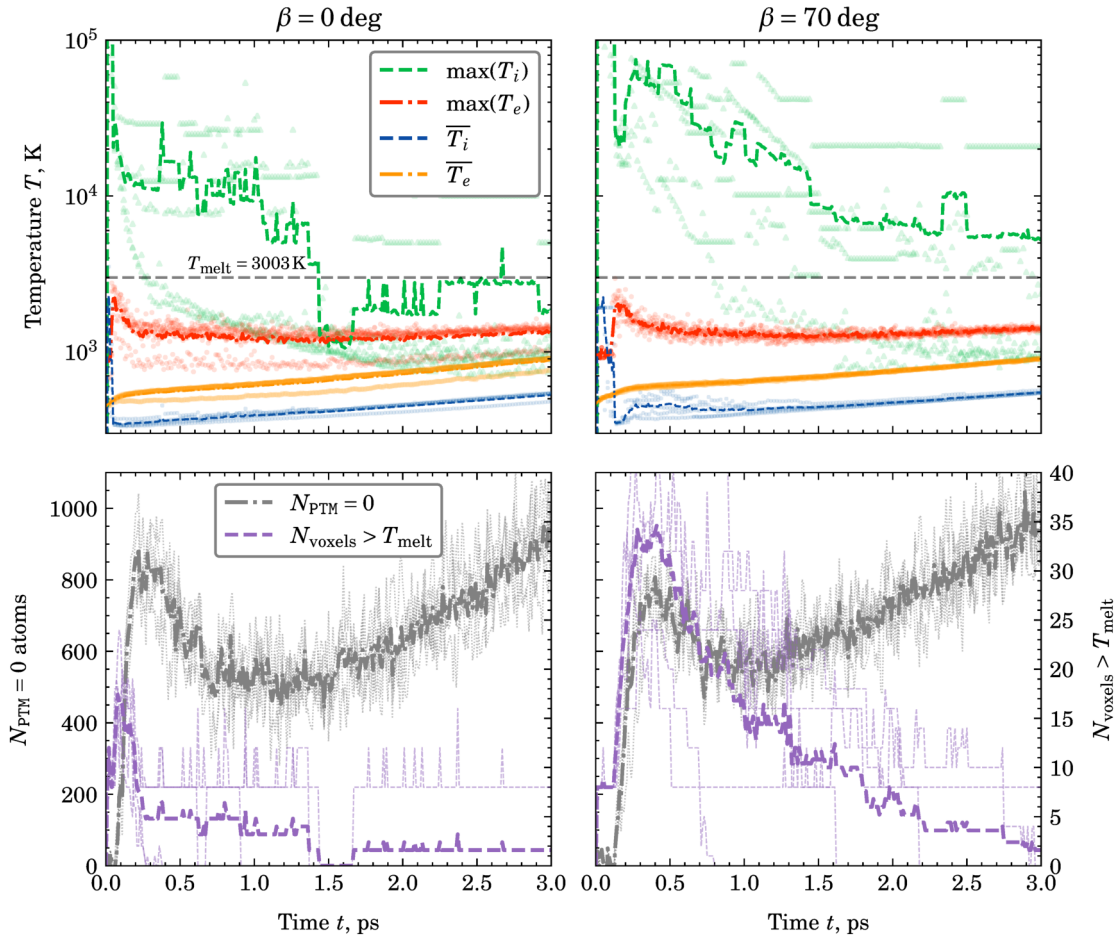


Figure 4.26 **Case:** $E_{\mathrm{Xe+}} = 1.4\,\mathrm{keV}$. Top row: comparison of mean and maximum atomic and electronic voxel temperatures. Bottom row: comparison of number of atoms converted to atoms without PTM structure and atomic voxels with temperatures higher than T_{melt}[5].

(i.e., decomposed) is presented in Figure 4.26. Since the ion impacts the PKA approximately 200 fs later in the $\beta = 70$ deg case due to its impact angle, the curves are slightly shifted in $+x$ direction. The large size of the supercell (330 000 atoms) yields very similar trends of the mean values of T_e and T_i (orange and blue curve, respectively). In fact, the maximum electronic voxel temperature is also very similar in terms of its trend and maximum value of just 2000 K, largely due to the high (electronic) heat capacity of SiC. However, noticable differences are observed for the maximum voxel atomic temperature: the thermal spike is much less pronounced in the case of normal incidence. Already after $t = 1.5$ ps, the hottest voxel temperature falls below the decomposition temperature. If the ion impacts the target at $\beta = 70$ deg the decomposition temperature is still exceeded by 2 voxels $\equiv$ 60 atoms. Despite the extensive noise in the data of max (T_i), an exponential decay can be observed in both cases. The more pronounced thermal spike is evident in the

plots of the lower row, wherein the number of voxels exceeding the decomposition temperature is more than twofold greater in the case of $\beta = 70\,\text{deg}$ compared to the grey graphs of PTM = 0 atoms, which exhibit a high degree of similarity of max $(N_{\text{PTM=0}}) = 900, 800$, respectively. Again, this finding implies that local decomposition is *not* a consequence of high temperature, but due to *local disclocation*, even after the first 0.5 ps after which the thermal spike is completed. In the bottom right plot of Figure 4.26, the number of voxels with $T > T_{\text{melt}}$ decays while the number of atoms forced out of their dcub or dhex structure steadily increases. Though less apparent, the same trend is visible in the normal impact case (bottom left plot).

A visual representation of the maximum energy and normal incidence scenario atomic trajectories filtered by the total trajectory length $|\mathbf{x}| > 2\,\text{Å}$ with a corresponding plot of $N_{\text{PTM=0}}$ on the right is outlined in Figure 4.27. The thermal spike at $t = 0.1 - 0.2\,\text{ps}$ is shown in the first two snapshots. Since only few atoms are visible, the trajectory length of most atoms forced out of their dcub and dhex lattice structure (max $(N_{\text{PTM=0}}) = 900$ is smaller than 2 Å, indicating that the thermal spike is able to locally enforce a small movement of individual atoms out of their lattice structure. After the thermal spike has culminated at $t = 0.2\,\text{ps}$, the number of $N_{\text{PTM=0}}$ atoms decreases as the collision cascade is initiated. This process generates an outward pressure that enables some atoms to "jump" back into the lattice as the interatomic distances are locally increased. This phenomenon can be observed in the snapshots of $t = 0.4\,\text{ps}$ and $t = 0.8\,\text{ps}$. Subsequently, at time $t = 1\,\text{ps}$, the catastrophic collision cascade commences, accompanied by a renewed increase in the number of $N_{\text{PTM=0}}$ atoms, although with a diminished gradient. At $t = 1.5\,\text{ps}$, most of the trajectory lengths in the region affected by the irradiation surpassed $|\mathbf{x}| > 2\,\text{Å}$. It is observed how the ion is able to create a decomposed zone of SiC with a maximum radius of 20 Å and depth of 40 Å, since most of the atoms visible in the last snapshot are of orange or red color, surrounding the ensemble visible at $t = 0.8\,\text{ps}$ where most of the shown trajectories are of blue color.

4.4.2 Parameter study

Results of the parameter study for silicon carbide are shown in Figure 4.28. In this case, the only experimental data found for SiC subjected to Xe^+ irradiation in the range of the present work is the data published by Ecke *et al.* [65]. They irradiated Si and SiC targets with Xe^+ ions between $0.5 - 5\,\text{keV}$ at an impact angle

[5] In the case of silicon carbide, the melting temperature should be seen as the temperature at which the compound decomposes into its constituents silicon, which becomes liquid, and carbon, which solidifies if the temperature remains below 3923 K.

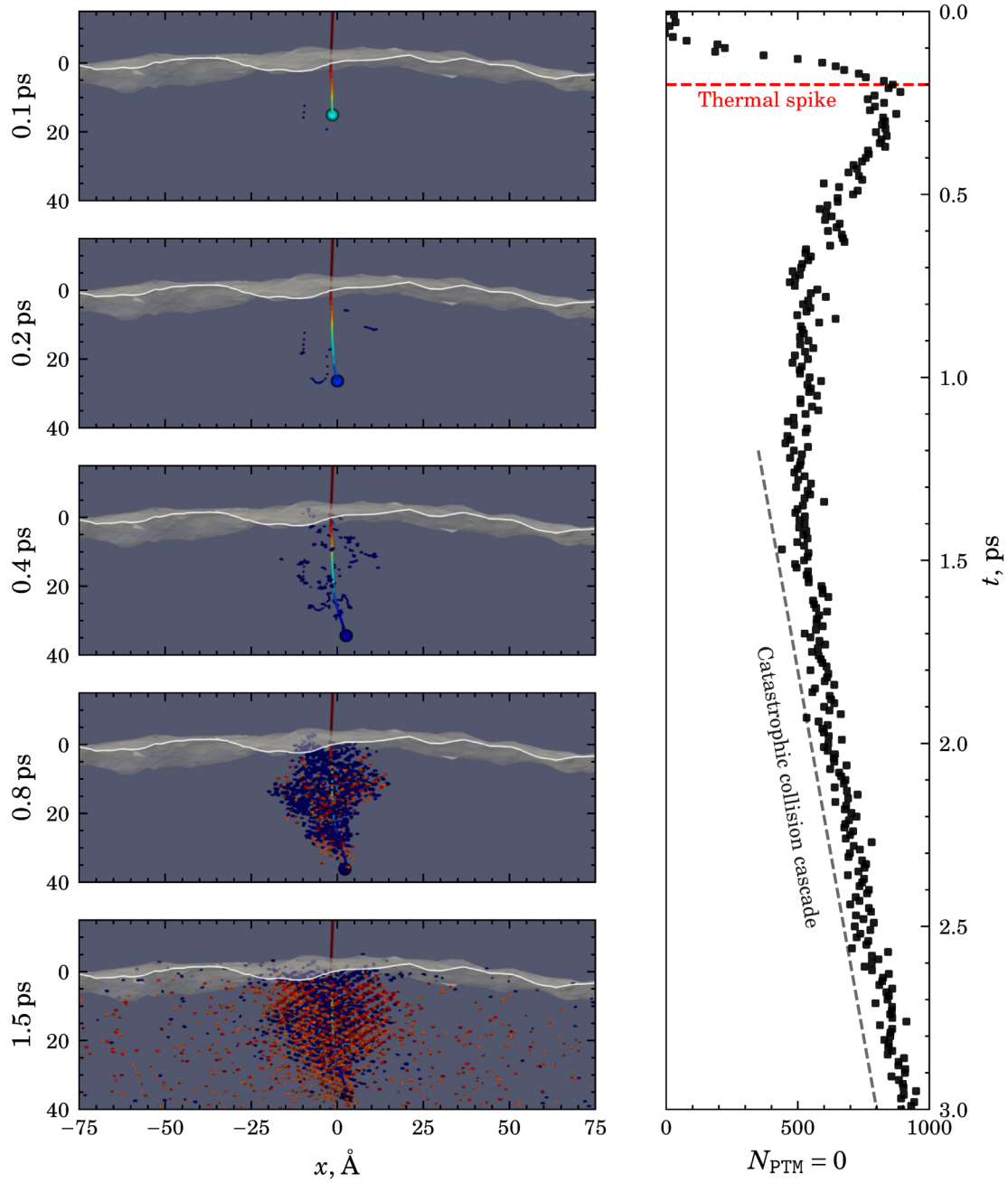


Figure 4.27 **Case:** $E_{\mathrm{Xe+}} = 1.4\,\mathrm{keV}$, $\beta = 0\,\mathrm{deg}$, run 2. **Left**: snapshots of temporal evolution collision cascade with ion velocity and atomic PTM structure, filtered by trajectory length. Target top surface indicated by transparent grey area / white line. Coloring of target atoms by PTM identified structure (PTM=0, dcub, and PTM=dhex). **Right**: Time-dependent number of atoms forced out of dcub or dhex structure.

of $\beta = 60\,\mathrm{deg}$. In order to derive the total sputter yields for these materials, sputter crater measurements and Auger depth profiling was employed. As was the case

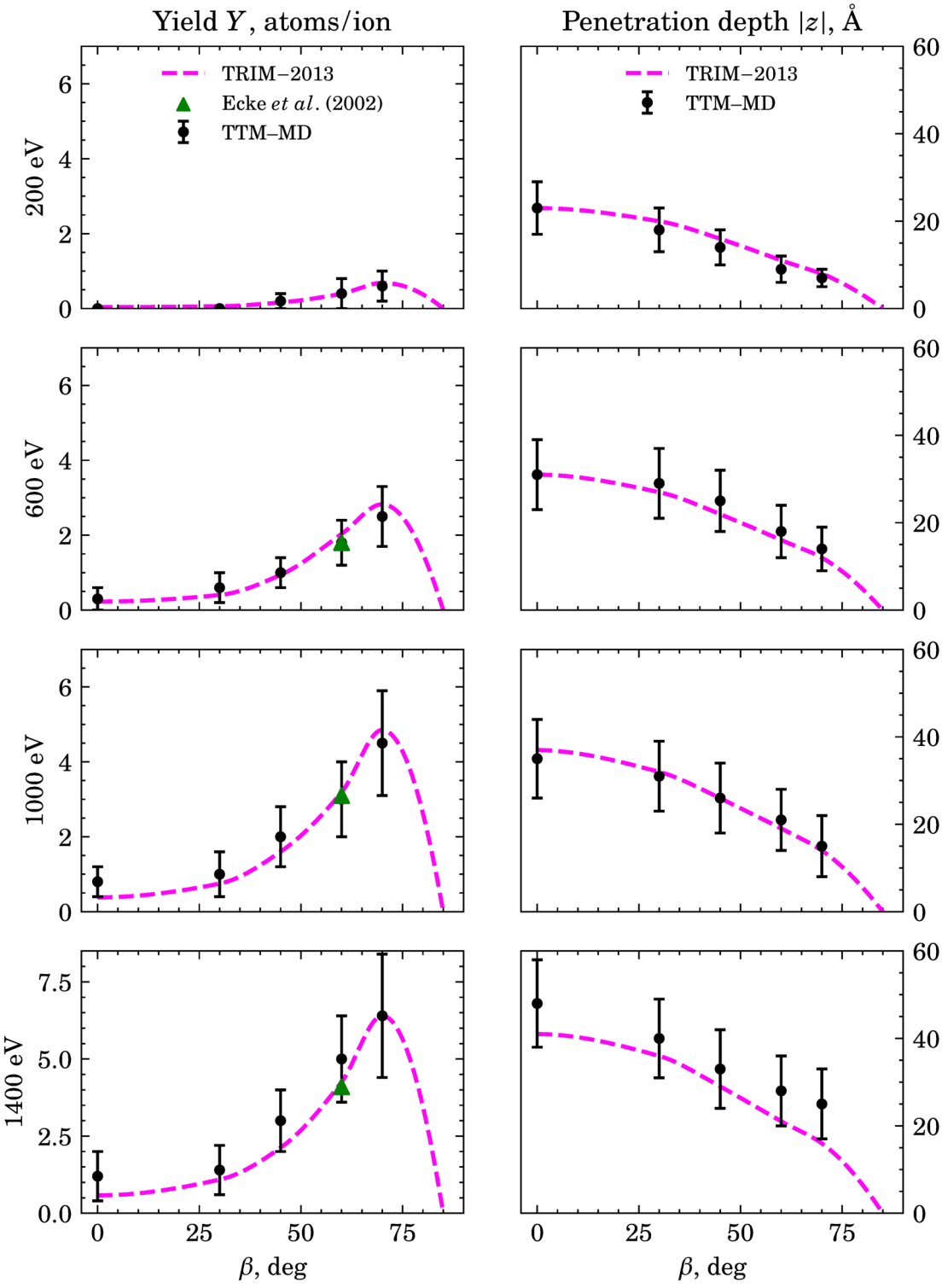


Figure 4.28 SiC parameter study of yield and penetration depth including comparison with experimental data from Ecke *et al.* [65] and Ziegler *et al.* [68] (denoted as TRIM–2013).

with the results from TRIM–2013 shown in the current section, they obtained very good agreement with the experimental data using an earlier version of TRIM, demonstrating that the TRIM–2013 calculated data serves as an excellent reference for comparison with the TTM–MD simulation. Throughout all investigated impact energies and angles, good overall agreement of Y and $|z|$ with both TRIM–2013 and the data from Ecke *et al.* [65] is achieved. Not only can the trends be accurately reproduced, but also the absolute values predicted by TTM–MD deviate on average less than 10 % from both datasets. The maximum yield of $Y = 6.4$ atoms/ion occurs at maximum impact energy and 70 deg incidence. In the case of SiC it was observed that the mean deviation of sputtered atoms from the mean yield according to Eq. (4.1) is quite large at $\epsilon = 30\,\%$. A possible explanation could be the way the Vashishta, Kalia, Nakano, *et al.* [117] interatomic potential works, since it not only accounts for the relative position between the individual atoms within the cutoff radius, but also their angular rotation. When the impact angle becomes large, the exact orientation of the PKAs that are impacted by the ion may play an important role. The hypothesis is corroborated by the observation that the mean deviation exhibits a notable decline for smaller impact angles, wherein the main component of the impact vector is oriented downwards in $-z$ direction.

A correlation is observed between the trend of the number of sputtered atoms and the penetration depth. With the exception of the highest analyzed impact angles, the sputter yield is generally overpredicted compared to the data from TRIM–2013. This circumstance correlates to the penetration depth, since TTM–MD predicts a deeper implamantation depth after the ion has come to rest in comparison the TRIM–2013, visible in the right column of Figure 4.28. Despite the impact energy of the lowest energy case is 7× lower than the highest energy case, the penetration is just 2× lower at normal incidence. Taking into account Figure 4.25 and Figure 4.26, it becomes clear that the collisions during the first 0.5 ps are responsible for the steepest velocity gradient where the ion is decelerated the most. In comparison to graphite, silicon carbide exhibits an approximately 4× higher yield, corresponding to another correlation found which relies on the number of PTM = 0 atoms. At the maximum of the thermal spike, graphite features $N^{\mathrm{C}}_{\mathrm{PTM}=0} = 500$ atoms compared to $N^{\mathrm{SiC}}_{\mathrm{PTM}=0} = 900$ atoms. It seems to be an important property governing the yield due to how many atoms are not inside their original lattice structure during the thermal spike and less inert to incoming forces. However, this observation must be taken with care, as titanium has $N^{\mathrm{Ti}}_{\mathrm{PTM}=0} = 3800$ atoms at a yield of 2× lower than SiC. It is therefore important to compare lattice structures of the similar types, since titanium mostly consists of `hcp` and `bcc` atoms, graphite of `graphene`, and silicon carbide of `dcub` and `dhex` atoms.

4.5 Synopsis

The results presented in this section demonstrate the ability of the TTM-MD model coupled with hybrid potentials to enable fundamental analysis of the physical phenomena taking place during keV ion sputtering. The thermal spike in both the electronic and atomic subsystems can be captured on the fs level, the collision cascade initiated by spread and relaxation of the thermal spike in the ps time span, and finally the full stopping and implantation of the ion are reproduced. The major advancement in this thesis is that the setup can also be used to accurately predict atomic sputtering yields of thruster materials, as the parameter studies for each material revealed. The main requirements are:

1. Knowledge of ion impact angle and energy.
2. Accurate target atom potential optimized for reproducing mechanical and thermal properties.
3. Knowledge of electronic properties of the target material.

The results presented in this section showed good to excellent agreement with the available experimental data. On the other hand, the agreement with TRIM–2013 featured a large variance especially for high impact angles and materials that are governed by complex interatomic interactions and where the lattice orientations play an important role such as in graphite, quartz or silicon carbide. Apart from the practical standpoint of predicting yield data the present study could verify observations that other publications predicted, most notably the results of graphite from Christie *et al.* [52].

If one thinks, one must reach conclusions. Conclusions are not always pleasant.

— H. Keller

5 Conclusion

This thesis addressed the topic of erosion modeling on the atomic length- and time-scale using TTM-MD, with a particular focus on erosion induced by xenon ion irradiation of materials used in RITs and HETs. The materials included titanium, graphite, quartz, and silicon carbide. The primary objective was to establish a numerical framework capable of capturing the trajectories of atoms in an ab initio type fashion. This allows for the temporal tracking of the evolution of macroscopic properties such as the temperature, and microscopic quantities, such as the individual kinetic energy or the PTM identified structure of individual atom. The application of this framework enables the acquisition of results pertinent to both physicists and engineers. For the former, this includes the characterization of the thermal spike, the collision cascade, and the lattice and electronic temperatures. For the latter, it encompasses the impact energy and angle-dependent sputter yield and implantation depth of the impacting xenon ion. This framework was constructed upon three fundamental mathematical models. First, this is the molecular dynamics simulation technique which enabled the calculation of the interaction between individual atoms in a time-resolved manner. The choice of interatomic potential governing interatomic forces, i.e., attraction and repulsion, and the correct utilization of numerical details, e.g., the time step and non-reflecting boundary conditions, largely determined the outcome. Secondly, the TTM model describes the interaction between the atomic and electronic subsystems, which was of particular importance when both subsystems are far from thermal equilibrium and is typically the case due to the rapid relaxation time of electrons. However, in instances of strong thermal non-equilibrium, such as those resulting from laser

or ion irradiation, an exchange of energy occurs due to atoms moving at a velocity exceeding the material-dependent binding energy. This results in friction with electrons or hot electrons interacting with lattice phonons. Thirdly, the ZBL model enabled the computation of interatomic forces in repulsion-dominated Coulomb-type collision regimes, which typically occur in cases involving fast ions or neutrons. The model's key advantage, apart from its proven precision over decades, particularly for high-energy collisions, is its simplicity: it requires only the atomic masses and atomic numbers from the collision partners as inputs, making it relatively straightforward to use.

The actual computations were carried out employing the massively parallel code LAMMPS, which already includes a TTM-MD package for simulation of thermal non-equilibrium cases. An adaptive electron voxel algorithm has been developed and implemented into LAMMPS, capable of activating or deactivating electronic voxels based on a threshold number of atoms inside a respective voxel, since they carry electrons with them. Other utilized software included the parallel-capable postprocessing tool ParaView for visualization and initial data preparation, as well as Python for the actual large scale analyses. Some postprocessing could already be done in LAMMPS itself during runtime, most notably the PTM package for identifying atomic crystal structures or atoms in non-lattice structure.

An underestimated aspect of this thesis was the equilibration step, which was essential for establishing well-defined and realistic initial conditions for the impact simulations, particularly for materials with specific lattice structures. The damping parameters for the ghost and penultimate atom ensembles surrounding the TTM-MD ensemble required careful calibration. This was crucial to prevent the reflection of pressure waves while simultaneously avoiding excessive cooling of the TTM-MD ensemble at their contact interfaces. This balance was necessary because the `nvt` thermostat was applied to the first two ensembles, while the microcanonical `nve` thermostat governed the latter. Selecting appropriate interatomic potentials was a particularly challenging task, demanding extensive testing in both the equilibration and impact scenarios. This was especially true for materials like graphite, quartz, and silicon carbide, where achieving the correct lattice structures was critical to accurately reflect known material properties. Some potentials performed well during equilibration but either overestimated or underestimated the yield during impact simulations, necessitating a preliminary parameter study of the interatomic potentials. Another significant challenge was obtaining electronic properties for non-metallic materials such as graphite, quartz, and silicon carbide. Most of the data available for the TTM model came from studies on ultrafast laser-matter interactions, which are predominantly focused on metals.

The TTM-MD simulations demonstrated strong agreement with experimental data, with the notable exception of the quartz case, where the direct applicability of the experimental findings to the present study remains uncertain. Deviations from TRIM-calculated data were generally minor at lower impact angles and energies, with more pronounced discrepancies emerging at maximum impact angles. This observation underlined the importance of accurately resolving atomic and electronic interactions—details that the interaction model used in TRIM fails to capture adequately. The best alignment between TTM-MD, TRIM, and experimental results was observed in the case of silicon carbide. In contrast, for graphite, TRIM significantly overestimated both yield and penetration depth, while TTM-MD results closely matched experimental observations. For titanium, TRIM tended to underpredict both quantities at lower impact angles, though agreement improved at higher angles. Across all conditions studied, the TTM-MD simulations successfully predicted not only the trends observed in the experimental data but also the absolute yield values. This thesis highlights the applicability of graphite for thruster components subjected to high-energy ion impacts, with TTM-MD predicting yields of 0.7 and 1.4 at normal and 70 deg incidence, respectively, at the highest analyzed impact energy of 1400 eV. In comparison, TRIM predicted significantly higher yields of 2.9 and 4.8. The thermal spike and collision cascade models described in the literature were accurately reproduced in these simulations, both in terms of their temporal evolution and their effects on the impact zone, locally and globally, within the supercell.

During the first few hundred femtoseconds, the thermal spike initiated by the impacting ion causes the displacement of atoms, either directly affected by the ion or the resulting primary knock-on atoms, leading to local melting, sublimation, or decomposition of the impact zone. Simultaneously, the ion loses most of its kinetic energy, demonstrating that the first 0 – 30 Å are the most affected by the ion, although the total penetration depth may extend to around 100 Å, depending on the impact angle. It was observed that the collision cascade does not commence until after the thermal spike subsides and some atoms have returned to their lattice positions. The cascade is driven by thermally excited atoms colliding with their neighboring atoms, propagating until the energy dissipates into the bulk material. In most cases, the highest number of PTM = 0 type atoms were found after a few picoseconds, following a linear increase from a local minimum of liquid-state atoms post-cascade.

A long-standing debate in the literature is whether the thermal spike or the collision cascade is primarily responsible for sputtering. In this thesis, the thermal spike was clearly identified as the dominant mechanism. The majority of atoms

ejected from the target and ultimately escaping the upper boundary condition were launched within the first 0.5 ps, a time frame preceding the onset of the collision cascade.

The significance of the current study is manyfold. The principal analysis carried out for each material gives detailed insight into the physical phenomena taking place, and a rich set of output data was generated, from which the quantities of interest were postprocessed. The de-facto standard code for sputtering and stopping simulations of ions is TRIM–2013. It has the benefit of requiring low computational resources, but, as could be seen in the results section, for highly lattice dependend materials such as graphite, the yield and penetration results deviated by more then multiple hundreds of percent, revealing the requirement of a more sophisticated numerical approach to resolve this issue, which was one of the objectives of the present study. Furthermore, as could be seen for the case of quartz and silicon carbide, experimental data may not always be at hand, especially when developing new compounds. In fact, another benefit from utilizing the TTM–MD framework implemented in this thesis is of financial and of practical nature. Devising, setting up, carrying out, measuring, and postprocessing of experiments is a costly and time-consuming activity, in particular of complex problems such as sputter yield measurements. Though TTM–MD can of course not entirely replace experiments in this area, it can be a strong supportive tool for understanding, designing, improving, and virtually testing materials of interest under arbitrary impact conditions, given that a validated interatomic potential is employed and the electronic properties of the material are known.

A typical use-case of the TTM–MD framework is the generation of datasets of angle-energy based impact yields for new or optimized material compounds in EP thrusters subjected to ion irradiation. Nowadays, it is possible to accurately model the plasma wall interactions in thrusters in 3D using PIC-DSMC, from which time-averaged surface impact properties can be obtained (see Figure 3.1). Using the TTM–MD produced datasets may be employed to erode virtually the thruster's walls and predict erosion and thus the lifetime of the thruster when closing this loop back to the PIC-DSMC simulations mentioned before. To give another example for a use-case, consider a fusion reactor with a sophisticated surface compound in order to withstand the extreme heat from the fusion plasma. These walls experience fast particle irradiation during the fusion process and therefore erode over time, making TTM–MD an attractive tool to help understand the particle-wall interaction and how the particle implantation might affect the physical properties of the chamber walls.

It should be noted that the methods and models used in this thesis are far from perfect and still require a tremendous amount of input data. In particular,

users must be aware of choosing an appropriate interatomic potential, find the electron temperature dependent electronic properties in the literature and correctly convert them into the units that most MD codes use. The statistical nature of MD makes multiple runs indispendable, from which mean values for each scenario can be derived, in this case the yield and penetration depth. The community of both MD and TTM simulation is very vibrant and teams of researchers around the globe work hard on improving these techniques and their coupling, hence the present study can by no means be considered “finished work”. Further validation loops of other materials is necessary as well as more runs per case to reduce the size of the errorbars presented in the parameter study sections. Still, a building block for bridging the gap between theoretical physics and practical engineering could be laid down, allowing future research in the area of irradiation problems to benefit from this thesis.

A Appendix

Contents

A.1 LAMMPS input files 105
A.2 Data availability statement 112

A.1 LAMMPS input files

Listing A.1 LAMMPS input file for equilibriation.

```
# This LAMMPS input script simulates:
#
#     Equilibriation of a titanium sample
#
#       ------------------------------
#
#                 Written by
#              Maximilian Maigler

# ---------- Units and boundary conditions ----------
units         metal
boundary      p p p
atom_style    atomic

# ---------- I/O ----------
variable      t_heat  equal 20
```

```
17 variable     t_melt  equal 10
18 variable     t_cool  equal 1000
19 variable     t_relax equal 20
20 variable     t_nve   equal 20
21 variable     thermofreq equal 500
22 variable     dump_freq  equal 500
23
24 # ---------- Temperature definitions ----------
25 variable     T_m equal 2000
26 variable     T_init equal 1
27 variable     T_melt equal 1.2*${T_m}
28 variable     T_fin  equal 350
29 variable     p      equal 1  # bar
30
31 # ---------- Physical properties ----------
32 variable     a equal 3.15  # Lattice constant
33 variable     RMSD equal 0.1
34
35 # ---------- Total extent of atom regions ----------
36 # TTM atoms
37 variable     Nx equal 15
38 variable     Ny equal ${Nx}
39 variable     Nz equal ${Nx}
40
41 # Correction factors in y and z due to hcp lattice
42 variable     ycorr equal 1.115
43 variable     zcorr equal 1.255
44 variable     Nx_hcp equal 2*${Nx}
45 variable     Ny_hcp equal ${ycorr}*${Ny}
46 variable     Nz_hcp equal 2*${zcorr}*${Nz}
47
48 # ---------- Thermostat related ----------
49 variable     dt         equal 0.001
50 variable     Np_damp    equal 1000
51 variable     NT_damp    equal 200
52 variable     p_damp     equal ${dt}*${Np_damp}
53 variable     T_damp     equal ${dt}*${NT_damp}
54
55 # ---------- Calculations ----------
56 variable     Nt_heat  equal floor(${t_heat}/${dt})
57 variable     Nt_melt  equal floor(${t_melt}/${dt})
58 variable     Nt_cool  equal floor(${t_cool}/${dt})
59 variable     Nt_relax equal floor(${t_relax}/${dt})
60 variable     Nt_nve   equal floor(${t_nve}/${dt})
61
```

```
# ---------- Regions ----------
lattice      custom 2.93093 a1 0.5 -0.866025 0 a2 0.5 0.866025 0 a3 0 0 1.596 basis 0.333333 0.666666 0.25 basis 0.666666 0.333333 0.75
region       domain block -${Nx_hcp} ${Nx_hcp} -${Ny_hcp} ${Ny_hcp} -${Nz_hcp} 0 units lattice
create_box   1 domain

# ---------- Define atoms ----------
create_atoms 1 region domain
mass         1 47.867   # Ti

# ---------- Potential ----------
pair_style   meam/sw/spline
pair_coeff   * * ../potentials/Hennig2008/Ti.meam.sw.spline Ti

# ---------- Neighbor settings ----------
neighbor     2.0 bin
neigh_modify every 1 delay 0 check yes

# ---------- Define PTM settings (default structures, RMSD threshold of 0.1) -------------------
compute      ptm all ptm/atom default ${RMSD} all
dump         dump_all all vtk ${dump_freq} res/dumps/base_*.vtu id type x y z vx vy vz c_ptm[1] type

thermo       ${thermofreq}

# ---------- Minimization ----------
# fix          1 all box/relax aniso 0
minimize     0 0 1000 1000

# ------ Initialize temperature and force ------
velocity     all create ${T_init} 123456 rot yes mom yes dist gaussian


# reset_timestep 0
timestep     ${dt}

# ------ 1. Heat to melting temperature ------
fix          1 all npt temp ${T_init} ${T_melt} ${T_damp} iso ${p} ${p} ${p_damp}
run          ${Nt_heat}
```

```
# ------ 2. Keep molten ------
unfix       1
fix         1 all nve
run         ${Nt_nve}
unfix       1
fix         1 all npt temp ${T_melt} ${T_melt} ${T_damp} iso ${p} ${p} ${p_damp}
run         ${Nt_melt}
unfix       1
fix         1 all nve
run         ${Nt_nve}
# ------ 3. Cool to final temperature ------
unfix       1
fix         1 all npt temp ${T_melt} ${T_fin} ${T_damp} iso ${p} ${p} ${p_damp}
run         ${Nt_cool}
unfix       1
fix         1 all nve
run         ${Nt_nve}
# ------ 4. Keep at final temperature ------
unfix       1
fix         1 all npt temp ${T_fin} ${T_fin} ${T_damp} iso ${p} ${p} ${p_damp}
run         ${Nt_relax}
unfix       1
fix         1 all nve
run         ${Nt_nve}

# ------ Unfix everything ------
unfix       1

write_data  restart.base.data.Ti
```

Listing A.2 LAMMPS input file for two-temperature molecular-dynamics of xenon impact onto equilibriated target. Normal incidence and 1.4 keV impact energy

```
# This LAMMPS input script simulates:
#
#    Impact of Xe onto a equil. Ti sample
#
#       ------------------------------
#
#                Written by
#             Maximilian Maigler

# ---------- Units and boundary conditions ----------
units         metal
boundary      p p p
atom_style    atomic

# ---------- Read restart ----------
read_data     ../base/restart.base.data.Ti

# ---------- Include base and ttm case variables ----------
include       ../base/in.vars

# ---------- Domain dimensions ----------
variable      domain_zlo_multi equal 0.1
variable      domain_zhi_multi equal 0.2

lattice       custom 2.93093 a1 0.5 -0.866025 0 a2 0.5
   0.866025 0 a3 0 0 1.596 basis 0.333333 0.666666 0.25 basis
    0.666666 0.333333 0.75

# ---------- Prepare regions ----------
# TTM thermostat (NVE)
variable      ttm_multi equal 0.75
variable      Nxt equal ${Nx_hcp}*${ttm_multi}
variable      Nyt equal ${Ny_hcp}*${ttm_multi}
variable      Nzt_lo equal ${Nz_hcp}*${ttm_multi}
variable      Nzt_hi equal 1.1*${Nz_hcp}
region        ttm_region block -${Nxt} ${Nxt} -${Nyt} ${Nyt} -
   ${Nzt_lo} ${Nzt_hi} units lattice
# Penultimate thermostat (reflectionless pressure-absorbing)
variable      penu_multi equal 0.2
variable      Nxp equal ${Nx_hcp}*${penu_multi}+${Nxt}
variable      Nyp equal ${Ny_hcp}*${penu_multi}+${Nyt}
variable      Nzp_lo equal ${Nz_hcp}*${penu_multi}+${Nzt_lo}
```

```
variable     Nzp_hi equal 1.1*${Nz_hcp}
region       penu_region block -${Nxp} ${Nxp} -${Nyp} ${Nyp}
   -${Nzp_lo} ${Nzp_hi} units lattice
# Output region
variable     out_multi equal 0.4
variable     Nyo equal ${Ny_hcp}*${out_multi}
variable     Nzo_lo equal ${Nz_hcp}*${out_multi}
variable     Nzo_hi equal 1.1*${Nz_hcp}
region       out_region block -${Nxt} ${Nxt} -${Nyo} ${Nyo} -
   ${Nzo_lo} ${Nzo_hi} units lattice

# ---------- Non reflective group temperatures ----------
group        Temp_ghost equal 350
group        Temp_penu  equal 350

# ---------- Prepare Groups ----------
group        ttm_group        region   ttm_region
group        penu_group_tmp   region   penu_region
group        ghost_group      subtract all penu_group_tmp
group        penu_group       subtract all ttm_group
   ghost_group
group        out_group        region   out_region

# ---------- Grid cells ----------
variable     Nxgrid equal 25
variable     Nygrid equal ${Nxgrid}
variable     Nzgrid equal floor(1.1*${Nxgrid})

# ---------- Initial velocity ----------
variable     ux_SI equal 0.0
variable     uy_SI equal 0.0
variable     uz_SI equal 45400
variable     ux equal ${ux_SI}*1e-2
variable     uy equal ${uy_SI}*1e-2
variable     uz equal -${uz_SI}*1e-2

# ---------- Define Xe atom ----------
create_atoms 2 single 0 0.0 2.0 units box
group        xe_group type 2
group        ttm_all union ttm_group xe_group

# ---------- Potential ----------
pair_style   hybrid/overlay meam/sw/spline zbl 0.2 1.333
pair_coeff   * * meam/sw/spline ../potentials/Hennig2008/Ti.
   meam.sw.spline Ti Ti
```

```
pair_coeff   1 1 zbl 22.0 22.0
pair_coeff   1 2 zbl 22.0 54.0

# ---------- Neighbor settings ----------
neighbor     2.0 bin
neigh_modify every 1 delay 0 check yes

# ---------- Initialize PKA and freeze ghost atoms ----------
velocity     xe_group    set ${ux} ${uy} ${uz} sum no units box
#velocity    ghost_group zero linear
#velocity    ghost_group zero angular

# ---------- Thermostats ----------
fix          1 ghost_group nvt temp ${Temp_ghost} ${Temp_ghost} 0.05
fix          2 penu_group nvt temp ${Temp_penu} ${Temp_penu} 0.05
fix          3 ttm_group nve
fix          4 xe_group nve
fix          5 ttm_all ttm/mod 342785 ttmInputFile.txt &
             ${Nxgrid} ${Nygrid} ${Nzgrid} set 350 outfile 100 res/Te/Te.out

# ---------- Calculate averages -------------------
fix          ave all ave/grid 1 10 10 ${Nxgrid} ${Nygrid} ${Nzgrid} temp vx vy vz

# ---------- Computes -------------------
compute      ptm       all ptm/atom default 0.1 all
compute      cmpgrid   all property/grid ${Nxgrid} ${Nygrid} ${Nzgrid} xc yc zc
compute      outTemp   out_group temp
compute      ttmTemp   ttm_group temp
compute      penuTemp  penu_group temp
compute      ghostTemp ghost_group temp

# ---------- Export pos, vel and forces -------------
dump         dmpxe    xe_group    vtk 10 res/dumps/Xe_*.vtp id type x y z vx vy vz type id
dump         dmpttm   out_group   vtk 10 res/dumps/out_*.vtk id type x y z vx vy vz type c_ptm[1] id
dump         dmpGridTemp all grid/vtk 10 res/dumps/grid_Temp_*.vtr f_ave:grid:data[1]
dump         dmpGridVel  all grid/vtk 10 res/dumps/grid_Vel_
```

```
   *.vtr  f_ave:grid:data[2] f_ave:grid:data[3] f_ave:grid:
   data[4]

# ---------- Run -------------
timestep     0.0002
thermo_style custom step ${step}*${timestep} c_outTemp[0]
   c_ttmTemp[0] c_penuTemp[0] c_ghostTemp[0]
thermo       10
run          10000
```

A.2 Data availability statement

The entire set of input files and generated raw data are available upon reasonable request.

Bibliography

[1] **Statista**, *Number of active satellites from 1957 to 2023*, https://www.statista.com/statistics/897719/number-of-active-satellites-by-year, [Online; accessed 22-August-2024], 2024.

[2] **K. E. Tsiolkovsky**, *Selected works of konstantin e. tsiolkovsky*, 2004.

[3] **D. A. Herman, T. Gray, I. Johnson, S. Hussein, and T. Winkelmann**, "Development and qualification status of the electric propulsion systems for the nasa ppe mission and gateway program," in *37th International Electric Propulsion Conference*, 2022.

[4] **J. Jackson, S. Miller, J. Cassady, E. Soendker, B. Welander, M. Barber, and P. Y. Peterson**, "13kW advanced electric propulsion flight system development and qualification," The 36th International Electric Propulsion Conference, Electric Rocket Propulsion Society, 2019.

[5] **V. Glushko**, *Development of Rocketry and Space Technology in the USSR*. Novosti Press Publishing House, 1973.

[6] **B. Harvey**, "The legacy," *Russian Planetary Exploration: History, Development, Legacy, Prospects*, pp. 325–331, 2007.

[7] **R. Cybulski, D. Shellhammer, R. Lovell, E. Domino, J. Kotnik, J. Cybulski, and R. Loveli**, "Results from SERT I ion rocket flight test," in *Proceedings*, Air Force Office of Scientific Research, vol. 1, 1965, p. 21.

[8] **P. Bartlett and A. Stelbovics**, "Calculation of electron-impact total-ionization cross sections," *Physical Review A*, vol. 66, Jul. 2002. DOI: 10.1103/PhysRevA.66.012707.

[9] **J. Miller, S. Pullins, D. Levandier, Y.-H. Chiu, and R. Dressler**, "Xenon charge exchange cross sections for electrostatic thruster models," *Journal of Applied Physics*, vol. 91, Feb. 2002. DOI: 10.1063/1.1426246.

[10] **M. Maigler, F. Maaß, J. Schein, and N. Wallace**, "Coupled Particle-in-Cell and Direct-Simulation Monte-Carlo Modelling of Grid Erosion by Ion Bombardment in Radio-Frequency Ion Thruster Grids," in *Proceedings of the 74th International Astronautical Congress (IAC)*, International Astronautical Federation (IAF), 2023.

[11] **J. Polk, V. Chaplin, J. Anderson, J. Yim, G. Soulas, G. Williams, and R. Shastry**, "Modeling grid erosion in the NEXT ion thruster using the CEX2D and CEX3D codes," *Journal of Electric Propulsion*, vol. 2, Apr. 2023. DOI: 10.1007/s44205-023-00043-0.

[12] **R. E. Wirz, J. R. Anderson, D. M. Goebel, and I. Katz**, "Ion thruster grid erosion assessment for deep space missions iepc-2007-265," 2007. [Online]. Available: https://api.semanticscholar.org/CorpusID:53590221.

[13] **E. Ahedo**, "Plasmas for space propulsion," *Plasma Physics and Controlled Fusion*, vol. 53, no. 12, p. 124 037, Nov. 2011. DOI: 10.1088/0741-3335/53/12/124037.

[14] **N. P. Brown and M. L. R. Walker**, "Review of plasma-induced hall thruster erosion," *Applied Sciences*, vol. 10, no. 11, 2020, ISSN: 2076-3417. DOI: 10.3390/app10113775.

[15] **N. Gascon and S. Barral**, "Wall material effects in stationary plasma thrusters. I. Parametric studies of an SPT-100," *Physics of Plasmas*, vol. 10, pp. 4123–4136, Oct. 2003. DOI: 10.1063/1.1611880.

[16] **R. Bond and P. Latham**, "Ion thruster extraction grid design and erosion modelling using computer simulation," in *31st Joint Propulsion Conference and Exhibit*, 1995, p. 2923.

[17] **X. Peng, D. Keefer, and W. M. Ruyten**, "Plasma particle simulation of electrostatic ion thrusters," *Journal of Propulsion and Power*, vol. 8, no. 2, pp. 361–366, 1992.

[18] **K. Ira, J. Polk, J. Brophy, and J. Anderson**, "Numerical simulations of ion thruster accelerator grid erosion," in *38th AIAA/ASME/SAE/ASEE Joint Propulsion Conference & Exhibit*, 2002, p. 4261.

[19] **C. C. Farnell, J. D. Williams, and P. J. Wilbur**, *Numerical simulation of ion thruster optics*. National Aeronautics and Space Administration [Glenn Research Center], 2003.

[20] **R. E. Wirz, J. R. Anderson, and I. Katz**, "Time-dependent erosion of ion optics," *Journal of Propulsion and Power*, vol. 27, no. 1, pp. 211–217, 2011. DOI: 10.2514/1.46845.

[21] **O. Kalentev, K. Matyash, J. Duras, K. F. Lüskow, R. Schneider, N. Koch, and M. Schirra**, "Electrostatic ion thrusters-towards predictive modeling," *Contributions to Plasma Physics*, vol. 54, no. 2, pp. 235–248, 2014.

[22] **J. W. Emhoff and I. D. Boyd**, "Modeling of total thruster performance for nasa's evolutionary xenon thruster ion optics," *Journal of propulsion and power*, vol. 22, no. 4, pp. 741–748, 2006.

[23] **R. E. Wirz, J. R. Anderson, D. M. Goebel, and I. Katz**, "Decel grid effects on ion thruster grid erosion," *IEEE transactions on plasma science*, vol. 36, no. 5, pp. 2122–2129, 2008.

[24] **S. Y.-M. Cheng**, "Modeling of hall thruster lifetime and erosion mechanisms," Ph.D. dissertation, Massachusetts Institute of Technology, 2007.

[25] **H. Koizumi, K. Komurasaki, and Y. Arakawa**, "Numerical prediction of wall erosion on a hall thruster," *Vacuum*, vol. 83, no. 1, pp. 67–71, 2008, ISSN: 0042-207X. DOI: 10.1016/j.vacuum.2008.03.096.

[26] **S. Cho, K. Komurasaki, and Y. Arakawa**, "Kinetic particle simulation of discharge and wall erosion of a Hall thruster," *Physics of Plasmas*, vol. 20, no. 6, p. 063 501, 2013, ISSN: 1070-664X. DOI: 10.1063/1.4810798.

[27] **H. Cao, Q. Li, K. Shan, Y. Cao, and L. Zheng**, "Effect of Preionization on the Erosion of the Discharge Channel Wall in a Hall Thruster Using a Kinetic Simulation," *IEEE Transactions on Plasma Science*, vol. 43, no. 1, pp. 130–140, 2015. DOI: 10.1109/TPS.2014.2367524.

[28] **V. Giannetti, T. Andreussi, A. Leporini, D. Estublier, and M. Andrenucci**, "Long-Life Low Erosion Hall Effect Thruster: Model and Simulations," in *Proceedings of the 5th Space Propulsion conference*, 2016.

[29] **A. Schinder, M. Walker, and J. Rimoli**, "Three-Dimensional Model for Erosion of a Hall-Effect Thruster Discharge Channel Wall," *Journal of Propulsion and Power*, vol. 30, pp. 1373–1382, Sep. 2014. DOI: 10.2514/1.B35098.

[30] **M. Passet, M. Panelli, and F. Battista**, "Numerical Modeling of Erosion in Hall Effect Thrusters," *Particles*, vol. 7, no. 1, pp. 121–143, 2024, ISSN: 2571-712X. DOI: 10.3390/particles7010007.

[31] **B. K. Parida, K. Sooraj, S. Hans, V. Pachchigar, S. Augustine, T. Remyamol, M. Ajith, and M. Ranjan**, "Sputtering yield and nanopattern formation study of BNSiO2 (Borosil) at elevated temperature relevance to Hall Effect Thruster," *Nuclear Instruments and Methods in Physics Research Section B: Beam Interactions with Materials and Atoms*, vol. 514, pp. 1–7, 2022.

[32] **F. Dessauer**, "Über einige Wirkungen von Strahlen. I: Mitteilung aus dem Universitätsinstitut für physikalische Grundlagen der Medizin in Frankfurt a. Main," *Zeitschrift für Physik*, vol. 12, no. 1, pp. 38–47, 1923.

[33] **M. Toulemonde, E. Paumier, and C. Dufour**, "Thermal spike model in the electronic stopping power regime," *Radiation Effects and Defects in Solids*, vol. 126, no. 1-4, pp. 201–206, 1993.

[34] **N. S. Jenkins**, "Medium Power Hall Thruster Erosion Modeling Using Dynamic Thruster Geometry," in *AIAA SCITECH 2024 Forum*, 2024, p. 1139.

[35] **M. Takahashi, M. Tsunoda, and H. Shoji**, "Ultra-clean sputtering process for magnetic thin films on hard disk drives," *Vacuum*, vol. 59, no. 2-3, pp. 814–824, 2000.

[36] **S. M. Rossnagel**, "Sputter deposition for semiconductor manufacturing," *IBM Journal of Research and development*, vol. 43, no. 1.2, pp. 163–179, 1999.

[37] **C. Solutions**, *Sputtering in IC Fabrication*, Accessed on March, 2024, 2023. [Online]. Available: https://resources.pcb.cadence.com/blog/2023-sputtering-in-ic-fabrication.

[38] **Y. Kuo, K. Okajima, and M. Takeichi**, "Plasma processing in the fabrication of amorphous silicon thin-film-transistor arrays," *IBM journal of research and development*, vol. 43, no. 1.2, pp. 73–88, 1999.

[39] **Y.-K. Moon, S. Lee, D.-H. Kim, D.-H. Lee, C.-O. Jeong, and J.-W. Park**, "Application of DC magnetron sputtering to deposition of InGaZnO films for thin film transistor devices," *Japanese Journal of Applied Physics*, vol. 48, no. 3R, p. 031 301, 2009.

[40] **C. Liu, Y. Sun, H. Qin, Y. Liu, S. Wei, and Y. Zhao**, "Low-temperature, high-performance InGaZnO thin-film transistors fabricated by capacitive coupled plasma-assistant magnetron sputtering," *IEEE Electron Device Letters*, vol. 40, no. 3, pp. 415–418, 2019.

[41] **P. Stuart, J. Osborn, and S. Lewis**, "The use of radio frequency sputter ion etching and scanning electron microscopy to study the internal structure of biological material," *Vacuum*, vol. 19, no. 11, pp. 503–506, 1969.

[42] **T. Müller, P. Walther, C. Scheidegger, R. Reichelt, S. Müller, and R. Guggenheim**, "Cryo-preparation and planar magnetron sputtering for low temperature scanning electron microscopy," *Scanning microscopy*, vol. 4, no. 4, p. 6, 1990.

[43] **D. H. Kim, S. Y. Lee, *et al.***, "Plasma sputtering of silicon dioxide substrate by low energy ar ion bombardment: Molecular dynamics simulation," *Journal of crystal growth*, vol. 237, pp. 217–222, 2002.

[44] **A.-P. Prskalo, S. Schmauder, C. Ziebert, J. Ye, and S. Ulrich**, "Molecular dynamics simulations of the sputtering process of silicon and the homoepitaxial growth of a si coating on silicon," *Computational materials science*, vol. 50, no. 4, pp. 1320–1325, 2011.

[45] **T. Metspalu, V. Jansson, V. Zadin, K. Avchaciov, K. Nordlund, A. Aabloo, and F. Djurabekova**, "Cu self-sputtering MD simulations for 0.1–5 keV ions at elevated temperatures," *Nuclear Instruments and Methods in Physics Research Section B: Beam Interactions with Materials and Atoms*, vol. 415, pp. 31–40, 2018.

[46] **T. Ono, T. Kenmotsu, and T. Muramoto**, "Simulation of the sputtering process," in *Reactive sputter deposition*, Springer, 2008, pp. 1–42.

[47] **E. C. Neyts and P. Brault**, "Molecular dynamics simulations for plasma-surface interactions," *Plasma Processes and Polymers*, vol. 14, no. 2, 2017.

[48] **P. Brault**, "Multiscale molecular dynamics simulation of plasma processing: Application to plasma sputtering," *Frontiers in Physics*, vol. 6, p. 59, 2018.

[49] **P. Brault, A.-L. Thomann, and M. Cavarroc**, "Theory and molecular simulations of plasma sputtering, transport and deposition processes," *The European Physical Journal D*, vol. 77, no. 2, p. 19, 2023.

[50] **H.-S. Ahn, T.-E. Kim, E. Cho, M. Ji, C.-K. Lee, S. Han, Y. Cho, and C. Kim**, "Molecular dynamics study on low-energy sputtering properties of MgO surfaces," *Journal of Applied Physics*, vol. 103, no. 7, 2008.

[51] **H. J. Christie**, *Molecular dynamics simulations in graphite and carbon materials*. University of Salford (United Kingdom), 2014.

[52] **H. Christie, M. Robinson, D. Roach, D. Ross, I. Suarez-Martinez, and N. A. Marks**, "Simulating radiation damage cascades in graphite," *Carbon*, vol. 81, pp. 105–114, 2015.

[53] **C. L. Phillips, R. J. Magyar, and P. S. Crozier**, "A two-temperature model of radiation damage in α-quartz," *The Journal of chemical physics*, vol. 133, no. 14, 2010.

[54] **D. Kanjilal**, "Swift heavy ion-induced modification and track formation in materials," *Current Science*, pp. 1560–1566, 2001.

[55] **E. G. Segre, H. A. Bethe, N. Ramsey, P. S. Morrison, and B. T. Feld**, "Experimental nuclear physics," DOE/ER/40609–2, 1953.

[56] **P. Sigmund**, "Stopping of heavy ions - a theoretical approach," *Springer Tracts in Modern Physics*, vol. 204, Jan. 2004.

[57] **R. Rymzhanov, S. Gorbunov, N. Medvedev, and A. Volkov**, "Damage along swift heavy ion trajectory," *Nuclear Instruments and Methods in Physics Research Section B: Beam Interactions with Materials and Atoms*, vol. 440, pp. 25–35, 2019, ISSN: 0168-583X. DOI: 10.1016/j.nimb.2018.11.034.

[58] **A. Abdullaev, K. Sekerbayev, R. Rymzhanov, V. Skuratov, J. O. Connell, B. Shukirgaliyev, A. Kozlovskiy, Y. Wang, and Z. Utegulov**, "Impact of swift heavy ion-induced point defects on nanoscale thermal transport in ZnO," *Materials Research Bulletin*, vol. 175, p. 112 786, 2024, ISSN: 0025-5408. DOI: 10.1016/j.materresbull.2024.112786.

[59] **M. Lang, R. Devanathan, M. Toulemonde, and C. Trautmann**, "Advances in understanding of swift heavy-ion tracks in complex ceramics," *Current Opinion in Solid State and Materials Science*, vol. 19, no. 1, pp. 39–48, 2015, Ion Beam Modification of Materials, ISSN: 1359-0286. DOI: 10.1016/j.cossms.2014.10.002.

[60] **M. Tartz, T. Heyn, C. Bundesmann, C. Zimmermann, and H. Neumann**, "Sputter yields of Mo, Ti, W, Al, Ag under xenon ion incidence," *The European Physical Journal D*, vol. 61, no. 3, pp. 587–592, 2011.

[61] **M. Nakano, S. Hosoda, and K. Nishiyama**, "Sputtering Yield of Carbon-Carbon Composite Due to Xenon Ion Bombardment in Ion Engines," *Transactions of the Japan Society for Aeronautical and Space Sciences*, vol. 58, no. 4, pp. 213–219, 2015.

[62] **M. Tartz, T. Heyn, C. Bundesmann, and H. Neumann**, "Measuring sputter yields of ceramic materials," in *Proceedings of the 31st International Electric Propulsion Conference. Fairview Park: ERPS*, 2009.

[63] **T. Nenadović, B. Perraillon, Ž. Bogdanov, Z. Djordjević, and M. Milić**, "Sputtering and surface topography of oxides," *Nuclear Instruments and Methods in Physics Research Section B: Beam Interactions with Materials and Atoms*, vol. 48, no. 1, pp. 538–543, 1990, ISSN: 0168-583X. DOI: doi.org/10.1016/0168-583X(90)90178-W.

[64] **A. Yalin, B. Rubin, S. Domingue, Z. Glueckert, and J. Williams**, "Differential Sputter Yields Of Boron Nitride, Quartz, and Kapton Due to Low Energy Xe+ Bombardment," *Collection of Technical Papers - 43rd AIAA/ASME/SAE/ASEE Joint Propulsion Conference*, vol. 3, p. 16, Jul. 2007. DOI: 10.2514/6.2007-5314.

[65] **G. Ecke, R. Kosiba, V. Kharlamov, Y. Trushin, and J. Pezoldt**, "The estimation of sputtering yields for SiC and Si," *Nuclear Instruments and Methods in Physics Research Section B: Beam Interactions with Materials and Atoms*, vol. 196, no. 1-2, pp. 39–50, 2002.

[66] **J. T. Yim**, "A survey of xenon ion sputter yield data and fits relevant to electric propulsion spacecraft integration," in *International Electric Propulsion Conference (IEPC)*, 2017.

[67] **J. E. Polk**, "A critical review and meta-analysis of xenon-on-carbon sputter yield data," *Journal of Applied Physics*, vol. 135, no. 4, 2024.

[68] **J. F. Ziegler, M. D. Ziegler, and J. P. Biersack**, "SRIM–The stopping and range of ions in matter," *Nuclear Instruments and Methods in Physics Research Section B: Beam Interactions with Materials and Atoms*, vol. 268, no. 11-12, pp. 1818–1823, 2010.

[69] **C. A. Volkert and A. M. Minor**, "Focused ion beam microscopy and micromachining," *MRS Bulletin*, vol. 32, pp. 389–399, 2007.

[70] **J. Van Noord**, "Lifetime assessment of the NEXT ion thruster," in *43rd AIAA / ASME / SAE / ASEE Joint Propulsion Conference & Exhibit*, 2007, p. 5274.

[71] **P. Sigmund**, "Sputtering by Ion Bombardment: Theoretical Concepts," in *Sputtering by Particle Bombardment I: Physical Sputtering of Single-Element Solids*, **R. Behrisch**, Ed. Berlin, Heidelberg: Springer Berlin Heidelberg, 1981, pp. 9–71, ISBN: 978-3-540-38514-1. DOI: 10.1007/3540105212_7.

[72] **T. P. S.I. Anisimov B.L. Kapeliovich**, "Electron emission from metal surfaces exposed to ultrashort laser pulses," *Sov. Journal of Experimental and Theoretical Physics*, vol. 39, no. 2, 1974.

[73] **M. Backman**, "Effects of nuclear and electronic stopping power on ion irradiation of silicon-based compounds," Dissertation, Ph.D. dissertation, 2012.

[74] **P. Sigmund**, "Nuclear Stopping," in *Stopping of Heavy Ions: A Theoretical Approach*, **P. Sigmund**, Ed. Berlin, Heidelberg: Springer Berlin Heidelberg, 2004, pp. 85–94, ISBN: 978-3-540-44471-8. DOI: 10.1007/978-3-540-44471-8_10.

[75] **J. P. Biersack and J. F. Ziegler**, "The Stopping and Range of Ions in Solids," in *Ion Implantation Techniques*, **H. Ryssel and H. Glawischnig**, Eds., Berlin, Heidelberg: Springer Berlin Heidelberg, 1982, pp. 122–156, ISBN: 978-3-642-68779-2.

[76] **M. J. Berger and S. M. Seltzer**, "Stopping powers and ranges of electrons and positrons," *National Bureau of Standards Center for Radiation Research*, 1982.

[77] **Wikipedia**, *Bethe formula — Wikipedia, the free encyclopedia*, https://en.wikipedia.org/wiki/Bethe_formula, [Online; accessed 22-May-2024], 2024.

[78] **J. Deasy**, "ICRU Report 49, Stopping Powers and Ranges for Protons and Alph Particles," *Medical Physics*, vol. 21, no. 5, pp. 709–710, 1994. DOI: https://doi.org/10.1118/1.597176.

[79] **M. Dobkevicius**, "Modelling and design of inductively coupled radio frequency gridded ion thrusters with an application to Ion Beam Shepherd type space missions," Ph.D. dissertation, University of Southampton, 2017.

[80] **B. J. Alder, T. E. Wainwright, *et al.***, "Phase transition for a hard sphere system," *The Journal of chemical physics*, vol. 27, no. 5, p. 1208, 1957.

[81] **A. Rahman**, "Correlations in the motion of atoms in liquid argon," *Physical review*, vol. 136, no. 2A, A405, 1964.

[82] **L. Verlet**, "Computer "Experiments" on Classical Fluids. I. Thermodynamical Properties of Lennard-Jones Molecules," *Phys. Rev.*, vol. 159, pp. 98–103, 1 Jul. 1967. DOI: 10.1103/PhysRev.159.98.

[83] **A. Rahman and F. H. Stillinger**, "Molecular dynamics study of liquid water," *The Journal of Chemical Physics*, vol. 55, no. 7, pp. 3336–3359, 1971.

[84] **J. A. McCammon, B. R. Gelin, and M. Karplus**, "Dynamics of folded proteins," *Nature*, vol. 267, pp. 585–590, 1977.

[85] **G. Ciccotti, C. Dellago, M. Ferrario, E. Hernández, and M. Tuckerman**, "Molecular simulations: Past, present, and future," *The European Physical Journal B*, vol. 95, no. 1, p. 3, 2022.

[86] **D. Duffy and A. Rutherford**, "Including the effects of electronic stopping and electron–ion interactions in radiation damage simulations," *J. Phys. Condens. Matter*, vol. 19, p. 016 207, 2006. DOI: 10.1088/0953-8984/19/1/016207.

[87] **M. Maigler, T. Held, D. O. Gericke, J. Schein, B. Rethfeld, S. H. Glenzer, and M. Z. Mo**, "Atomistic modelling of ultrafast laser-induced melting in copper," in *High-Power Laser Ablation VIII*, **C. R. Phipps and V. E. Gruzdev**, Eds., International Society for Optics and Photonics, vol. 12939, SPIE, 2024, 129390Q. DOI: 10.1117/12.3012630.

[88] **T. Held, S. T. Weber, and B. Rethfeld**, "Influence of band occupation on electron-phonon coupling in gold," *arXiv preprint arXiv:2308.01067*, 2023.

[89] **Z. Lin, L. V. Zhigilei, and V. Celli**, "Electron-phonon coupling and electron heat capacity of metals under conditions of strong electron-phonon nonequilibrium," *Phys. Rev. B*, vol. 77, p. 075 133, 7 Feb. 2008. DOI: 10.1103/PhysRevB.77.075133.

[90] **E. E. Zhurkin and A. S. Kolesnikov**, "Atomic scale modelling of Al and Ni(111) surface erosion under cluster impact," *Nuclear Instruments and Methods in Physics Research Section B: Beam Interactions with Materials and Atoms*, vol. 202, pp. 269–277, 2003, 6th International Conference on Computer Simulation of Radiation Effects in Solids, ISSN: 0168-583X. DOI: 10.1016/S0168-583X(02)01868-2.

[91] **R. Landauer**, "Spatial variation of currents and fields due to localized scatterers in metallic conduction," *IBM Journal of Research and Development*, vol. 1, no. 3, pp. 223–231, 1957. DOI: 10.1147/rd.13.0223.

[92] **S. Datta**, *Electronic Transport in Mesoscopic Systems* (Cambridge Studies in Semiconductor Physics and Microelectronic Engineering). Cambridge University Press, 1995.

[93] **P. Karna, M. Hoque, S. Thakur, P. Hopkins, and A. Giri**, "Direct measurement of ballistic and diffusive electron transport in gold," *Nano Letters*, vol. 23, Jan. 2023. DOI: 10.1021/acs.nanolett.2c03781.

[94] **R. Courant, K. Friedrichs, and H. Lewy**, "Über die partiellen Differenzengleichungen der mathematischen Physik," *Mathematische Annalen*, vol. 100, no. 1, pp. 32–74, 1928.

[95] **P. Drude**, "Zur Elektronentheorie der Metalle," *Annalen der Physik*, vol. 306, no. 3, pp. 566–613, 1900. DOI: https://doi.org/10.1002/andp.19003060312. eprint: https://onlinelibrary.wiley.com/doi/pdf/10.1002/andp.19003060312. [Online]. Available: https://onlinelibrary.wiley.com/doi/abs/10.1002/andp.19003060312.

[96] **D. S. Ivanov and L. V. Zhigilei**, "Combined atomistic-continuum modeling of short-pulse laser melting and disintegration of metal films," *Phys. Rev. B*, vol. 68, p. 064 114, 6 Aug. 2003. DOI: 10.1103/PhysRevB.68.064114.

[97] **S. I. Anisimov and B. Rethfeld**, "Theory of ultrashort laser pulse interaction with a metal," in *Nonresonant Laser-Matter Interaction (NLMI-9)*, **V. I. Konov and M. N. Libenson**, Eds., International Society for Optics and Photonics, vol. 3093, SPIE, 1997, pp. 192–203. DOI: 10.1117/12.271674.

[98] **J. E. Jones and S. Chapman**, "On the determination of molecular fields.—I. From the variation of the viscosity of a gas with temperature," *Proceedings of the Royal Society of London. Series A, Containing Papers of a Mathematical and Physical Character*, vol. 106, no. 738, pp. 441–462, 1924. DOI: 10.1098/rspa.1924.0081.

[99] **P. Schwerdtfeger and D. J. Wales**, "100 years of the lennard-jones potential," *Journal of Chemical Theory and Computation*, vol. 20, no. 9, pp. 3379–3405, 2024, PMID: 38669689. DOI: 10.1021/acs.jctc.4c00135.

[100] **J. Lenhard, S. Stephan, and H. Hasse**, "On the History of the Lennard-Jones Potential," *Annalen der Physik*, 2024. DOI: doi.org/10.1002/andp.202400115.

[101] **S. Stephan, J. Staubach, and H. Hasse**, "Review and comparison of equations of state for the Lennard-Jones fluid," *Fluid Phase Equilibria*, vol. 523, p. 112 772, 2020, ISSN: 0378-3812. DOI: 10.1016/j.fluid.2020.112772.

[102] **M. Griebel, S. Knapek, G. Zumbusch, and A. Caglar**, *Numerische Simulation in der Moleküldynamik: Numerik, Algorithmen, Parallelisierung, Anwendungen* (Springer-Lehrbuch). Springer Berlin Heidelberg, 2013, ISBN: 9783642187797.

[103] **M. S. Daw and M. I. Baskes**, "Embedded-atom method: Derivation and application to impurities, surfaces, and other defects in metals," *Phys. Rev. B*, vol. 29, pp. 6443–6453, 12 Jun. 1984. DOI: 10.1103/PhysRevB.29.6443.

[104] **M. W. Finnis and J. E. Sinclair**, "A simple empirical N-body potential for transition metals," *Philosophical Magazine A*, vol. 50, no. 1, pp. 45–55, 1984. DOI: 10.1080/01418618408244210.

[105] **K. Hartz-Behrend**, "Einsatz der klassischen Molekulardynamik (MD) für die quantitative Vorausberechnung des Benetzungsverhaltens beim Löten," Dissertation, Universität der Bundeswehr München, Fakultät für Elektrotechnik und Informationstechnik, Neubiberg, 2012.

[106] **M. I. Baskes**. "How to develop modified embedded atom method potentials," Los Alamos National Laboratory. (Apr. 14, 2016), [Online]. Available: https://www.slideserve.com/lisle/how-to-develop-modified-embedded-atom-method-potentials (visited on 05/25/2024).

[107] **A. Carlsson**, "Beyond Pair Potentials in Elemental Transition Metals and Semiconductors," *Solid State Physics - Advances in Research and Applications*, vol. 43, no. C, pp. 1–91, 1990, ISSN: 0081-1947. DOI: 10.1016/S0081-1947(08)60323-9.

[108] **M. I. Baskes**, "Application of the Embedded-Atom Method to Covalent Materials: A Semiempirical Potential for Silicon," *Phys. Rev. Lett.*, vol. 59, pp. 2666–2669, 23 1987. DOI: 10.1103/PhysRevLett.59.2666.

[109] **M. I. Baskes**, "Determination of modified embedded atom method parameters for nickel," *Materials Chemistry and Physics*, vol. 50, no. 2, pp. 152–158, 1997.

[110] **J. Tersoff**, "New empirical approach for the structure and energy of covalent systems," *Phys. Rev. B*, vol. 37, pp. 6991–7000, 12 Apr. 1988. DOI: 10.1103/PhysRevB.37.6991.

[111] **D. W. Brenner**, "Empirical potential for hydrocarbons for use in simulating the chemical vapor deposition of diamond films," *Phys. Rev. B*, vol. 42, pp. 9458–9471, 15 Nov. 1990. DOI: 10.1103/PhysRevB.42.9458. [Online]. Available: https://link.aps.org/doi/10.1103/PhysRevB.42.9458.

[112] **S. J. Stuart, A. B. Tutein, and J. A. Harrison**, "A reactive potential for hydrocarbons with intermolecular interactions," *The Journal of Chemical Physics*, vol. 112, no. 14, pp. 6472–6486, Apr. 2000, ISSN: 0021-9606. DOI: 10.1063/1.481208.

[113] **J. Los and A. Fasolino**, "Intrinsic long-range bond-order potential for carbon: Performance in Monte Carlo simulations of graphitization," *Physical Review B*, vol. 68, no. 2, p. 024 107, 2003.

[114] **P. Vashishta, R. Kalia, J. Rino, and I. Ebbsjö**, "Interaction potential for sio2: A molecular-dynamics study of structural correlations," *Physical review. B, Condensed matter*, vol. 41, pp. 12 197–12 209, Jul. 1990. DOI: 10.1103/PhysRevB.41.12197.

[115] **P. N. Keating**, "Effect of invariance requirements on the elastic strain energy of crystals with application to the diamond structure," *Phys. Rev.*, vol. 145, pp. 637–645, 2 May 1966. DOI: 10.1103/PhysRev.145.637.

[116] **F. H. Stillinger and T. A. Weber**, "Computer simulation of local order in condensed phases of silicon," *Phys. Rev. B*, vol. 31, pp. 5262–5271, 8 Apr. 1985. DOI: 10.1103/PhysRevB.31.5262.

[117] **P. Vashishta, R. K. Kalia, A. Nakano, and J. P. Rino**, "Interaction potential for silicon carbide: A molecular dynamics study of elastic constants and vibrational density of states for crystalline and amorphous silicon carbide," *Journal of Applied Physics*, vol. 101, no. 10, p. 103 515, May 2007, ISSN: 0021-8979. DOI: 10.1063/1.2724570.

[118] **A. P. Thompson, H. M. Aktulga, R. Berger, D. S. Bolintineanu, W. M. Brown, P. S. Crozier, P. J. in 't Veld, A. Kohlmeyer, S. G. Moore, T. D. Nguyen, R. Shan, M. J. Stevens, J. Tranchida, C. Trott, and S. J. Plimpton**, "LAMMPS - a flexible simulation tool for particle-based materials modeling at the atomic, meso, and continuum scales," *Comp. Phys. Comm.*, vol. 271, p. 108 171, 2022. DOI: 10.1016/j.cpc.2021.108171.

[119] **J. Chen, D. Tzou, and J. Beraun**, "A semiclassical two-temperature model for ultrafast laser heating," *International Journal of Heat and Mass Transfer*, vol. 49, no. 1, pp. 307–316, 2006, ISSN: 0017-9310. DOI: 10.1016/j.ijheatmasstransfer.2005.06.022.

[120] **V. V. Pisarev and S. V. Starikov**, "Atomistic simulation of ion track formation in UO2," *Journal of Physics: Condensed Matter*, vol. 26, no. 47, p. 475 401, 2014. DOI: 10.1088/0953-8984/26/47/475401.

[121] **TOP500**, *Hsuper*, Accessed on Jun 25, 2024, 2022. [Online]. Available: https://top500.org/system/180076/.

[122] **W. Schroeder, K. Martin, and B. Lorensen**, *The Visualization Toolkit (4th ed.)* Kitware, 2006, ISBN: 978-1-930934-19-1.

[123] **J. Ahrens, B. Geveci, and C. Law**, "Visualization handbook," in **C. D. Hansen and C. R. Johnson**, Eds. Burlington, MA, USA: Elsevier Inc., 2005, ch. ParaView: An End-User Tool for Large Data Visualization, pp. 717–731.

[124] **H. Wang, S. Yang, and B. Wei**, "Density and structure of undercooled liquid titanium," *Chinese Science Bulletin*, vol. 57, pp. 719–723, 2012.

[125] **R. G. Hennig, T. J. Lenosky, D. R. Trinkle, S. P. Rudin, and J. W. Wilkins**, "Classical potential describes martensitic phase transformations between the α, β, and ω titanium phases," *Phys. Rev. B*, vol. 78, p. 054 121, 5 Aug. 2008. DOI: 10.1103/PhysRevB.78.054121.

[126] **J. Hone**, "Carbon nanotubes: Thermal properties," *Dekker Encyclopedia of Nanoscience and nanotechnology*, vol. 7, pp. 603–610, 2004.

[127] **T. G. White, J. Vorberger, C. Brown, B. Crowley, P. Davis, S. Glenzer, J. Harris, D. Hochhaus, S. Le Pape, T. Ma, *et al.***, "Observation of inhibited electron-ion coupling in strongly heated graphite," *Scientific reports*, vol. 2, no. 1, p. 889, 2012.

[128] **M. Xibraku, M. Garcia, and B. Bauerhenne**, "Interatomic potential for carbon based quantum-technology applications," *Advanced Quantum Technologies*, May 2024. DOI: 10.1002/qute.202300454.

[129] **A. Ravichandran, M. Mehta, A. A. Woodworth, and J. W. Lawson**, "Molecular dynamics simulations of ultrafast radiation induced melting at metal–semiconductor interfaces," *Journal of Applied Physics*, vol. 129, no. 21, 2021.

[130] **C. Zhang, F. Mao, and F.-S. Zhang**, "Electron–ion coupling effects on radiation damage in cubic silicon carbide," *Journal of Physics: Condensed Matter*, vol. 25, no. 23, p. 235 402, 2013.

[131] **A. Leino, S. Daraszewicz, O. Pakarinen, K. Nordlund, and F. Djurabekova**, "Atomistic two-temperature modelling of ion track formation in silicon dioxide," *EPL (Europhysics Letters)*, vol. 110, p. 16 004, Apr. 2015. DOI: 10.1209/0295-5075/110/16004.

[132] **X. Wang, X. Ye, H. Yao, P. Wei, F. Yin, J. Cong, Y. Tong, L. Zhang, and W. Zhu**, "Simulation of femtosecond laser ablation and spallation of titanium film based on two-temperature model and molecular dynamics," *Journal of Laser Applications*, vol. 33, no. 1, p. 012 047, Jan. 2021, ISSN: 1042-346X. DOI: 10.2351/7.0000264.

[133] **H. Mousavi and J. Khodadadi**, "Electronic heat capacity and conductivity of gapped graphene," *Physica E: Low-dimensional Systems and Nanostructures*, vol. 50, pp. 11–16, 2013, ISSN: 1386-9477. DOI: doi.org/10.1016/j.physe.2013.02.015.

[134] **J. Lindhard and M. Scharff**, "Energy loss in matter by fast particles of low charge," *Dan. Mat. Fys. Medd.*, vol. 27, no. 15, 1953.

[135] **Sandia Corporation**, *LAMMPS Documentation (27 Jun 2024 version); LAMMPS documentation — docs.lammps.org*, https://docs.lammps.org/Manual.html, [Accessed 03-07-2024], 2024.

[136] **P. M. Larsen, S. Schmidt, and J. Schiøtz**, "Robust structural identification via polyhedral template matching," *Modelling and Simulation in Materials Science and Engineering*, vol. 24, no. 5, p. 055 007, 2016.

[137] **P. Hirel**, "Atomsk: A tool for manipulating and converting atomic data files," *Computer Physics Communications*, vol. 197, pp. 212–219, 2015, Images taken from: https://atomsk.univ-lille.fr/tutorial_polycrystal.php, ISSN: 0010-4655. DOI: 10.1016/j.cpc.2015.07.012.

[138] **W. Pokojski and P. Pokojska**, "Voronoi diagrams – inventor, method, applications," *Polish Cartographical Review*, vol. 50, pp. 141–150, Sep. 2018. DOI: 10.2478/pcr-2018-0009.

[139] **L. S. Ramsdell**, "Studies on silicon carbide," *American Mineralogist: Journal of Earth and Planetary Materials*, vol. 32, no. 1-2, pp. 64–82, 1947.

[140] **A. Stukowski**, "Visualization and analysis of atomistic simulation data with OVITO-the Open Visualization Tool," *Modelling and Simulation in Materials Science and Engineering*, vol. 18, no. 1, 2010. DOI: {10.1088/0965-0393/18/1/015012}.

[141] **N. Velisavljevic and G. N. Chesnut**, "Direct hcp to bcc structural phase transition observed in titanium alloy at high pressure," *Applied Physics Letters*, vol. 91, no. 10, 2007.

[142] **E. E. GmbH**, *Material Sound Velocities | Olympus IMS — olympus-ims.com*, https://www.olympus-ims.com/en/ndt-tutorials/thickness-gauge/appendices-velocities/, [Accessed 16-07-2024].

[143] **P. Budzyński, M. Kamiński, Z. Surowiec, M. Wiertel, V. Skuratov, and E. Korneeva**, "Effects of xenon-ion irradiation on the tribological properties and crystal structure of titanium and its alloy Ti6Al4V," *Tribology International*, vol. 156, p. 106 854, 2021.

[144] **S. Gavarini, R. Bes, N. Millard-Pinard, S. Cardinal, C. Peaucelle, A. Perrat-Mabilon, V. Garnier, and C. Gaillard**, "A comparative study of TiN and TiC: Oxidation resistance and retention of xenon at high temperature and under degraded vacuum," *Journal of Applied Physics*, vol. 109, no. 1, 2011.

[145] **H. Vasco, T. Hlatshwayo, S. Motloung, M. Mlambo, B. Mwankemwa, S. Petrovic, and V. Skuratov**, "Effect of swift heavy ion irradiation in the migration behavior of Xe implanted into TiN," *Vacuum*, vol. 163, pp. 59–68, 2019, ISSN: 0042-207X. DOI: doi.org/10.1016/j.vacuum.2019.01.054.